ANALYSIS AND DESIGN OF SLOTTED SUBSTRATE INTEGRATED WAVEGUIDE ANTENNA ON CYLINDRICAL SURFACE

A THESIS SUBMITTED TO
THE GRADUATE SCHOOL OF NATURAL AND APPLIED SCIENCES
OF
MIDDLE EAST TECHNICAL UNIVERSITY

BY

ÖMER BAYRAKTAR

IN PARTIAL FULFILLMENT OF THE REQUIREMENTS
FOR
THE DEGREE OF DOCTOR OF PHILOSOPHY
IN
ELECTRICAL AND ELECTRONICS ENGINEERING

SEPTEMBER 2014

Approval of the thesis:

ANALYSIS AND DESIGN OF SLOTTED SUBSTRATE INTEGRATED WAVEGUIDE ANTENNA ON CYLINDRICAL SURFACE

submitted by **ÖMER BAYRAKTAR** in partial fulfillment of the requirements for the degree of **Doctor of Philosophy in Electrical and Electronics Engineering Department, Middle East Technical University** by,

Prof. Dr. Canan Özgen _____
Dean, Graduate School of **Natural and Applied Sciences**

Prof. Dr. Gönül Turhan Sayan _____
Head of Department, **Electrical and Electronics Engineering**

Prof. Dr. Özlem Aydın Çivi _____
Supervisor, **Electrical and Electronics Engineering Dept., METU**

Examining Committee Members:

Prof. Dr. Sencer Koç _____
Electrical and Electronics Engineering Dept., METU

Prof. Dr. Özlem Aydın Çivi _____
Electrical and Electronics Engineering Dept., METU

Assoc. Prof. Dr. Vakur B. Ertürk _____
Electrical and Electronics Engineering Dept., Bilkent Univ.

Assoc. Prof. Dr. Lale Alatan _____
Electrical and Electronics Engineering Dept., METU

Prof. Dr. Şimşek Demir _____
Electrical and Electronics Engineering Dept., METU

Date: 03.09.2014

I hereby declare that all information in this document has been obtained and presented in accordance with academic rules and ethical conduct. I also declare that, as required by these rules and conduct, I have fully cited and referenced all material and results that are not original to this work.

Name, Last name : Ömer BAYRAKTAR

Signature :

ABSTRACT

ANALYSIS AND DESIGN OF SLOTTED SUBSTRATE INTEGRATED WAVEGUIDE ANTENNA ON CYLINDRICAL SURFACE

Bayraktar, Ömer

Ph. D., Department of Electrical and Electronics Engineering

Supervisor: Prof. Dr. Özlem Aydın Çivi

September 2014, 160 pages

This thesis presents novel traveling wave conformal shunt slot arrays on cylindrical substrate integrated waveguide (CSIW) placed on a cylindrical surface in the circumferential direction at K-band. Mutual couplings of longitudinal slots on broad wall of CSIW are formulated and active admittance formulas of the slots are derived which are used in Elliott's design procedure to design slotted CSIW arrays. The designs are carried out at *25 GHz* using non-uniform and uniform slot separations. The non-uniform slot array allocates *16* slot elements near resonance where element separations are determined to compensate different spatial phase delays of each element to increase directivity. The slot excitation amplitudes are determined by *-20 dB* side lobe level (SLL) Taylor distribution using aperture projection method. However, *-20 dB* SLL is not achieved because of large slot separations. Hence, slot lengths are optimized further to increase bandwidth for beam steering applications at the expense of increasing SLL. Three different uniform slot arrays are designed with

25 slot elements to obtain pencil beam pattern with low SLL using aperture projection method and genetic algorithm. The required slot excitation coefficients are achieved by using slots with large deviations from resonance. Both uniform and non-uniform slot arrays are fabricated using standard printed circuit board (PCB) process. The antennas are measured and about *10°* beam steering in H-plane is obtained when frequency is swept between *24-26 GHz* in the non-uniform slot array. Pencil beam pattern with desired *-20 dB* SLL is achieved at *25 GHz* in the uniform slot array.

Keywords: Substrate Integrated Waveguide Antenna Array, Conformal Arrays, Slotted Waveguide Array, Traveling Wave Antenna, Slot Antenna Array.

ÖZ

SİLİNDİRİK YÜZEY ÜZERİNDE YARIKLI DALGA KILAVUZU ANTENİNİN ANALİZ VE TASARIMI

Bayraktar, Ömer
Doktora, Elektrik ve Elektronik Mühendisliği Bölümü
Tez Yöneticisi: Prof. Dr. Özlem Aydın Çivi

Eylül 2014, 160 sayfa

Bu tezde, K-bantta çalışan silindirik yüzey tümleşik dalga kılavuzu (SYTDK) üzerinde yeni bir yüzey uyumlu yürüyen dalga yarık anten dizisi sunulmuştur. SYTDK yapısı silindir üzerine çevrel yönde yerleştirilmiştir. SYTDK'nın geniş duvarına yerleştirilmiş boylamsal yarıklar için bağlaşım formülleri türetilmiş ve yarıkların aktif admitans formülleri bulunmuştur. Aktif admitans değerleri, Elliott tasarım yöntemi ile birlikte kullanılarak yarıklı SYTDK dizileri tasarlanmıştır. Tasarımlar *25 GHz*'de yarık aralıklarının eşit olduğu ve olmadığı durumlar için yapılmıştır. Yarık aralıklarının eşit olmadığı durumda, rezonans yakınında *16* yarık elemanı kullanılmıştır. Huzme yönlülüğünü arttırmak amacı ile yarıkların arasındaki mesafeler uygun şekilde seçilerek yarık elemanlarının farklı uzaysal faz farkları giderilmiştir. Yarık uyarım katsayılarının büyüklüğü, yüzey izdüşümü yöntemi kullanılarak *-20 dB* yan huzme seviyesi (SLL) Taylor dağılımı ile belirlenmiştir. Ancak büyük yarık mesafeleri sebebi ile *-20 dB* yan huzme seviyesi elde

edilememiştir. Bu sebepten frekans taraması uygulamaları için yan huzme seviyesinin daha da artması karşılığında yarık uzunluklarının optimizasyonu ile tasarımın bandı genişletilmiştir. Eşit yarık aralıkları kullanılarak *25* yarık elemanından oluşan üç farklı yarık dizisi tasarımı yapılmıştır. Tasarımlarda düşük yan huzme seviyesine sahip kalem biçimli huzme elde etmek amacı ile yüzey izdüşümü yöntemi ve genetik algoritma kullanılmıştır. İstenen yarık uyarım katsayıları, rezonanstan oldukça sapan yarıklar kullanılarak elde edilmiştir. Eşit olan ve olmayan yarık aralıklarına sahip diziler standart baskı devre kartı (PCB) teknolojisi kullanılarak üretilmiştir. Antenler ölçülmüş ve eşit yarık aralıklarına sahip olmayan dizide frekansın *24-26 GHz* aralığında değiştirilmesi sonucunda H-düzleminde yaklaşık *10°* huzme taraması elde edilmiştir. Eşit yarık aralıklı dizide *25 GHz*'de istenilen *-20 dB* yan huzme seviyesine sahip kalem biçimli huzme elde edilmiştir.

Anahtar Kelimeler: Yüzey Tümleşik Dalga Kılavuzu Anten Dizisi, Yüzey Uyumlu Anten, Yarıklı Dalga Kılavuzu Dizisi, Yürüyen Dalga Anteni, Yarık Anten Dizisi.

To My Family and Ayşe

ACKNOWLEDGEMENTS

I would like to express my acknowledgements to everyone who helped in completing this thesis. First of all, I would like to thank my advisor Prof. Dr. Özlem Aydın Çivi for her invaluable supervision and sharing her deep theoretical background during my research. I am so grateful for gaining much from her vision and approach of dealing with the problems in research. I would like to thank to Prof. Dr. Tayfun Akın for his supervision, encouragement, and guidance. I am also thankful to Prof. Dr. Şimşek Demir for his effort in his supervision and encouragement during my study. I also would like to thank to Prof. Dr. Sencer Koç and Prof. Dr. Altunkan Hızal for sharing their invaluable experiences and suggestions. I also would like to thank to Assoc. Prof. Dr. Lale Alatan for her suggestions which helped to improve the content of my study. I am thankful to Assoc. Prof. Dr. Vakur B. Ertürk for his help, encouragement and positive attitude during my study.

I would like to thank to my friends Onur Gölbaşı, Şerif Kaya, Şenol Reçber, and my cousin Salih Kar for their wonderful friendship and support. I am also thankful to İlker Comart, Çağrı Çetintepe, Özgehan Kılıç, Yaşar Barış Yetkil, Savaş Karadağ, Alper Yalım, Enis Kobal, and Ahmet Kuzubaşlı for their lively friendship and for transforming the microwave research group to a family. I also want to express my sincere thanks to Orçun Kiriş for his support, excellent friendship and being a good companion during this study.

I would also like to extend my deepest gratitude to my family. I would like to thank my father İlhan Bayraktar for his constant encouragement to increase my knowledge and providing invaluable advices. I would like to express my special thanks to my

mother Neriman Bayraktar, and my sister, Emel Mahmutoğlu, for their genuine support, love, and understanding.

Last but certainly not least, my heartfelt thanks go to thank my wife Ayşe Bayraktar for her endless love, support and constant encouragement during my study. Without her, this work would have never been completed.

This work is partially supported by the Scientific and Technical Research Council of Turkey (TÜBİTAK-EEEAG-111R001).

TABLE OF CONTENTS

ABSTRACT v
ÖZ vii
ACKNOWLEDGEMENTS x
TABLE OF CONTENTS xii
LIST OF TABLES xiv
LIST OF FIGURES xv
CHAPTERS
1. INTRODUCTION 1
1.1. Literature Survey on Slotted SIW Antennas 3
1.2. The Traveling Wave Slot Array on CSIW Developed in This Thesis 7
1.3. Thesis Objectives and Organisation 8
2. CHARACTERIZATION OF CSIW AND SINGLE LONGITUDINAL SLOT ON CSIW 11
2.1. Characterization of CSIW 11
2.2. Microstrip to SIW Transition Structure 14
2.3. Characterization of Single Slot on CSIW 17
3. DESIGN PROCEDURE OF SHUNT SLOT ARRAY ON CSIW 27
3.1. Derivation of the Active Admittance Formulas for the Longitudinal Slots on CSIW 27
3.1.1. Modes in the CSIW 28
3.1.2. Active Admittance Formulation of Longitudinal Slot on the CSIW 31
3.1.2.1. Waveguide and Slot Dimensions 32
3.1.2.2. Derivation of the First Active Admittance Formula 34
3.1.2.3. Derivation of the Second Active Admittance Formula 43
3.2. Design Procedure of Slotted CSIW Array 59

3.3. Numerical Results 64
3.3.1. External Couplings of Two Slots on PEC Cylinder 66
3.3.2. External and Internal Couplings of Two Slots on CSIW 70
4. DESIGN OF TRAVELING WAVE CSIW SLOT ARRAY 79
4.1. Pattern Synthesis Methods 80
4.1.1. Aperture Projection Method 81
4.1.1.1. Taylor Line Source Sampling for Planar Arrays 81
4.1.1.2. Taylor Line Source Sampling for Slotted CSIW Array 87
4.2. Slot Array Design on CSIW with Non-Uniform Slot Separation 93
4.2.1. Fabrication and Measurements 101
4.2.1.1. 1 x 16 Optimized Slot Array on CSIW 101
4.2.1.2. 1 x 4 SIW Power Divider 106
4.2.1.3. 4 x 16 Slot Array on CSIW 108
4.3. Slot Array Design on CSIW with Uniform Slot Separation 113
4.3.1. Fabrication and Measurements 132
4.3.1.1. 1 x 25 Slot Array on CSIW 132
5. CONCLUSIONS AND FUTURE WORK 139
REFERENCES 141
APPENDICES
A. SYSTEMATIC CONSTRUCTION OF FIELDS IN BEND REGULAR WAVEGUIDES 147
B. FIELDS RADIATED BY APERTURES ON PEC CYLINDER 151
C. ASYMPTOTIC FORMS OF HANKEL FUNCTION RATIOS FOR LARGE ORDER AND ARGUMENT 155
CURRICULUM VITAE 157

LIST OF TABLES

TABLES

Table 3.1: Eigenvalues, $\in_{mn}$ and μ_{mn}, of TE^{z}_{mn} and TM^{z}_{mn} modes for various *m* and *n* values. (NA: Not Applicable)..... 30

Table 3.2: Comparison of the Y_{pq} values for $z_0 = 0$" with the literature [45]..... 67

Table 3.3: Comparison of the Y_{pq} values for $\phi_0 = 0°$ with the literature [45]. 68

Table 3.4: Comparison of the Y_{pq} values for various z_0 and ϕ_0 values with the literature [45]..... 69

Table 4.1: Slot offsets and lengths of *1 x 16* slot array on CSIW determined by Elliott's design procedure..... 96

Table 4.2: Slot offsets and lengths determined after the optimization of *1 x 16* slot array on CSIW designed by Elliott's design procedure. 100

Table 4.3: Comparison of the simulated efficiency values of optimized *1 x 16* slot array on CSIW..... 100

Table 4.4: Simulated and measured HPBW and cross-polarization values of *1 x 16* slot array on CSIW..... 105

Table 4.5: Simulated and measured HPBW and cross-polarization values of *4 x 16* slot array on CSIW..... 112

Table 4.6: Slot offsets and lengths for *1 x 25* slot array on CSIW (1^{st} design)..... 118

Table 4.7: Slot offsets and lengths for *1 x 25* slot array on CSIW (3^{rd} design). 130

Table 4.8: Slot offsets and lengths for *1 x 25* slot array on CSIW after 6^{th} iteration (3^{rd} design). 131

Table 4.9: Simulated and measured HPBW and cross-polarization values of *1 x 25* slot array on CSIW..... 136

LIST OF FIGURES

FIGURES

Figure 1.1: Slotted CSIW Array..... 2
Figure 1.2: (a) Cross-sectional and (b) top views of the traveling wave slot array on CSIW..... 7
Figure 2.1: (a) SIW structure. (b) Equivalent of SIW..... 12
Figure 2.2: Comparison of the propagation constants found by simulations and closed form expressions..... 14
Figure 2.3: A schematic view of microstrip line to SIW transition..... 15
Figure 2.4: (a) Fabricated microstrip to SIW transition ($L = 2\ cm$). (b) S_{11} and (c) S_{21} results..... 15
Figure 2.5: (a) Fabricated microstrip to SIW transition ($L = 10\ cm$). (b) S_{11} and (c) S_{21} results..... 16
Figure 2.6: TRL calibration standards: (a) Thru (b) Reflect, and (c) Line Standards. 18
Figure 2.7: Circuit model of longitudinal slot on CSIW..... 19
Figure 2.8: *A* and *D*-parameters of the single slot on CSIW for $R = 10\ cm$: (a) real and (b) imaginary parts..... 20
Figure 2.9: *B*-parameters of the single slot on CSIW for $R = 10\ cm$: (a) real and (b) imaginary parts..... 21
Figure 2.10: *C*-parameters of the single slot on CSIW for $R = 10\ cm$: (a) Real and (b) imaginary part of the shunt admittance..... 22
Figure 2.11: Characterization polynomials of the shunt slot on CSIW: (a) Ratios of the admittance to resonant conductance. (b) Normalized Resonant Conductance. (c) Normalized Resonant Length..... 23

Figure 2.12: (a) Fabricated single slot on microstrip to SIW transition ($L = 2\ cm$). (b) S_{11} and (c) S_{21} results. 24
Figure 3.1: E-plane bend regular waveguide. 29
Figure 3.2: Longitudinal slot array on bended regular waveguide. 32
Figure 3.3: Longitudinal slot (p^{th} slot) on bended regular waveguide. 33
Figure 3.4: Bended regular waveguide with no slot (p^{th} slot is covered by conducting tape). 37
Figure 3.5: Circuit model of the longitudinal slot on E-plane bend regular waveguide. 41
Figure 3.6: Longitudinal slot array composed of p^{th} and q^{th} slots on bended regular waveguide. 46
Figure 3.7: (a) Longitudinal slot array with q^{th} slot is covered by conducting tape (case "a"). (b) Equivalent problem. 47
Figure 3.8: (a) Longitudinal slot array composed of p^{th} and q^{th} slots on bended regular waveguide with q^{th} slot is excited (case "b"). (b) Equivalent problem. 50
Figure 3.9: Circuit model representation of a traveling wave shunt slot array. 60
Figure 3.10: Deformed integration path. 64
Figure 3.11: Two slots on cylindrical PEC. 66
Figure 3.12: (a) Longitudinal slots on the same CSIW. (b) Longitudinal slots on two parallel CSIW. 70
Figure 3.13: Circuit model of two longitudinal slots on the same CSIW. 71
Figure 3.14: (a) Magnitude and (b) phase of S_{11} ($R = 10\ cm$, $D_{pq} = 5\ mm$, and $z_q = 0.5\ mm$). 72
Figure 3.15: (a) Magnitude and (b) phase of S_{11} ($R = 10\ cm$, $z_p = 0.2\ mm$, and $z_q = 0.5\ mm$). 73
Figure 3.16: (a) Magnitude and (b) phase of S_{11} ($R = 10\ cm$, $z_p = -0.2\ mm$, and $z_q = 0.5\ mm$). 74
Figure 3.17: (a) Magnitude and (b) phase of S_{11} ($R = 0.6\ cm$, $z_p = -0.2\ mm$, and $z_q = 0.5\ mm$). 74
Figure 3.18: Circuit model of the longitudinal slot on CSIW. 75

Figure 3.19: (a) Magnitude and (b) phase of active S_{11} ($R = 10\ cm$, $z_q = 0.5\ mm$ and $D_w = 6\ mm$). 76
Figure 3.20: (a) Magnitude and (b) phase of active S_{11} ($R = 10\ cm$, $z_p = 0.2\ mm$ and $z_q = 0.5\ mm$). 77
Figure 4.1: Sampling of the Taylor distribution using aperture projection method... 80
Figure 4.2: (a) Sampling Taylor line source distribution randomly with *100* elements. (b) Corresponding radiation patterns. 82
Figure 4.3: (a) Sampling half side of the Taylor line source distribution randomly and allocating symmetric weights for the other half (Total *200* elements). (b) Corresponding radiation patterns. 83
Figure 4.4: (a) Sampling Taylor line source distribution randomly with 1000 elements. (b) Corresponding radiation patterns. 83
Figure 4.5: (a) Sampling Taylor line source distribution uniformly with *11* elements. (b) Corresponding radiation patterns. 84
Figure 4.6: (a) Sampling Taylor line source distribution randomly with *100* elements and adjusting the sampled weights using element density. (b) Corresponding radiation patterns. 85
Figure 4.7: (a) Sampling Taylor line source distribution randomly with *20* elements and adjusting the sampled weights using element density. (b) Corresponding radiation patterns. 86
Figure 4.8: (a) Element positions of the slotted CSIW array and element positions at the projected aperture (*40* element array). (b) Sampling Taylor line source distribution using projected aperture positions. (c) Corresponding radiation patterns for linear arrays. (d) Corresponding radiation patterns for cylindrical slot arrays. 88
Figure 4.9: (a) Radiation patterns for the slotted CSIW array using (a) *-30 dB* and (b) *-40 dB SLL* Taylor weights. 90
Figure 4.10: (a) Element positions of the slotted CSIW array and element positions at the projected aperture (*25* element array). (b) Sampling Taylor line source distribution using projected aperture positions. (c) Corresponding radiation

patterns for linear array. (d) Corresponding radiation patterns for cylindrical slot array. 92
Figure 4.11: (a) Element spacing and (b) calculated patterns of *1 x 16* slot array on CSIW (*R = 10 cm*) for three different slot separation schemes. 94
Figure 4.12: (a) S_{11} and (b) S_{21} results of *1 x 16* SIW slot array on CSIW designed by Elliott's design procedure. 97
Figure 4.13: Simulated radiation patterns of *1 x 16* arrays (a) designed using Elliott's design procedure and (b) optimized array. 98
Figure 4.14: Comparison of the accepted powers and efficiencies of two *1 x 16* array on CSIW (*R = 10 cm*). 99
Figure 4.15: (a) Fabricated traveling wave optimized *1 x 16* slot array on SIW. (b) S_{11} and (c) S_{21} results of the optimized *1 x 16* slotted SIW array. 102
Figure 4.16: Measurement setup of *1 x 16* slot array on CSIW (*R = 10 cm*). 102
Figure 4.17: Radiation patterns of *1 x 16* slot array on CSIW. 104
Figure 4.18: (a) Gain and (b) efficiency results of *1 x 16* SIW slot array. 106
Figure 4.19: (a) Fabricated two back to back *1 x 4* power dividers. (b) S_{11} and (c) S_{21} results of the back to back power divider structure. 107
Figure 4.20: Fabricated traveling wave *4 x 16* slot array on SIW. 108
Figure 4.21: (a) S_{11} and (b) S_{21} results of *4 x 16* SIW slot array. 109
Figure 4.22: Measurement setup of *4 x 16* slot array on CSIW (*R = 10 cm*). 110
Figure 4.23: Radiation patterns of *4 x 16* slot array on CSIW. 111
Figure 4.24: (a) Gain and (b) efficiency results of *4 x 16* SIW slot array. 112
Figure 4.25: The function of the Elliott's design. 114
Figure 4.26: Slot array on bended regular waveguide. 115
Figure 4.27. Phase and error graphs for *1 x 25* slot array on CSIW (*1st* design): (a) Deviation of slot phases from mode voltage phases ($\angle D_p^1$). (b) Deviation of slot phases from mode voltage phases in Elliott's design ($\angle D_p^2$). (c) Error in the Elliot's design. 117
Figure 4.28. Slot voltage (a) amplitudes and (b) phases for *1 x 25* slot array on CSIW. (c) H-plane radiation patterns (*1st* design). 120

Figure 4.29. Slot voltage (a) amplitudes and (b) phases for *1 x 25* slot array on CSIW. (c) H-plane radiation patterns (*2nd* design). (d) Error in the Elliot's design. 125
Figure 4.30. Slot voltage (a) amplitudes and (b) phases for *1 x 25* slot array on CSIW. (c) H-plane radiation patterns (*3rd* design). 128
Figure 4.31. Phase and error graphs for *1 x 25* slot array on CSIW (*3rd* design): (a) Deviation of slot phases from mode voltage phases ($\angle D_p^1$). (b) Deviation of slot phases from mode voltage phases in Elliott's design ($\angle D_p^2$). (c) Error in the Elliot's design. 129
Figure 4.32: (a) Fabricated traveling wave *1 x 25* slot array on SIW. (b) S_{11} and (c) S_{21} results of the *1 x 25* slotted SIW array. 133
Figure 4.33: Measurement setup of *1 x 25* slot array on CSIW (*R = 10 cm*). 133
Figure 4.34: Radiation patterns of *1 x 25* slot array on CSIW. 135
Figure 4.35: (a) Gain and (b) efficiency results of *1 x 25* SIW slot array. 137

CHAPTER 1

INTRODUCTION

Conformal arrays have a specific shape determined by the parameters other than radiation pattern and input match requirements and they can easily be implemented using microstrip technology using a flexible substrate or multifaceted surfaces [1]. However, microstrip arrays can have complex feed networks such as probes feeding patch elements. Series or corporate microstrip feed networks can be used to eliminate this problem but microstrip feed networks suffer from radiation problems. Strip line can be used to eliminate the radiation losses, however, a cross coupling problems are encountered in the feed network with strip line structure. Slotted waveguide arrays (SWA) have some advantages over microstrip antennas such as being low loss, high isolation, and high power handling. Due to these advantages, SWA antennas are widely used in communication and radar systems particularly at microwave wave frequencies. Regarding conformal array applications, microstrip antennas are easier to implement compared to SWA antennas, however, excitation of antenna elements by a waveguide feed network is advantageous compared to microstrip feed network in terms of eliminating radiation losses and cross coupling problems. Moreover, complex feed network structure is not needed in SWA to excite the slots in the same waveguide. Furthermore, the array of waveguides can be formed without cross coupling problems. Recently, a new planar wave guiding structure, namely post wall waveguide or substrate integrated waveguide (SIW) is proposed [2], [3]. Although, dielectric filled SIW suffers from dielectric losses which do not exist in hollow waveguides, SIW takes most of the advantages of regular rectangular waveguides as well as the advantages of microstrip technology such as being low cost and small

size. Moreover, SIW can be easily manufactured using simple printed circuit board (PCB) process which allows monolithic integration of SIW with the other planar circuits. The integration of regular rectangular waveguides with planar feed networks requires complex and bulky integration schemes which require precise manufacturing process difficult to achieve at millimeter wave frequencies. Monolithic integration capability in SIW technology eliminates transition losses due to these complex integration of regular rectangular waveguides with planar feed networks. Due to these advantages, the slotted SIW antennas are good candidates for the conformal array applications especially when SIW is implemented using a flexible substrate.

There is a limited study in the literature on the conformal array applications with slotted waveguide arrays. The aim of this thesis is to analyze, design and implement a traveling wave slot array on a novel cylindrical substrate integrated waveguide (CSIW) structure at K-band where the CSIW lies in the circumferential direction of the cylinder as shown in Figure 1.1.

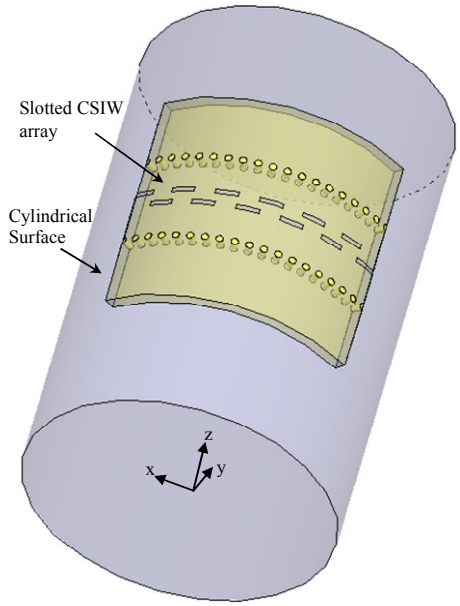

Figure 1.1: Slotted CSIW Array.

The contents of this chapter, in which the traveling wave slot array structure on CSIW is introduced, can be summarized as follows. Section 1.1 gives the overview of the slotted SIW antennas for both planar and conformal array applications in the literature while Section 1.2 presents the traveling wave slot array on CSIW developed in this thesis. Finally, Section 1.3 explains the detailed objectives and organization of the thesis.

1.1. Literature Survey on Slotted SIW Antennas

There has been a growing interest in SIW based antennas in the last few years. Most of the studies regarding SIW slot antennas in the literature employ planar SIW structures [4] - [23]. The first slot waveguide antenna is presented in [4] where *4 x 4* longitudinal standing wave slot array is formed at X-band. The array is fed by *1 x 4* microstrip power divider. The antenna is successfully implemented and measured. Using a SIW based power divider with tapered power division, a low side lobe level (SLL) longitudinal slot array on SIW is implemented in [5] and about *-30 dB* SLL is obtained at X-band. Slotted SIW antennas usually allocate constant spacing between slot elements. In [6], an optimization on the spacing between each element is carried out by using a combination of genetic algorithm and conjugate gradient method for a given pattern and efficiency requirements, and hence, a traveling wave SIW slot array with *10* slots is obtained with about *8 %* bandwidth at X-band. A series slot array is implemented with transverse slots in [7] using half mode SIW to miniaturize the SIW antennas where the SIW is cut from its centerline such that only one wall of the half mode SIW contains periodic vias while the radiation into free space takes place at the other wall. A narrow *10 dB* return loss bandwidth, which is about *275 MHz*, is obtained at X-band because of the standing wave array design. Another standing wave series slot array on SIW with improved bandwidth performance is presented in [8] where *16* element *45°*-inclined alternating reactance slot pairs are allocated to achieve both impedance matching and uniform field excitation. About

990 MHz 10 dB return loss bandwidth is obtained with *24.3 dBi* gain and *53.7 %* efficiency at Ka-band. There are other slotted SIW studies in the literature where beam forming networks are implemented by SIW technology and they are monolithically integrated with SIW slot arrays [9] - [12]. In [9], a standing wave planar SIW slot array is monolithically integrated with SIW *7* input rotman lens for multibeam applications at *28.5 GHz*. The scan coverage is increased by conformal placement of *5* planar multibeam antennas. A *24* beam slot array antenna with *4 x 8* butler matrix is implemented with SIW technology in [10] to achieve *360°* coverage over azimuth and *-14.5 dB* SLL is obtained in all the beam states. The antenna is constructed for multiple input multiple output (MIMO) wireless communications and *3.75 %* bandwidth is obtained at *16 GHz*. The other slot array with *4 x 4* butler matrix implemented at *77 GHz* with SIW technology combines *4* broadband couplers to avoid crossovers [11]. Another example is a compact single layer monopulse SIW slot array presented in [12] where *7.39 %* bandwidth with maximum gain of *18.75 dB* at Ka-band is obtained. The antenna has four ports where each port is responsible form exciting the sum and difference patterns in azimuth, elevation, and diagonal planes.

There are also studies to enhance the efficiency and bandwidth of the SIW slot arrays. Dielectric resonators are allocated on top of slots in [13] to increase bandwidth and efficiency. About *11 dB* gain is obtained with *1 x 4* elements over *4.7 %* bandwidth. In [14], the patch elements are located on top of *4 x 4* slots fed by SIW. The dielectric cubes placed on top of patch elements in [13] are replaced by Yagi-like parasitic director in [14], and hence, difficulties in the fabrication of dielectric cubes are eliminated. In [14], about *7.5 GHz* impedance bandwidth is obtained at W-band with about *18 dB* antenna gain.

There are some SIW leaky wave antenna examples in the literature [15] - [23]. A leaky wave antenna using continuous slot on broad wall of SIW is implemented in [15]. Position of the slot with respect to the center line of the SIW is varied along the

SIW to obtain amplitude taper, and hence, a low SLL about *-30 dB* is obtained at *35 GHz*. The scan ranges of the continuous leaky wave antennas are limited to the forward quadrant only. In order to increase the scan range by radiating into both forward and backward quadrants, periodic and metamaterial based leaky wave antennas are employed [16] - [23]. SIW based periodic leaky wave antenna is first proposed in [16] where the leakage is obtained by increasing the spacing of the vias at one side of SIW. The same type of leaky wave antenna is implemented in [17] by rarely spacing the vias at both sides of the SIW and first higher order mode is used in the SIW structure to obtain better leakage constant compared to fundamental mode of the SIW at Ka-band. A miniaturized leaky wave antenna using half mode SIW is proposed in [18]. In [18], a quasi-omnidirectional pattern at *28 GHz* is obtained with an input match below *-14 dB* between *24.5 GHz* and *29.5 GHz*. Another half mode SIW leaky wave antenna is developed in [19] to obtain *4* different polarization states at Ka-band. The antenna provides an input match better than *-20 dB* for all the polarization states and also it achieves about *30°* beam steering by sweeping the frequency between *33 GHz* and *39 GHz*. A very large frequency scanning about *130°* is obtained in [20] by using composite right/left handed metamaterial on broad wall of SIW when the frequency is swept between *8.5 GHz* and *12 GHz* where *-10 dB* input match is also satisfied in the band. In [20], the same antenna is also implemented using half mode SIW, and hence, the efficiency is increased to *87 %*. Another SIW leaky wave antenna which contains right/left handed metamaterial is presented in [21] to obtain *6* different polarization states with increased scan range compared to the one presented in [19]. A gain reduction problem near the broadside of the metamaterial based leaky wave antennas is studied in [22] and gain values above *9 dBi* is obtained between *8 GHz* and *13 GHz* by using patch elements inserted below radiating slots in SIW. Moreover, the same structure is also used to improve the boresight bandwidth in [23] by slowing down the rapid transition from backward quadrant to forward quadrant in the metamaterial based leaky wave antennas.

In the literature, most of the studies related to conformal waveguide arrays employ regular rectangular waveguides [24] - [27] and there are limited studies with the SIW conformal arrays [9], [28], [29]. An analytic design procedure is developed in [24] for dielectric filled waveguide small slot arrays and *6 x 9* conformal waveguide slot array is implemented at *9.34 GHz*. Another waveguide with edge wall slot array is designed and fabricated in [25]. A large beam steering about *84°* from broadside is obtained with *-13 dB* side lobe level (SLL). The radar cross section of the conformal slot array in [26] is computed using method of moments (MoM) but the slot array is not implemented. All of these slotted waveguide antennas have sectoral cross section extends parallel to the cylinder axis. A conformal waveguide slot array where planar waveguides are placed around the cylinder tangent to the circumferential direction is formed at Ku band using narrow wall slots for *360°* azimuth tracking in [27]; however, this antenna is multifaceted, i.e., planar slotted waveguides are used to form the conformal array. There are also conformal slot array examples in the literature using SIW, however, none of them employs SIW fully conformed around the cylinder in the circumferential direction. The conformal SIW array presented in [9] is multifaceted and planar SIW slot antennas are used to increase the scan coverage. In the other conformal SIW array application, a *4 x 4* slotted SIW array is formed using a flexible substrate and *11 dB* gain is obtained for planar case at *79 GHz* [28]. However, no effort has been made in the design of this antenna to place it on a prescribed conformal surface; it is fabricated only on a flexible substrate. Another SIW conformal array is presented in [29]. The array shows the design and implementation of a shaped beam slotted SIW antenna on cylindrical surface. A flat topped fan beam is obtained with about *38°* half power beam width (HPBW) in E-plane at *35 GHz*. However, the conformal slotted SIW array is formed by using a SIW having sectoral cross-section which extends in the axial direction of the cylinder.

1.2. The Traveling Wave Slot Array on CSIW Developed in This Thesis

The traveling wave slot array on CSIW structure examined in this thesis is shown in Figure 1.2. The array is designed to operate at K-band. The CSIW is formed by conformal placement of the planar SIW on a cylindrical surface in the circumferential direction. The periodic placement of the vias mimics the side walls of the regular rectangular waveguide. The longitudinal slot antennas are placed on the broad wall of the CSIW to radiate into free space. The array is excited from Port 1 and Port 2 is terminated by a match load to obtain a traveling wave array. When the frequency is varied, steering in the main beam direction in H-plane of the slot array

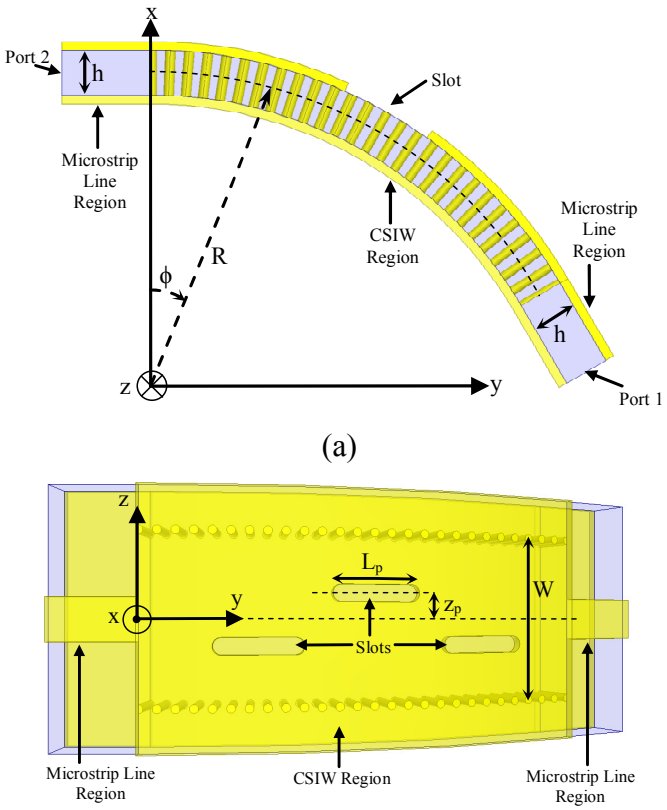

Figure 1.2: (a) Cross-sectional and (b) top views of the traveling wave slot array on CSIW.

can be obtained which eliminates allocating phase shifters used in phased arrays for beam steering. The steering in the E-plane can be achieved by constructing the arrays of CSIW structures and using phase shifters for each CSIW in the array.

In this thesis, different designs of slotted CSIW arrays are carried out at *25 GHz* using non-uniform and uniform slot separations on CSIW. In both of the slot separation cases, the directivity is increased by using proper slot phase values. The non-uniform slot array is designed for beam steering applications while the uniform slot array is examined for pattern synthesis problem. In the non-uniform slot array, the slot elements near resonance are used and the slot separations are designed to adjust slot phases to increase directivity while required slot phases are obtained by using slots with large deviation from resonance in the uniform slot array. Both non-uniform and uniform slot arrays are fabricated on CSIW using standard printed circuit board (PCB) process. The measurement results of the fabricated antennas show that the non-uniform slot array has about *10°* frequency steering in H-plane when the frequency is swept between *24 GHz* and *26 GHz*. In the uniform slot array, a pencil beam pattern is synthesized with a SLL below *-20 dB*. These are the first slotted cylindrical SIW arrays presented in the literature.

1.3. Thesis Objectives and Organisation

The main goal of this thesis is to design, analyze, and implement a traveling wave slot array on a cylindrical substrate integrated waveguide (CSIW) where the SIW lies in the circumferential direction of the cylinder. The specific objectives in the frame of this thesis are summarized as follows:

- Characterization of CSIW and single slot on CSIW.

A propagation constant of the fundamental mode excited in CSIW is determined and the effect of radius of curvature on the propagation constant is examined. Single slot is the basic antenna structure used in the array. The circuit model of a single slot is extracted and self-slot admittance values to be used in the design of the array are calculated for various slot lengths and offsets.

- Mutual coupling and active admittance formulations.

  The active admittance formulas are needed in the Elliott's design procedure to determine the slot offsets and lengths in the slotted CSIW array. The external and internal mutual coupling formulations of the slots on CSIW are carried out and the active admittance formulas are derived.

- Design of traveling wave slot arrays on CSIW

  Slotted CSIW arrays are designed for beam steering and pattern synthesis applications using non-uniform and uniform slot separations, respectively. Designed arrays are fabricated using conventional PCB manufacturing techniques.

  Beam steering is achieved by varying the frequency in the non-uniform slot array. Pattern synthesis procedure is developed for slotted CSIW arrays with uniform slot separation. A few arrays are designed and fabricated to realize low side lobe level, narrow beam width radiation patterns.

This thesis consists of four chapters explaining the accomplishments of the mentioned objectives. After this introduction chapter, the effect of radius on the propagation constant of the fundamental mode in CSIW is examined in Chapter 2.

Moreover, the characterization of the single slot is carried out using a shunt admittance model.

Chapter 3 presents the derivations of active admittance formulas by taking both internal and external couplings into account. Then, the design steps of the slotted CSIW array using derived active admittance formulas are listed. Finally, the case studies related to the mutual couplings of the slots on perfect electric conductor (PEC) cylinder and the mutual couplings of the slots on CSIW are examined. The mutual couplings are calculated using derived coupling formulas for different cases and they are compared with the simulations and literature to validate them.

Chapter 4 describes the design of slotted CSIW arrays. The slotted CSIW arrays are designed for beam steering and pattern synthesis applications. One slotted CSIW array is designed for frequency steering and the other designs are carried out to obtain pencil beam pattern with low SLL. The fabrication and measurement results of the designed slotted CSIW arrays are also presented in the chapter.

Chapter 5 concludes the results of this study with a discussion on possible suggestions of the future improvements.

CHAPTER 2

CHARACTERIZATION OF CSIW AND SINGLE LONGITUDINAL SLOT ON CSIW

This chapter introduces the SIW structures used in the final design of the traveling wave slot array on CSIW. Section 2.1 gives the CSIW parameters used in this thesis and examines the propagation constant of the fundamental mode in the CSIW for different radius of curvature values while Section 2.2 presents the microstrip to SIW transition structure and loss calculation in the SIW. Finally, Section 2.3 introduces the circuit model of the longitudinal slot and characterization of the single slot element on the CSIW.

2.1. Characterization of CSIW

SIW is a waveguide structure the walls of which are formed by periodically located metallic vias with period, p and diameter, d, as shown in Figure 2.1 (a). The width of the SIW, W, which is usually greater than the substrate height, h, determines the cutoff frequency. A SIW can be modelled by a regular rectangular waveguide as shown in Figure 2.1 (b) where the waveguide have the same dielectric filling and waveguide height, h, as in the SIW. The width of the waveguide, W_{eff}, is equal to the equivalent width of the SIW determined by the period and diameter of the vias as well as the width of the SIW, [30]. Using this equivalence, the propagation constant

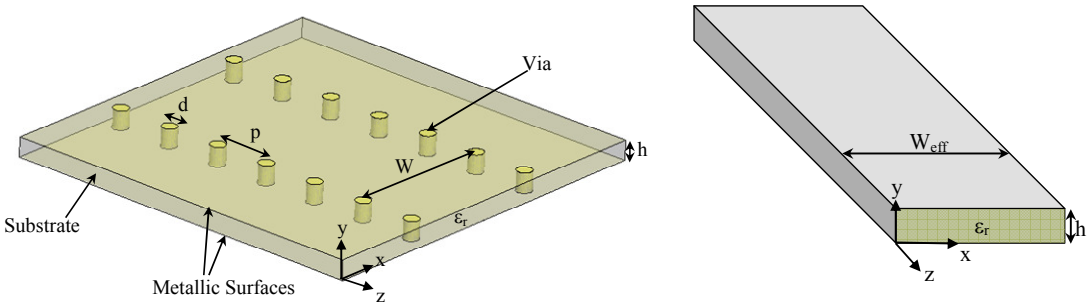

(a) (b)

Figure 2.1: (a) SIW structure. (b) Equivalent of SIW

of the modes in the SIW can be calculated using closed form expressions derived for the waveguides.

The SIW structure used in the slotted CSIW array developed in this thesis is built on Rogers *3003* substrate ($\varepsilon_r = 3$, $tan\delta = 0.0013$ *at 10 GHz*) with thickness, $h = 0.5$ *mm*. The width of the SIW, W, is measured from the centers of the vias and it is chosen as *6 mm* which is half a free space wavelength ($\lambda_0/2$) at *25 GHz* to avoid grating lobes in the E-plane when the array of slotted CSIW is formed. Using *6 mm* SIW width, only the fundamental mode propagates at *25 GHz* in the SIW which is required in the design of the CSIW array. The period and the diameters of the vias are important parameters responsible from the leakage of the electromagnetic field. The dimensions of vias are determined by considering the fabrication tolerances as well as obtaining a good electrical performance. Via diameters should not be too small so that the vias can be successfully drilled and electroplated in PCB process. In order to use the space on the substrate efficiently, large via diameter values should be avoided. The period of the vias should be small enough to have low leakage loss. However, the distance between two vias should be large enough to have enough strength of the structure to avoid any defects in the fabrication. Considering these

fabrication and electrical performance criteria, the period, p, and diameter, d, of the vias are determined as *1 mm* and *0.8 mm*, respectively.

The propagation constant determines the excitation phases of the slot elements and it is an important parameter used in the design of slotted CSIW array. Using the closed form expressions given in [4], the equivalent width of the SIW shown in Figure 2.1 (a) is calculated. In the calculation of the equivalent width, the SIW parameters mentioned for the slotted CSIW array is used. By choosing the width of the SIW, $W = 6\ mm$, only the fundamental mode is allowed to propagate between *16 GHz* and *32 GHz*. Hence, the propagation constant is obtained for the fundamental mode in planar SIW using the equivalent width in the standard closed form formulas for the waveguides, [31]. The attenuation constant is ignored in the calculations. The propagation constant formulations for the fundamental mode of the rectangular waveguide bent in its E- or H-plane is presented in [32]. After finding the equivalent width of the CSIW bent over its E-plane as shown in Figure 1.2, the propagation constant of the fundamental mode in CSIW is calculated for different values of radius, R, between *5 cm* and *15 cm* using the equivalent width of the CSIW and the formulations derived for E-plane bend regular waveguides given in [32]. By considering about *4 mm* resonant length of the slots at *25 GHz* and the element spacing, the radius values above *5 cm* is useful for cylindrical array applications at *25 GHz* to have enough number of array elements to obtain good matching as well as satisfying some pattern requirements such as high directivity. The propagation constant values calculated using closed form expressions for the planar case and for different radius of curvature values are compared in Figure 2.2. As it can be seen in Figure 2.2, there is almost no difference between the results for the radius values above *5 cm* and planar case.

The simulations of the propagation constant of CSIW are carried out in Ansys High Frequency Structure Simulator (HFSS) to compare with the propagation constants obtained from closed form expressions. The CSIW structure shown in Figure 1.2 is

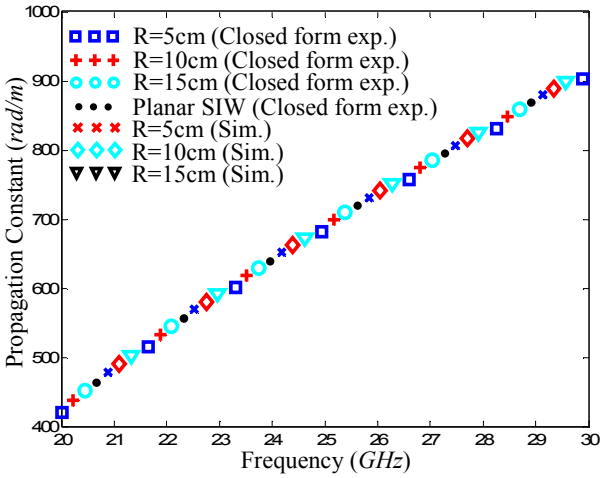

Figure 2.2: Comparison of the propagation constants found by simulations and closed form expressions.

simulated without slots and microstrip parts in HFSS. The CSIW is excited by the wave port in HFSS representing a regular rectangular waveguide coming from infinity having width equal to the equivalent width of the SIW to reduce reflections. The propagation constants are derived from simulated phase of S_{21} results of the structure for various radius values as shown in Figure 2.2. As it is seen in Figure 2.2, it can be concluded that the simulated propagation constants are nearly the same as the ones calculated by closed form expressions.

2.2. Microstrip to SIW Transition Structure

A transition from microstrip line to SIW structure is needed to plug connectors to the microstrip lines and then to be able to measure the SIW devices by the network analyzer. A transition structure designed for the traveling wave antenna study is composed of a microstrip line linearly tapered till the one side of the SIW as shown in Figure 2.3. A $50\ \Omega$ microstrip line have width, $W_f = 1.25\ mm$ and length,

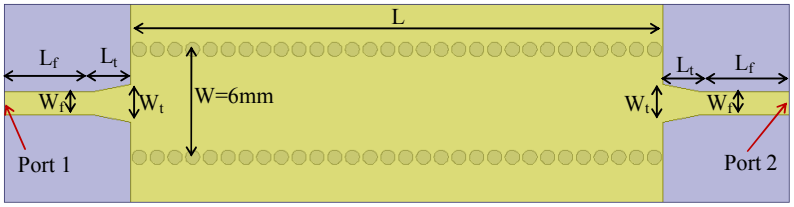

Figure 2.3: A schematic view of microstrip line to SIW transition.

$L_f = 4\ mm$. The tapered section with dimensions, $W_t = L_t = 2.1\ mm$ is connected to SIW with length, L. Both microstrip line and SIW is built on *0.5 mm*-thick Rogers *3003* substrate. The same SIW parameters as mentioned in Section 2.1 are used.

The designed transition structure with length, $L = 2\ cm$ is fabricated using standard PCB process and it is shown in Figure 2.4 (a). The structure is measured using *2.92*

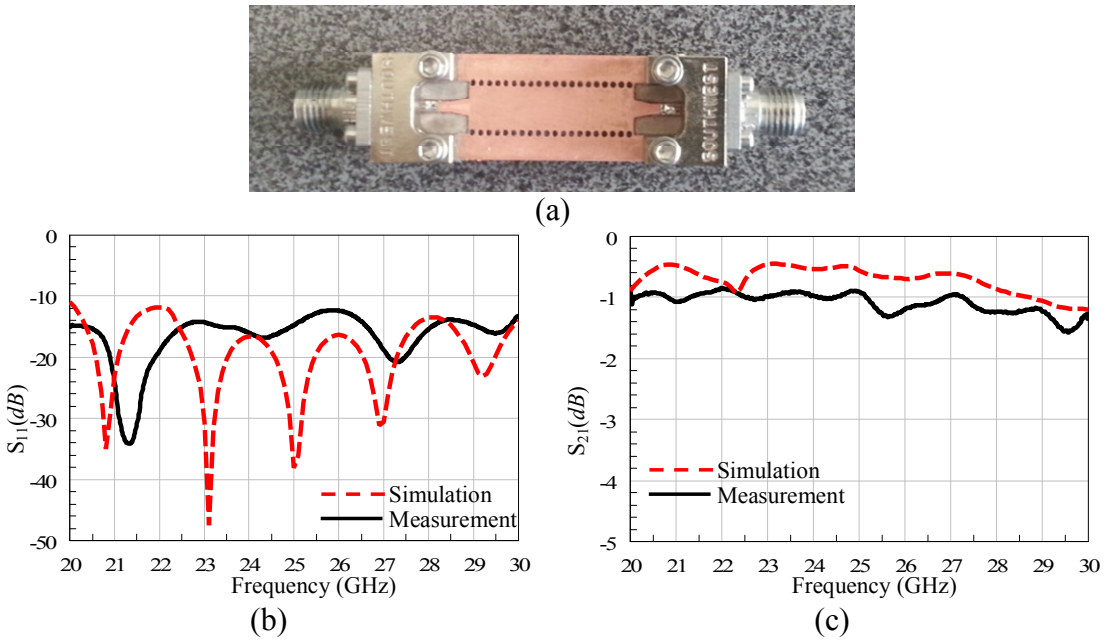

Figure 2.4: (a) Fabricated microstrip to SIW transition ($L = 2\ cm$). (b) S_{11} and (c) S_{21} results.

mm end launch connectors operating till *40 GHz*. The measured results are compared with the simulations in Figure 2.4 (b) and (c). As it can be seen in Figure 2.4 (b) and (c), there is a good agreement between measured and simulated results where the effect of the connectors is taken into account in the simulations. The measured return loss is better than *10 dB* between *20 GHz* and *30 GHz*. Measured insertion loss is about *0.91 dB* at *25 GHz* and the simulations of the structure with connectors shows about *0.57 dB* insertion loss which is quite close to the measured one.

The other transition structure with length, $L = 10\ cm$ is also fabricated in which the other parameters are the same with the transition structure shown in Figure 2.4 (a). The fabricated transition is presented in Figure 2.5 (a). The simulations of the structure with connectors are carried out and they are compared with the measurements as shown in Figure 2.5 (b) and (c). A good agreement between the

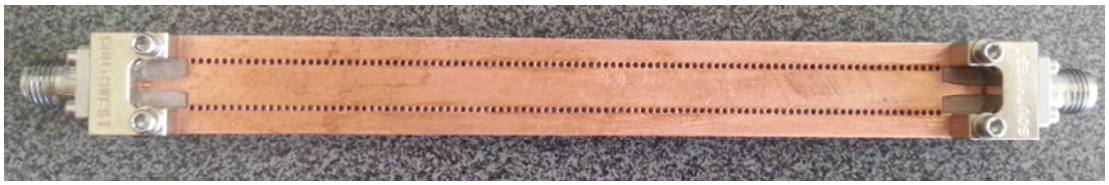

(a)

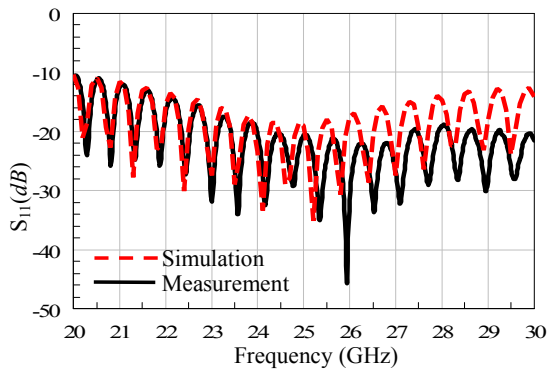

(b)

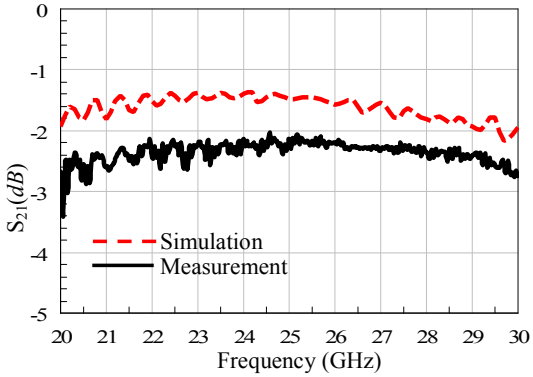

(c)

Figure 2.5: (a) Fabricated microstrip to SIW transition ($L = 10\ cm$). (b) S_{11} and (c) S_{21} results.

measured and simulated s-parameters of the structure is obtained especially in the S_{11} parameters shown in Figure 2.5 (b). Measured and simulated insertion losses of the structure at *25 GHz* are found as *2.13 dB* and *1.48 dB*, respectively. In order to understand the small differences between the simulations and measurements, many fabrications are carried out for the devices and highly non-uniform manufacturing is observed between the same samples in the same fabrication cycle, i.e., yield of the fabrication is low. Devices that give the best results are chosen, and hence, fabrication process might need to be improved further for better results.

Using the measured insertion loss values for the transition structures with *2 cm* and *10 cm* SIW lengths, the loss inside the SIW is calculated as *0.153 dB/cm* at *25 GHz*. Hence, the measured losses due to the microstrip feed line with length, $L_f = 4\ mm$, and the transition part with length, $L_t = 2.1\ mm$ are calculated as about *0.3 dB* for one sided transition at *25 GHz*. The loss inside the SIW includes dielectric and conductor losses while the losses at the transition part include dielectric, conductor, and radiation losses due to the discontinuity encountered in the microstrip transition.

2.3. Characterization of Single Slot on CSIW

Characterization of the single slot is one of the important steps in designing the slotted waveguide array. It is known that longitudinal slot on broad face of planar rectangular waveguide is modeled as shunt admittance [33]. When the other slots are absent in the array, the shunt admittance of single slot does not contain the effects of mutual couplings, hence the admittance of single slot is called self-slot admittance. Since the cross sections of the planar SIW and CSIW are the same and the length of the slot is small compared to the radius of curvature, the shunt admittance model is not affected much by the radius. Hence, a longitudinal slot on CSIW can also be modeled as shunt admittance. In the planar regular rectangular waveguide case, the circuit model of the slot can be extracted by feeding the structure using a wave port

and embedding the ports till the slot reference plane in the simulator. However, in the simulation of CSIW, there is no port parameter calculation in HFSS for both cylindrical waveguide structures and planar SIW. Hence, Thru-Reflect-Line (TRL) calibration standards shown in Figure 2.6 are used to extract the circuit model of single slot on CSIW.

The circuit model of a longitudinal slot on CSIW is extracted using the parameters of

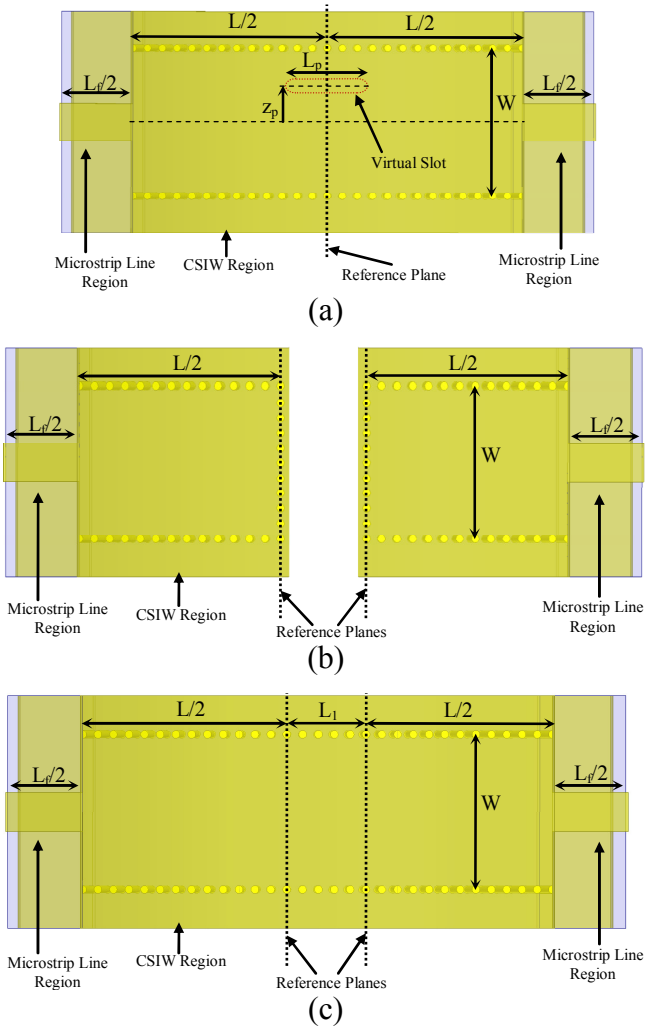

Figure 2.6: TRL calibration standards: (a) Thru (b) Reflect, and (c) Line Standards.

the SIW given in Section 2.1. The CSIW is placed on a cylindrical surface with radius $R = 10\ cm$ as shown in Figure 1.2 and single slot is assumed to exist on the CSIW. Moreover, only $\hat{a}_z$-directed electrical field is assumed in the slot region [34]. TRL calibration standards shown in Figure 2.6 are also placed on cylindrical surface with radius $R = 10\ cm$ to eliminate the effect of the transition from microstrip line to CSIW and to extract the slot admittance. The slot width should be small in order not to disturb the fundamental mode in CSIW. Moreover, narrow slot assumption which assumes only $\hat{a}_z$-directed electrical field in the slot region shown in Figure 1.2 can be achieved better by reducing the width of the slot [34]. By considering the fabrication tolerances and mentioned electrical criteria, the width of the slot, w^s, is chosen as $0.25\ mm$. A single slot having width of $w^s = 0.25\ mm$ is placed on a Thru standard with length L as indicated in Figure 2.6 (a) where the slot center is located at the reference plane which cuts the CSIW two equal pieces with CSIW length $L/2$. The length and offset of the p^{th} slot are abbreviated as L_p and z_p, respectively, as shown in Figure 1.2 (b) and Figure 2.6 (a). The effects of curved edges, which are encountered in PCB milling process in the fabrication, are taken into account by properly rounding the edges of the slots in the simulations. The slot length, L_p extends till the rounded edges of the slots.

The circuit model of single longitudinal slot placed on the CSIW is assumed to be a shunt admittance as shown in Figure 2.7 where Y_s/G_0 is the normalized self-admittance of the slot, where G_0 and γ are the characteristic impedance and the

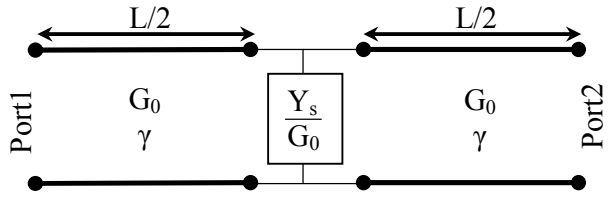

Figure 2.7: Circuit model of longitudinal slot on CSIW.

propagation constant of the CSIW, respectively. The CSIW with single slot simulations are carried out for different slot offsets, z_p and lengths, L_p at *25 GHz* for $R = 10\ cm$. The simulations of the TRL standards without the slot are also carried out at *25 GHz* for $R = 10\ cm$ and the *ABCD* parameters of the slot are extracted for different slot offsets and lengths. Extracted *A*, *D* parameters are shown in Figure 2.8 while *B*-parameters are presented in Figure 2.9. As it is seen in Figure 2.8 and Figure 2.9, *A*- and *D*-parameters are close to unity and *B*-parameters are close to zero for slot offsets till *0.5 mm* and slot lengths around resonance, which is the case for shunt admittance. Hence, it is proved that the longitudinal slot on CSIW can also be modeled as shunt admittance.

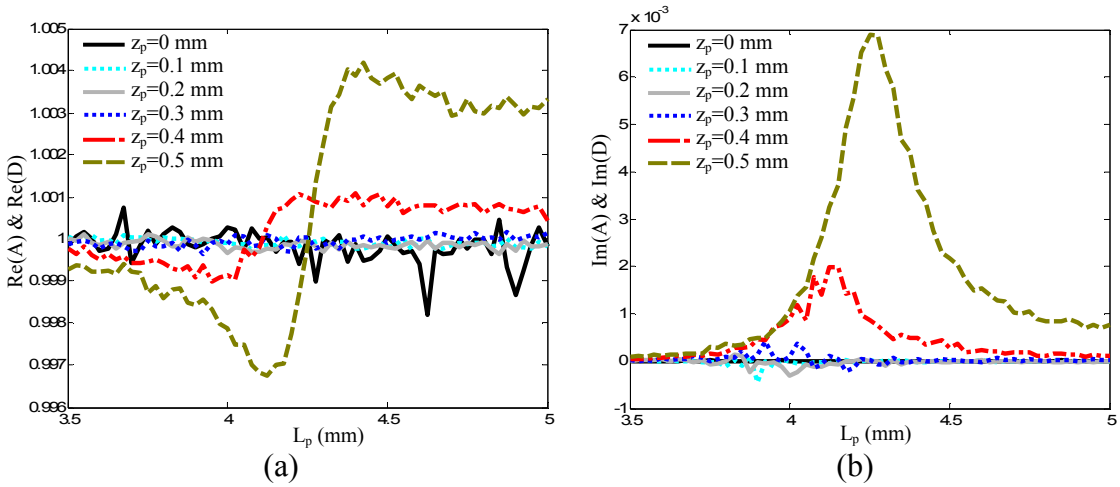

Figure 2.8: *A* and *D*-parameters of the single slot on CSIW for $R = 10\ cm$: (a) real and (b) imaginary parts.

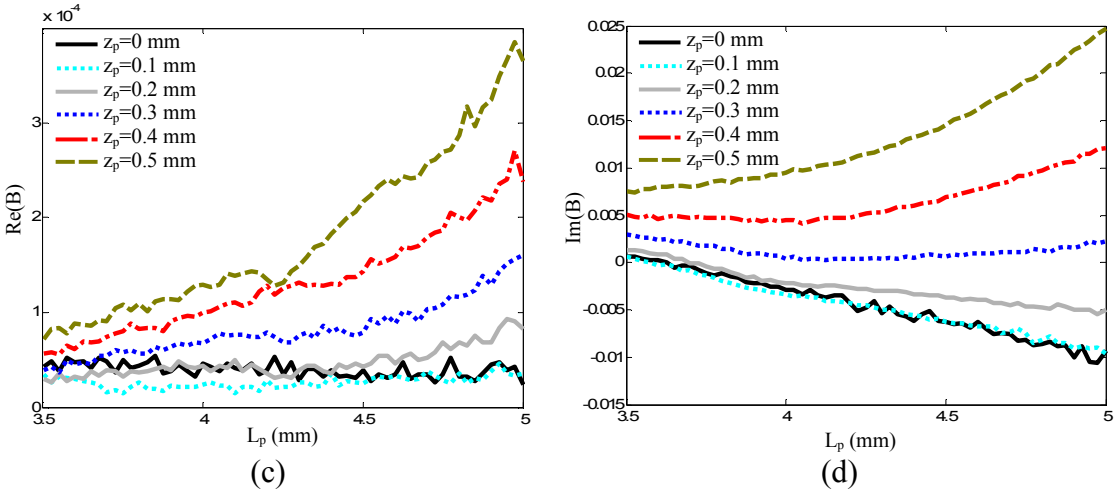

Figure 2.9: *B*-parameters of the single slot on CSIW for *R = 10 cm*: (a) real and (b) imaginary parts.

The shunt admittance values of the slot are equal to the *C*-parameters. *C*-parameters, i.e, real (G_s/G_0) and imaginary (B_s/G_0) parts of the normalized shunt admittance, Y_s/G_0, are given in Figure 2.10. It can be concluded from Figure 2.10 that the resonant conductance and the resonant length increase with the slot offset [35]. In the design of a slotted CSIW array, the desired complex slot voltage distribution is determined by the pattern requirements. Then the desired active admittance values corresponding to the desired slot voltage distribution are determined. After that the slot offsets and lengths which satisfy desired active admittance values are found. Hence, the slot admittance values calculated between discrete slot offset and length values might be needed to sustain desired excitation voltage. So, it is useful to derive the characterization polynomials using Figure 2.10 to be able to extract any slot admittance that corresponds to any slot offset till *0.5 mm* and any slot length between *3.5 mm* and *5 mm*. The accuracy of the characterization polynomials increases as the number of slot offset and length values to carry out simulations is increased. For this reason, the simulations are carried out with *0.1 mm* slot offset steps and *0.025 mm*

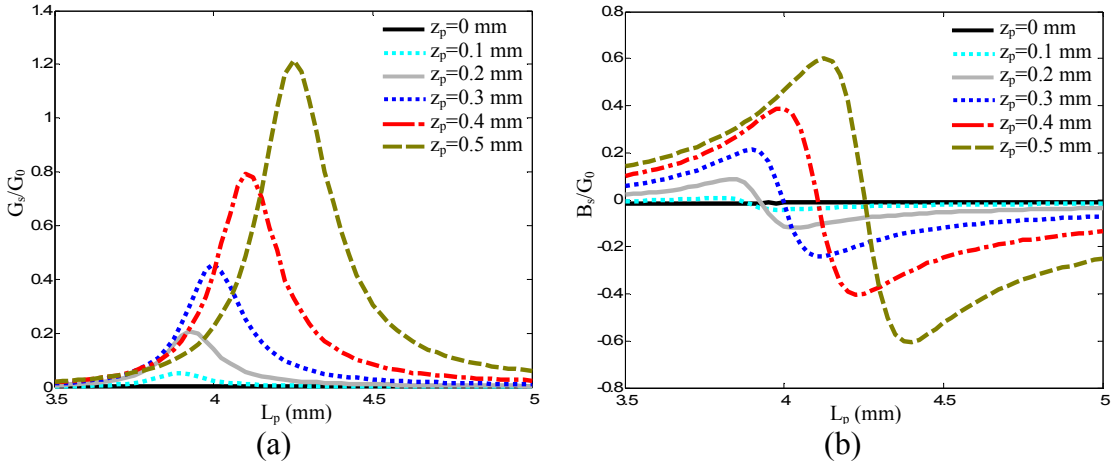

Figure 2.10: *C*-parameters of the single slot on CSIW for *R = 10 cm*: (a) Real and (b) imaginary part of the shunt admittance.

slot length steps which are dense enough for good interpolation between discretely calculated values.

The characterization polynomials are derived by using the curves for different slot offsets shown in Figure 2.10. The first characterization polynomial curves are determined as follows. First of all, the slot lengths are normalized with respect to the resonant length, L_r. After that, the conductance, G_s and susceptance, B_s values are normalized with respect to the resonant conductance, G_r. These calculations are carried out for different slot offset values and the first characterization polynomial curve shown in Figure 2.11 (a) is found by taking the average of the curves. The second and third characterization polynomial curves are the normalized resonant conductance, G_r/G_0 and the normalized resonant lengths, kL_r values as a function of the slot offset as shown in Figure 2.11 (b) and (c), respectively, where k is the wavenumber in the CSIW [33]. The characterization polynomials are determined by finding the polynomial coefficients of the curves shown in Figure 2.11.

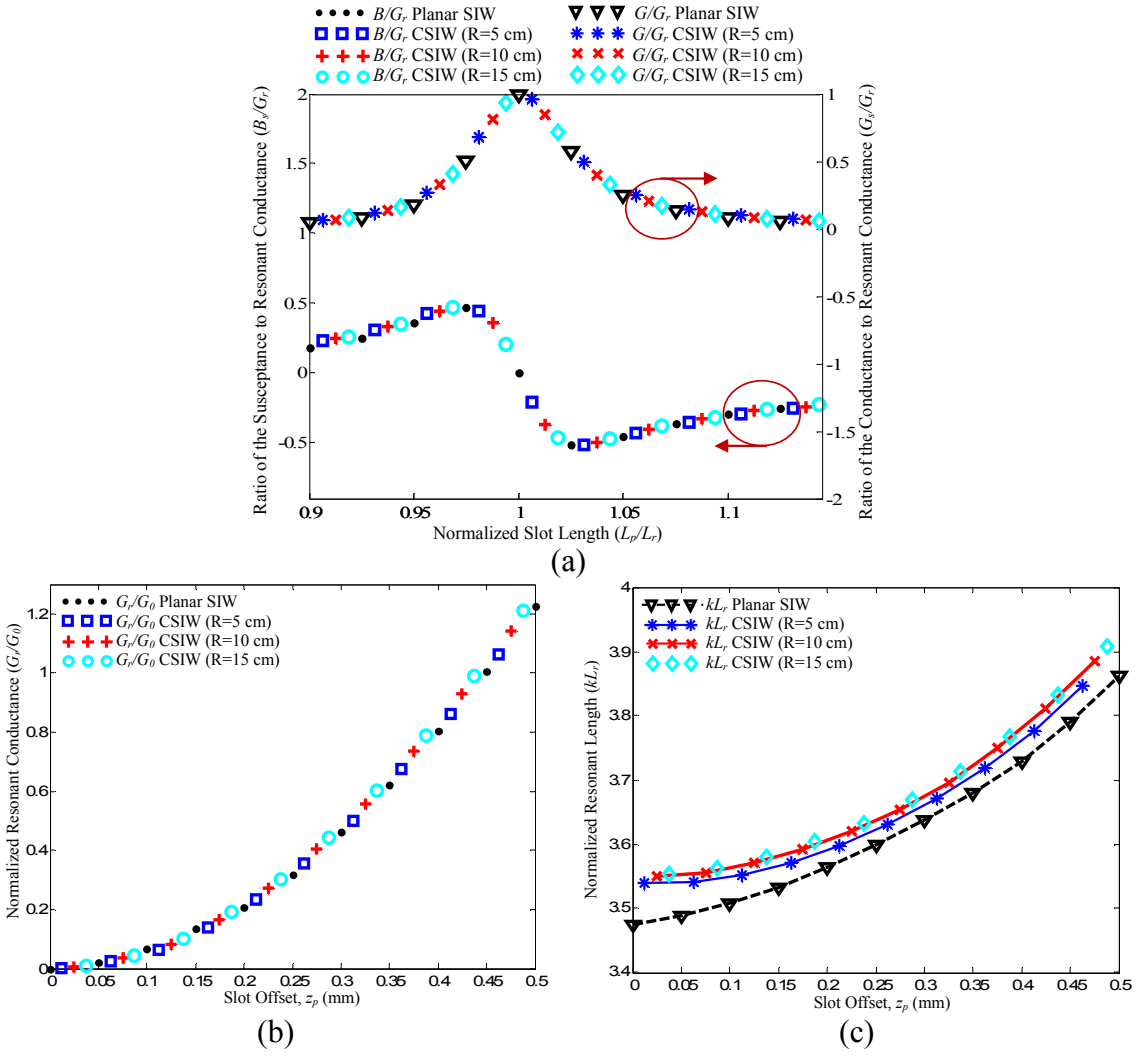

Figure 2.11: Characterization polynomials of the shunt slot on CSIW: (a) Ratios of the admittance to resonant conductance. (b) Normalized Resonant Conductance. (c) Normalized Resonant Length.

The longitudinal slot characterization is carried out for $R = 5\ cm$, $R = 15\ cm$, and planar case. The characterization polynomials are determined for these cases and they are presented in Figure 2.11. As it is seen in Figure 2.11, there is almost no difference between different radius values. The radius values affect the resonant length of the slot, especially for the small slot offset values.

A single slot is designed and fabricated on the SIW transition structure with length, $L = 2\ cm$ shown in Figure 2.4 (a). The fabricated single slot on the SIW transition structure is shown in Figure 2.12 (a). The single slot has slot offset, $z_p = 0.5\ mm$ and slot width, $w^s = 0.25\ mm$. The length of the slot is $L_p = 4.3423\ mm$ which is the resonant length of the slot for $0.5\ mm$ slot offset determined from Figure 2.10. The measured s-parameters of the single slot is compared with the simulations in Figure 2.12 (b) and (c). Good agreement between the simulated and measured values is obtained. In Figure 2.12 (b), the S_{11}-parameters are slightly above $-10\ dB$ at some frequency points. Compared to the S_{11}-parameters of the transition structure with no slots shown in Figure 2.4 (b), the input match is disturbed by the existence of the slot in Figure 2.12 (b) which is an expected result because of the shunt admittance value introduced by the slot. In the slot array design, slot offsets and spacings should be

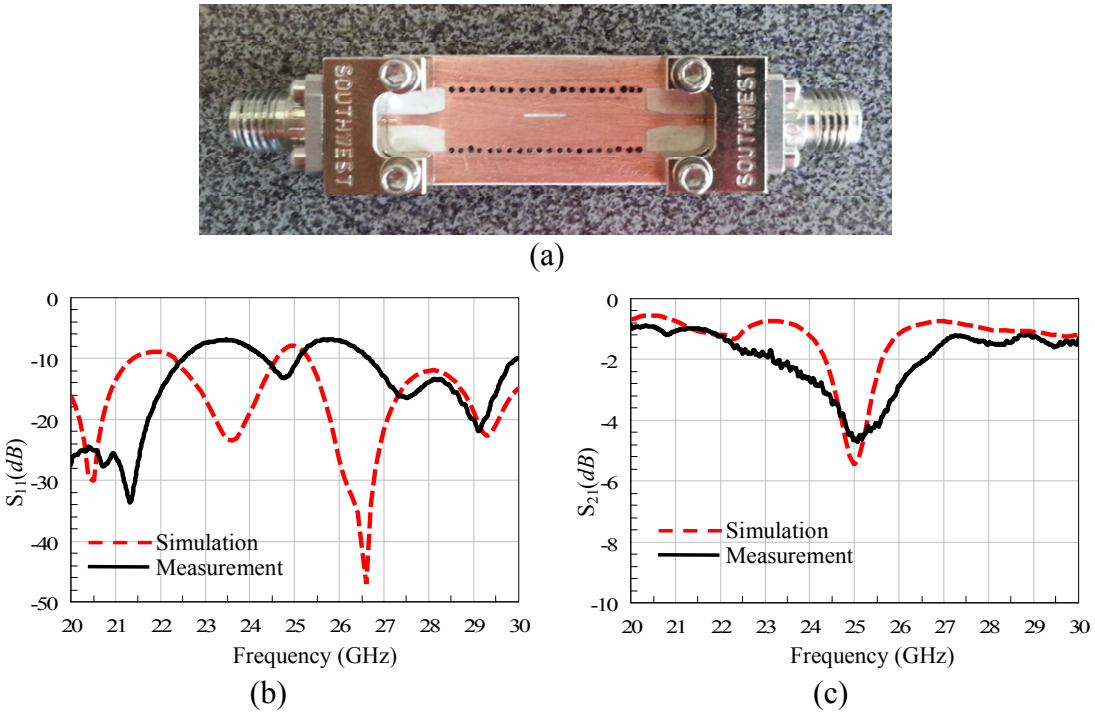

Figure 2.12: (a) Fabricated single slot on microstrip to SIW transition ($L = 2\ cm$). (b) S_{11} and (c) S_{21} results.

properly designed so that total admittance seen by excitation side of the array should be close to characteristic impedance of the waveguide to avoid mismatch caused by the slots. The effect of the other slots on shunt admittance model should also be taken into account in the design as described in Chapter 3.

CHAPTER 3

DESIGN PROCEDURE OF SHUNT SLOT ARRAY ON CSIW

This chapter presents the derivation of the active admittance formulas of the longitudinal slots on broad wall of E-plane bend regular waveguide by taking the external and internal couplings into account. Section 3.1 presents the description and formulation of the problem and the derivation of the active admittance formulas while Section 3.2 explains the design procedure for the slotted CSIW arrays using derived active admittances. Section 3.3 gives the numerical results for the coupling of the slots on cylindrical surface and on CSIW.

3.1. Derivation of the Active Admittance Formulas for the Longitudinal Slots on CSIW

The characterization of the single slot on CSIW is carried out in Section 2.3. As it is stated in Section 2.3, the admittance of the single slot on CSIW is called self-slot admittance since the other slots are absent in CSIW. When the other slots are present in the array, the self-slot admittance values used to present the longitudinal slots are disturbed by the mutual couplings and the slots are presented by the active slot admittance values. In other words, the active slot admittance is the admittance of the slot when the other slots are present in the array. The active admittance is also assumed to be shunt admittance like in the self-admittance circuit model. The active admittance is found by considering both the external and internal couplings in the

slotted CSIW array. The slot couplings through free space outside the SIW are considered as external couplings while the slot couplings through the path inside the SIW are called internal couplings.

The active admittance formulas containing the external and internal mutual couplings of the slots are important parameters used in the Elliott's design procedure [34], [36]. The active admittance formulas derived in [34] and [36] contains the self-slot admittance terms and the mutual coupling terms for the planar slotted waveguide antennas. Similar to the planar slotted waveguides, the active admittance formulas for slotted CSIW antennas can be derived by the help of reciprocity theorem. The fundamental mode and higher order modes are used in the derivation of the active admittance formulas. So, it is proper to examine the mode characteristics in the CSIW before the derivation of the active admittance formulas.

3.1.1. Modes in the CSIW

The CSIW used in this study resembles E-plane bend regular waveguides. The E-plane bend regular waveguides differ only in containing the continuous walls compared to the CSIW. The schematic view of the E-plane bend regular waveguide is presented in Figure 3.1. The bended regular waveguide has PEC boundaries at $\rho = \rho_1, \rho_2$ and $z = 0, a$. Since traveling wave slot array is examined in this thesis, the E-plane waveguide is assumed to be excited from one end and it is matched at $\phi = \phi_1, \phi_2$. The E-plane bend regular waveguide is formed by bending the regular rectangular waveguide on cylindrical surface such that its broad wall with length a lies parallel to the z-axis as shown in Figure 3.1, [32]. Since the CSIW presented in Figure 1.2 is bended in a similar manner, the modes inside the CSIW can be examined using the E-plane bend regular waveguides. Because the waveguide is bended, the hybrid mode fields, i.e., transverse magnetic to $\hat{a}_z$-direction (TM^z_{mn}) and

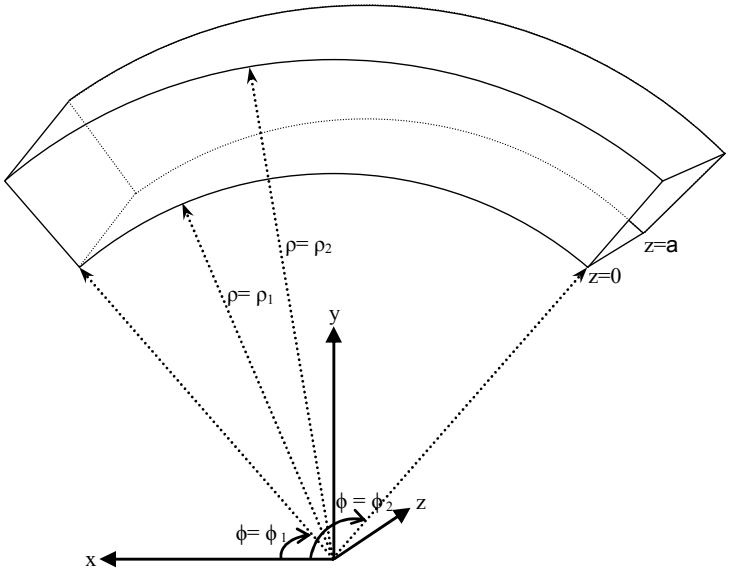

Figure 3.1: E-plane bend regular waveguide.

transverse electric to $\hat{a}_z$-direction (TE^z_{mn}), exist in the bend regular waveguides [37]. Using the systematic construction of fields [38], TM^z_{mn} and TE^z_{mn} mode field components are derived for the E-plane bend regular waveguide in Appendix A. These field components are used in the application of reciprocity theorem to find the active admittance formulas.

The eigenvalues, $\in_{mn}$ and μ_{mn}, for TM^z_{mn} and TE^z_{mn} modes, respectively can be found from roots of (A.20) and (A.33), respectively [37]. The CSIW is formed by using the substrate and SIW parameters given in Section 2.1. In Figure 3.1, the radius, $R = (\rho_1 + \rho_2)/2$ is taken as *10 cm* and the broad wall dimension, a is determined by the equivalent width of the CSIW, [4]. The height of the bended regular waveguide, $(\rho_2 - \rho_1)$, is equal to the thickness of the substrate used in CSIW. Using these parameters the eigenvalues, $\in_{mn}$ and μ_{mn} for TM^z_{mn} and TE^z_{mn} fields, respectively, are calculated at *25 GHz* and presented in Table 3.1. In Table 3.1, the *m*

Table 3.1: Eigenvalues, $\in_{mn}$ and μ_{mn}, of TE^{z}_{mn} and TM^{z}_{mn} modes for various *m* and *n* values. (NA: Not Applicable).

m	*n*	μ_{mn}	$\in_{mn}$	*m*	*n*	μ_{mn}	$\in_{mn}$
1	0	6.90	NA	0	1	NA	-j62.20
2	0	-j7.50	NA	1	1	-j62.45	-j62.45
3	0	-j15.12	NA	2	1	-j63.27	-j63.30
4	0	-j21.70	NA	3	1	-j64.60	-j64.60
5	0	-j28.00	NA	4	1	-j66.45	-j66.45
6	0	-j34.10	NA	5	1	-j68.75	-j68.75
7	0	-j40.10	NA	6	1	-j71.50	-j71.50
8	0	-j46.12	NA	7	1	-j74.60	-j74.60
9	0	-j52.10	NA	8	1	-j78.00	-j78.00
10	0	-j58.06	NA	9	1	-j81.60	-j81.60

values explicitly used in (A.20) and (A.33) are listed. However, different *n* values are assigned in order to discriminate two cases with same *m* value. The *n* values are started from *0*. As it is seen in Table 3.1, TE^{z}_{10} mode is the fundamental mode as in regular rectangular waveguides. The other bended regular waveguide modes are found to be similar to the *TE* and *TM* fields with respect to the direction of propagation in planar waveguides with the same transverse cross-section shown in Figure 3.1 except the case where $m = 0$ and $n = 1$. For $m = 0$ and $n = 1$, TE^{z}_{mn} field components vanishes which can be seen in Appendix A and TM^{z}_{mn} modes are excited unlike *TE* and *TM* modes in planar waveguides. For this reason, the value for the eigenvalue μ_{01} is assigned as not applicable (NA). The other cases where the eigenvalues assigned as NA in Table 3.1 corresponds to the cases such that there is no root of (A.20) or (A.33).

The propagation constant values in the E-plane bend regular waveguide can be found by dividing the eigenvalues listed in Table 3.1 by the radius, *R*. If this procedure is carried out for TE_{10}^{z} mode, it can be seen that the resulting propagation constant value is so close to the propagation constant values calculated in Figure 2.2 at *25 GHz* in Section 2.1.

3.1.2. Active Admittance Formulation of Longitudinal Slot on the CSIW

The active admittance formulations of the longitudinal slot on the CSIW are carried out using the procedure similar to one explained in [34]. The formulations are carried out for the longitudinal slots on E-plane bend regular waveguide and the equivalent width of SIW is used for the longitudinal slots on CSIW. Two formulas are derived for the active admittance values which are used as first and second design equations in the design of slotted CSIW array. In the first active admittance formula, it will be assumed that the total slot voltage is known after all couplings take place. Then the relation between the active admittance and circuit model parameters, such as, slot voltage, mode voltage, and characteristic impedance, etc., is found. The first design formula is used to find the relation between the active admittances of successive slots in the traveling wave array while the value of the active admittance is calculated explicitly in the second active admittance formula. In the second active admittance formula, the sources of the slot voltages are examined and the self-admittance is modified by mutual coupling terms. The accuracy of the active admittance value increases as the number of coupling terms considered in the second design equation increases. Before the active admittance formulations, the variables which define the bended regular waveguide and slot dimensions used in the active admittance formulations are introduced.

3.1.2.1. Waveguide and Slot Dimensions

The schematic view of longitudinal slot array on bended regular waveguide is shown in Figure 3.2. The bend regular waveguide is formed between cylindrical PEC surfaces located at $\rho = \rho_1$ and $\rho = \rho_2$. Then the longitudinal slots are cut on the surface at $\rho = \rho_2$. The waveguide has PEC boundaries on the waveguide walls located between $z = z_1$ and $z = z_2$ with $z_2 > z_1$ in $\hat{a}_z$-direction. Both the region defined by $\phi_L < \phi < \phi_F$ for $\rho < \rho_2$ and the other region defined by $\phi_F < \phi < \phi_L$ for $\rho < \rho_1$ are filled with PEC. Moreover, the structure extends to infinity in $\pm\hat{a}_z$-direction so that in the regions outside the waveguide, i.e., the region for $z < z_1$ and $z > z_2$, the structure becomes a cylindrical PEC volume with radius ρ_2. The waveguide region is covered by fictitious closed surface *S* which is composed of the surfaces S_F, S_L and S_3. The surface S_3 is located on the waveguide boundaries at

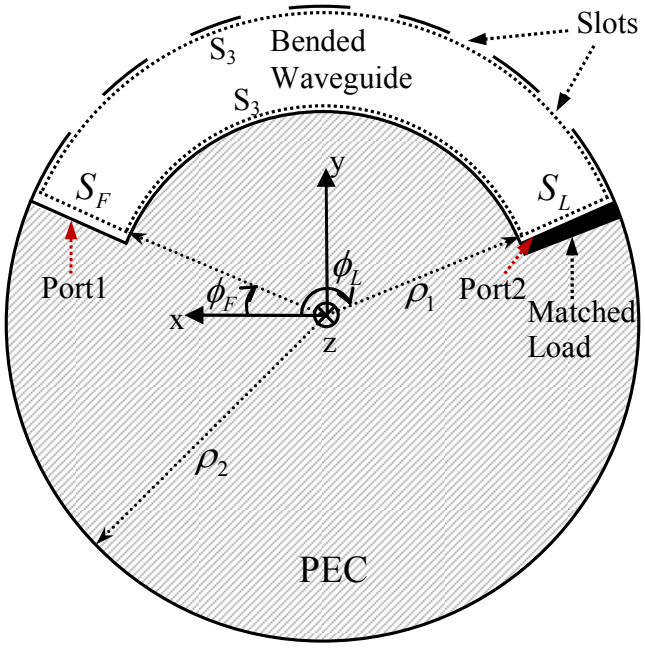

Figure 3.2: Longitudinal slot array on bended regular waveguide.

$\rho = \rho_1$, $\rho = \rho_2$, $z = z_1$, and $z = z_2$. The waveguide is fed from Port1 located at $\phi = \phi_F$ on the surface S_F and Port2 located at $\phi = \phi_L$ on the surface S_L is terminated by a matched load to obtain traveling wave slot array.

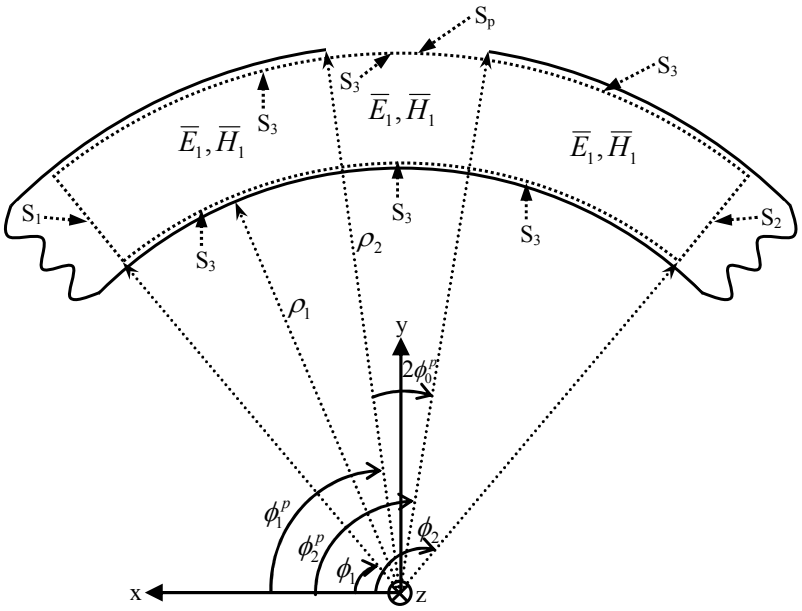

Figure 3.3: Longitudinal slot (p^{th} slot) on bended regular waveguide.

In order to describe the slot dimensions, the p^{th} slot in the slot array shown in Figure 3.2 is chosen. The p^{th} slot is presented in Figure 3.3. The start and end positions of the p^{th} slot in $\hat{a}_\phi$-direction are $\phi = \phi_1^p$ and $\phi = \phi_2^p$, respectively. The total angular displacement of the slot is $2\phi_0^p$ while the start and end positions of the slot in $\hat{a}_z$-direction are $z = z_1^p$ and $z = z_2^p$, respectively. The slot width, w^s is the same for all the slots in the slot array shown in Figure 3.2 and it is assumed to be very thin so that only $\hat{a}_z$-directed electric field exist in the slot. Considering these slot and waveguide dimensions following equations can be written.

$$2\phi_0^p = \phi_2^p - \phi_1^p \tag{3.1}$$

$$w^s = z_2^p - z_1^p \tag{3.2}$$

$$\phi^p = \frac{\phi_1^p + \phi_2^p}{2} \tag{3.3}$$

$$z^p = \frac{z_1^p + z_2^p}{2} \tag{3.4}$$

$$z^{p,0} = \frac{z_2 - z_1}{2} + z_p \tag{3.5}$$

where ϕ^p and z^p are the center positions of the slot in the global coordinate system. z_p is the slot offset measured with respect to the centerline of the waveguide as shown in Figure 1.2. $z^{p,0}$ is the center position of the slot in $\hat{a}_z$-direction measured from the wall of the waveguide. The derivation of the active admittance formulas are carried out using the field expressions given in Appendix A where the formulas are derived for waveguide located at $z_1 = 0$ and $z_2 = a$.

3.1.2.2. Derivation of the First Active Admittance Formula

The derivation of the active admittances is based on finding the backward scattered mode amplitude for each slot in the slot array shown in Figure 3.2 as explained in [33], [34], and [36]. Then using the relation between the backward scattered mode amplitude and the transmission line model, the first active admittance formula is derived. The backward scattered mode amplitude, B_p, for the p^{th} slot in the array can be found and the result can be generalized to all the slots in the array. First of all, the slotted bended regular waveguide array shown in Figure 3.2 is excited by the

fundamental mode, (TE_{10}^{z}) mode, incident from Port1 located at the surface S_F and Port2 at the surface S_L is terminated by a matched load. As a result of this excitation, the slot voltage $V_{p,1}^{s}$ appears between the terminals of the p^{th} slot in the waveguide. Because of the reflections of the fundamental mode and higher order modes from the other slots in the waveguide and also due to the external couplings, the total slot voltage becomes V_p^s for the p^{th} slot. The sources of V_p^s will be examined in detail in Section 3.1.2.3 while deriving the second active admittance formula. In deriving the first active admittance formula, it will be assumed that total slot voltage V_p^s is known in the array. The first active admittance formula gives the relation between the slot voltage, V_p^s and the active admittance. The slot voltage, V_p^s, and hence, the active admittance causes backward and forward scattering waves propagating in $-\hat{a}_\phi$ and $+\hat{a}_\phi$-directions respectively. The backward and forward scattered mode amplitudes for the p^{th} slot will be derived only for TE_{mn}^{z} modes because *9* higher order modes appear as TE_{mn}^{z} modes before TM_{mn}^{z} higher order modes are excited as shown in Table 3.1. The internal mutual couplings of the slots are considered only for the first higher order mode in the second design equation for planar waveguides, [36]. The effect of the higher order mode couplings increases as the height of the waveguide decreases, [36]. By considering the small thickness of the substrate, which determines the height of the bended regular waveguide with equivalent width of the CSIW used in this thesis, considering the effect of only the first higher order mode is enough and a few higher order modes can also be taken into account if desired. For this reason, the backward and forward scattered coefficients are not calculated for TM_{mn}^{z} modes in slotted bended regular waveguide array.

The backward and forward scattered mode amplitudes for TE_{mn}^{z} modes which are abbreviated as $B_p^{TE_{mn}^{z}}$ and $C_p^{TE_{mn}^{z}}$, respectively, caused by the slot voltage V_p^s will be derived by the help of the reciprocity theorem. Before applying the reciprocity

theorem, it is assumed in the derivations that the slot width, w^s is small enough so that only $\hat{a}_z$-directed electric field appears in the slot region. Moreover, it is also assumed that the scattering is not affected by the propagation direction of the field used to excite the waveguide, i.e., the slot mode is symmetrical and its shape is not affected by the direction of propagation of the waveguide mode [33]. Since the slot is longitudinally placed on the broad wall of the waveguide, the circuit model of the slot can be assumed as a shunt admittance as stated in Section 2.3.

The reciprocity theorem can be applied to the fields around the p^{th} slot in the slot array shown in Figure 3.2. The zoomed view of the p^{th} slot in the slot array while the array is excited is shown in Figure 3.3. The closed fictitious surface S is defined around the p^{th} slot to the apply the reciprocity theorem as shown in Figure 3.3. The surface, S is composed of three parts. The first and second parts are S_1 and S_2 lying before and after the p^{th} slot region, respectively. The third part, S_3 lies skin tight against the waveguide walls and it contains the surface S_p, defined just below the slot region. The fields $\overline{E}_1$ and $\overline{H}_1$ inside the surface S are TE^z_{mn} and TM^z_{mn} mode fields scattered by the slot to the region $\phi < \phi_1^p$ and $\phi > \phi_2^p$ and they are equal to the slot mode in the slot region. Similar to finding the scattering coefficients of the slots for TE modes in planar waveguides described in [33], the fields $\overline{E}_2$ and $\overline{H}_2$ inside the closed surface S are chosen as $TE^z_{m'n'}$ mode fields exist in the absence of the slot, i.e., when the slots in the waveguide is covered by conducting tape as shown in Figure 3.4. In Figure 3.4, the surface S_3 contains the fictitious surface, S_p to represent the p^{th} slot region. However, the slot surface S_p is shorted in Figure 3.4. Similar to [33], $\overline{E}_2$ and $\overline{H}_2$ are chosen as field components used to find the forward and backward scattering coefficients of the slot, they are not the modes exciting the waveguide. As stated before, the waveguide is excited by TE^z_{10} mode, and hence, the slot voltage V_p^s appears between the slot terminals. The usage of $\overline{E}_2$ and $\overline{H}_2$ is just an artifice to obtain scattering coefficients for $TE^z_{m'n'}$ mode, [33]. Since the closed surfaces defined

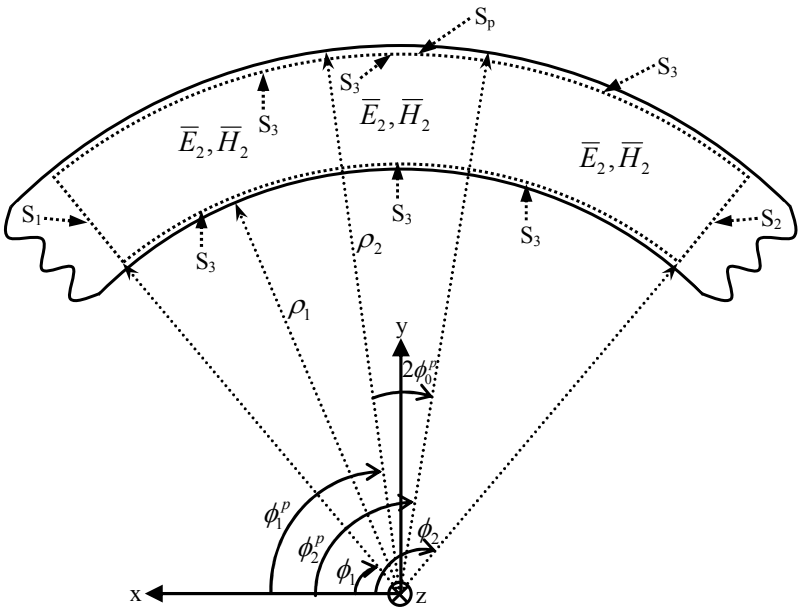

Figure 3.4: Bended regular waveguide with no slot (p^{th} slot is covered by conducting tape).

in Figure 3.3 and Figure 3.4 are geometrically the same, the reciprocity theorem presented in (3.6) can be applied between the fields $(\overline{E}_1, \overline{H}_1)$ and $(\overline{E}_2, \overline{H}_2)$ as, [33].

$$\int_S (\overline{E}_1 \times \overline{H}_2 - \overline{E}_2 \times \overline{H}_1).d\overline{S} = 0\,,\ S = S_1 \cup S_2 \cup S_3 \tag{3.6}$$

Since the tangential component of $\overline{E}_1$, $\overline{E}_1^{\tan g} = 0$ on the surface $S_3 - S_p$ in Figure 3.3 and the tangential component of $\overline{E}_2$, $\overline{E}_2^{\tan g} = 0$ over the surface S_3 in Figure 3.4, it is obtained that $\int_{S_3} (\overline{E}_1 \times \overline{H}_2 - \overline{E}_2 \times \overline{H}_1).d\overline{S} = \int_{S_p} (\overline{E}_{slot} \times \overline{H}_2).d\overline{S}$. Hence, (3.6) becomes

$$\int_{S_p} (\overline{E}_{slot} \times \overline{H}_2).d\overline{S} = \int_{S_1} (\overline{E}_2 \times \overline{H}_1 - \overline{E}_1 \times \overline{H}_2).d\overline{S} + \int_{S_2} (\overline{E}_2 \times \overline{H}_1 - \overline{E}_1 \times \overline{H}_2).d\overline{S} \tag{3.7}$$

where $\overline{E}_{slot}$ is the slot field found by considering the assumptions on the slots mentioned before and $\overline{E}_1 = \overline{E}_{slot}$ on S_p as shown in Figure 3.3.

The fields $\overline{E}_1$ and $\overline{H}_1$ on the surfaces S_1 and S_2 are composed of summation of TE^z_{mn} and summation of TM^z_{mn} modes derived in Appendix A and they are given by

$$\overline{E}_1 = \sum_{m=1}^{\infty}\sum_{n=0}^{\infty} \overline{E}_1^{TE^z_{mn}} + \sum_{m=0}^{\infty}\sum_{n=1}^{\infty} \overline{E}_1^{TM^z_{mn}} \ , \ \phi < \phi_1^p \ \text{ or } \ \phi > \phi_2^p \tag{3.8}$$

$$\overline{H}_1 = \sum_{m=1}^{\infty}\sum_{n=0}^{\infty} \overline{H}_1^{TE^z_{mn}} + \sum_{m=0}^{\infty}\sum_{n=1}^{\infty} \overline{H}_1^{TM^z_{mn}} \ , \ \phi < \phi_1^p \ \text{ or } \ \phi > \phi_2^p \tag{3.9}$$

The fields $\overline{E}_2$ and $\overline{H}_2$ are composed of only $TE^z_{m'n'}$ mode components, i.e., $\overline{E}_2 = \overline{E}_2^{TE^z_{m'n'}}$ and $\overline{H}_2 = \overline{H}_2^{TE^z_{m'n'}}$. Using mode orthogonality [39], the integrals over S_1 and S_2 on the right hand side (RHS) of (3.7) becomes

$$\int_{S_{1,2}} \left(\overline{E}_2 \times \overline{H}_1 - \overline{E}_1 \times \overline{H}_2\right) d\overline{S} = \int_{S_{1,2}} \left(\overline{E}_2^{TE^z_{m'n'}} \times \sum_{m=1}^{\infty}\sum_{n=0}^{\infty} \overline{H}_1^{TE^z_{mn}} - \sum_{m=1}^{\infty}\sum_{n=0}^{\infty} \overline{E}_1^{TE^z_{mn}} \times \overline{H}_2^{TE^z_{m'n'}} \right) . d\overline{S} \tag{3.10}$$

If $\overline{E}_2^{TE^z_{m'n'}}$ and $\overline{H}_2^{TE^z_{m'n'}}$ are chosen as $TE^z_{m'n'}$ mode fields propagating in $+\hat{a}_\phi$-direction, the backward scattered mode amplitudes, $B_p^{TE^z_{mn}}$ are derived. Since $d\overline{S}$ is in $\pm\hat{a}_\phi$-direction in (3.10), only transverse field components ($\hat{a}_\rho$ and $\hat{a}_z$-components) of $\overline{E}_1^{TE^z_{mn}}, \overline{H}_1^{TE^z_{mn}}$ and $\overline{E}_2^{TE^z_{m'n'}}, \overline{H}_2^{TE^z_{m'n'}}$ are required for the integrals taken over S_1 and S_2. The transverse field components of $\overline{E}_1^{TE^z_{mn}}, \overline{H}_1^{TE^z_{mn}}$ in the regions of S_1 and S_2 can be written using the fields derived in Appendix A as

$$\overline{E}_{1,t}^{TE_{mn}^{z}} = \begin{cases} -\dfrac{j}{\rho}\displaystyle\sum_{m=1}^{\infty}\sum_{n=0}^{\infty} B_{p}^{TE_{mn}^{z}} \sin\left(\frac{m\pi z}{a}\right) B_{\mu_{mn}}\left(k_{\rho}^{TE_{mn}^{z}}\rho\right)\mu_{mn} e^{+j\mu_{mn}\left(\phi-\phi^{p}\right)}\hat{a}_{\rho} & \phi < \phi_{1}^{p} \\ \dfrac{j}{\rho}\displaystyle\sum_{m=1}^{\infty}\sum_{n=0}^{\infty} C_{p}^{TE_{mn}^{z}} \sin\left(\frac{m\pi z}{a}\right) B_{\mu_{mn}}\left(k_{\rho}^{TE_{mn}^{z}}\rho\right)\mu_{mn} e^{-j\mu_{mn}\left(\phi-\phi^{p}\right)}\hat{a}_{\rho} & \phi > \phi_{2}^{p} \end{cases} \tag{3.11}$$

$$\overline{H}_{1,t}^{TE_{mn}^{z}} = \begin{cases} \left[\begin{array}{l} \dfrac{1}{\hat{z}}\displaystyle\sum_{m=1}^{\infty}\sum_{n=0}^{\infty} B_{p}^{TE_{mn}^{z}} \frac{m\pi}{a}\cos\left(\frac{m\pi z}{a}\right) B'_{\mu_{mn}}\left(k_{\rho}^{TE_{mn}^{z}}\rho\right) k_{\rho}^{TE_{mn}^{z}} e^{+j\mu_{mn}\left(\phi-\phi^{p}\right)}\hat{a}_{\rho} \\ +\displaystyle\sum_{m=1}^{\infty}\sum_{n=0}^{\infty} B_{p}^{TE_{mn}^{z}} \frac{\left(k_{\rho}^{TE_{mn}^{z}}\right)^{2}}{\hat{z}} \sin\left(\frac{m\pi z}{a}\right) B_{\mu_{mn}}\left(k_{\rho}^{TE_{mn}^{z}}\rho\right) e^{+j\mu_{mn}\left(\phi-\phi^{p}\right)}\hat{a}_{z} \end{array}\right] & \phi < \phi_{1}^{p} \\ \left[\begin{array}{l} \dfrac{1}{\hat{z}}\displaystyle\sum_{m=1}^{\infty}\sum_{n=0}^{\infty} C_{p}^{TE_{mn}^{z}} \frac{m\pi}{a}\cos\left(\frac{m\pi z}{a}\right) B'_{\mu_{mn}}\left(k_{\rho}^{TE_{mn}^{z}}\rho\right) k_{\rho}^{TE_{mn}^{z}} e^{-j\mu_{mn}\left(\phi-\phi^{p}\right)}\hat{a}_{\rho} \\ +\displaystyle\sum_{m=1}^{\infty}\sum_{n=0}^{\infty} C_{p}^{TE_{mn}^{z}} \frac{\left(k_{\rho}^{TE_{mn}^{z}}\right)^{2}}{\hat{z}} \sin\left(\frac{m\pi z}{a}\right) B_{\mu_{mn}}\left(k_{\rho}^{TE_{mn}^{z}}\rho\right) e^{-j\mu_{mn}\left(\phi-\phi^{p}\right)}\hat{a}_{z} \end{array}\right] & \phi > \phi_{2}^{p} \end{cases} \tag{3.12}$$

Let $\overline{E}_{2}^{TE_{m'n'}^{z}}$ and $\overline{H}_{2}^{TE_{m'n'}^{z}}$ be $TE_{m'n'}^{z}$ mode field propagating in $+\hat{a}_{\phi}$-direction. The transverse field components of $\overline{E}_{2}^{TE_{m'n'}^{z}}$ and $\overline{H}_{2}^{TE_{m'n'}^{z}}$ are given by

$$\overline{E}_{2,t}^{TE_{m'n'}^{z}} = \frac{j}{\rho}\sin\left(\frac{m'\pi z}{a}\right) B_{\mu_{m'n'}}\left(k_{\rho}^{TE_{m'n'}^{z}}\rho\right)\mu_{m'n'} e^{-j\mu_{m'n'}\left(\phi-\phi^{p}\right)}\hat{a}_{\rho} \tag{3.13}$$

$$\overline{H}_{2,t}^{TE_{m'n'}^{z}} = \left[\begin{array}{l} \dfrac{1}{\hat{z}}\dfrac{m'\pi}{a}\cos\left(\frac{m'\pi z}{a}\right) B'_{\mu_{m'n'}}\left(k_{\rho}^{TE_{m'n'}^{z}}\rho\right) k_{\rho}^{TE_{m'n'}^{z}} e^{-j\mu_{m'n'}\left(\phi-\phi^{p}\right)}\hat{a}_{\rho} + \\ \dfrac{\left(k_{\rho}^{TE_{m'n'}^{z}}\right)^{2}}{\hat{z}}\sin\left(\frac{m'\pi z}{a}\right) B_{\mu_{m'n'}}\left(k_{\rho}^{TE_{m'n'}^{z}}\rho\right) e^{-j\mu_{m'n'}\left(\phi-\phi^{p}\right)}\hat{a}_{z} \end{array}\right] \tag{3.14}$$

It can be shown that $\int_{S_2}\left(\overline{E}_{2}^{TE_{m'n'}^{z}} \times \sum_{m=1}^{\infty}\sum_{n=0}^{\infty}\overline{H}_{1}^{TE_{mn}^{z}} - \sum_{m=1}^{\infty}\sum_{n=0}^{\infty}\overline{E}_{1}^{TE_{mn}^{z}} \times \overline{H}_{2}^{TE_{m'n'}^{z}}\right).d\overline{S} = 0$ in (3.10). Then using (3.7) - (3.14) and mode orthogonality the back scattering mode amplitudes are derived as

$$B_p^{TE_{mn}^z} = \frac{\int_{S_{slot}} \left(\overline{E}_{slot} \times \overline{H}_2^{TE_{mn}^z}\right) d\overline{S}}{2\int_{S_1} \left(\overline{E}_t^{TE_{mn}^z} \times \overline{H}_t^{TE_{mn}^z}\right) d\overline{S}} \tag{3.15}$$

where

$$\overline{E}_t^{TE_{mn}^z} = \frac{j}{\rho} \sin\left(\frac{m\pi z}{a}\right) B_{\mu_{mn}}\left(k_\rho^{TE_{mn}^z} \rho\right) \mu_{mn} \hat{a}_\rho \tag{3.16}$$

$$\overline{H}_t^{TE_{mn}^z} \frac{1}{\hat{z}} \frac{m\pi}{a} \cos\left(\frac{m\pi z}{a}\right) B'_{\mu_{mn}}\left(k_\rho^{TE_{mn}^z} \rho\right) k_\rho \hat{a}_\rho + \frac{\left(k_\rho^{TE_{mn}^z}\right)^2}{\hat{z}} \sin\left(\frac{m\pi z}{a}\right) B_{\mu_{mn}}\left(k_\rho^{TE_{mn}^z} \rho\right) \hat{a}_z \tag{3.17}$$

$$\overline{H}_2^{TE_{mn}^z} = \begin{bmatrix} \frac{1}{\hat{z}} \frac{m\pi}{a} \cos\left(\frac{m\pi z}{a}\right) B'_{\mu_{mn}}\left(k_\rho^{TE_{mn}^z} \rho\right) k_\rho^{TE_{mn}^z} e^{-j\mu_{mn}\left(\phi - \phi^p\right)} \hat{a}_\rho + \\ \frac{\left(k_\rho^{TE_{mn}^z}\right)^2}{\hat{z}} \sin\left(\frac{m\pi z}{a}\right) B_{\mu_{mn}}\left(k_\rho^{TE_{mn}^z} \rho\right) e^{-j\mu_{mn}\left(\phi - \phi^p\right)} \hat{a}_z - \\ \frac{j}{\hat{z}\rho} \frac{m\pi}{a} \cos\left(\frac{m\pi z}{a}\right) B_{\mu_{mn}}\left(k_\rho^{TE_{mn}^z} \rho\right) \mu_{mn} e^{-j\mu_{mn}\left(\phi - \phi^p\right)} \hat{a}_\phi \end{bmatrix} \tag{3.18}$$

and where the slot field is given by

$$\overline{E}_{slot} = \frac{V_p^s}{w^s} \cos\left(\frac{\pi\left(\phi - \phi^p\right)}{2\phi_0^p}\right) \hat{a}_z \tag{3.19}$$

By assuming $\overline{E}_2^{TE_{m'n'}^z}$ and $\overline{H}_2^{TE_{m'n'}^z}$ mode fields propagating in $-\hat{a}_\phi$-direction, the forward scattering TE_{mn}^z mode amplitudes $C_p^{TE_{mn}^z}$ can be found and it can be shown that

$$C_p^{TE_{mn}^z} = -B_p^{TE_{mn}^z} \tag{3.20}$$

The general expression of $B_p^{TE_{mn}^z}$ can be obtained from (3.15) as

$$B_p^{TE_{mn}^z} = K^{TE_{mn}^z} f_p^{TE_{mn}^z} V_p^s \tag{3.21}$$

where

$$K^{TE_{mn}^z} = \frac{m\pi}{a^2\left(k_\rho^{TE_{mn}^z}\right)^2} \frac{B_{\mu_{m0}}\left(k_\rho^{TE_{mn}^z}\rho_2\right)}{N_{\mu_{mn}}} \sin c\left(\frac{mw^s}{2a}\right) \tag{3.22}$$

$$f_p^{TE_{mn}^z} = \frac{\left(\pi/\phi_0^p\right)\cos\left(\mu_{mn}\phi_0^p\right)}{\left(\pi/2\phi_0^p\right)^2 - \mu_{mn}^2} \cos\left(\frac{m\pi z^{p,0}}{a}\right) \tag{3.23}$$

and where

$$N_{\mu_{mn}} = \int_{\rho_1}^{\rho_2} \frac{1}{\rho}\left[B_{\mu_{mn}}\left(k_\rho^{TE_{mn}^z}\rho\right)\right]^2 d\rho \tag{3.24}$$

In (3.22), since $w^s << 2a$, the term $\sin c\left(\frac{mw^s}{2a}\right) \approx 1$ for $m = 1$.

In order to relate the active admittance to the slot voltage, the circuit model presented in Figure 3.5 can be used. In Figure 3.5, the active admittance of the p^{th} slot is

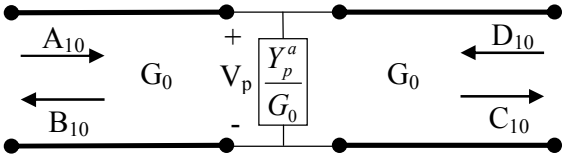

Figure 3.5: Circuit model of the longitudinal slot on E-plane bend regular waveguide.

assumed to be placed between transmission lines. The transmission lines with characteristic impedance, G_0, represent the E-plane bend regular waveguide before and after the slot. The incident and scattered fields are assumed to be TE_{10}^{z} waveguide modes. A_{10} is due to the excitation of the waveguide plus the reflections coming from the slots located before the p^{th} slot and D_{10} is due to the reflections coming from the succeeding slots. B_{10} and C_{10} are the back and forward scattered voltage coefficients. The multi-reflection effects due to D_{10} are not taken into account. The mode voltage, V_p can be defined between the upper and lower walls of the waveguide. Hence, by considering the sign change in the $\hat{a}_\rho$-component of the electrical field in TE_{10}^{z} mode with respect to the direction of propagation in Appendix A, the following equations can be derived [33],

$$\frac{Y_p^a}{G_0} = \frac{2B_{10}}{A_{10} - D_{10} - B_{10}} \tag{3.25}$$

$$B_{10} = -C_{10} = \frac{1}{2}\frac{Y_p^a}{G_0}V_p \tag{3.26}$$

Hence, the back scattered mode amplitudes can be equated as

$$B_p^{TE_{10}^z} = B_{10} = \frac{1}{2}\frac{Y_p^a}{G_0}V_p \tag{3.27}$$

In order (3.27) to be valid the backward scattered power levels must be the same. The backward scattered power levels can be equated as follows.

$$\frac{1}{2}\left|B_{10}\right|^2 G_0 = \frac{1}{2}\mathrm{Re}\left\{\int_{S_1}\left(B_p^{TE_{mn}^z}\overline{E}_t^{TE_{mn}^z} \times \left(B_p^{TE_{mn}^z}\overline{H}_t^{TE_{mn}^z}\right)^*\right).d\overline{S}\right\} \tag{3.28}$$

The first active admittance formula due to TE_{10}^{z} mode scattering can be derived using (3.21), (3.27), and (3.28) as

$$\frac{Y_p^a}{G_0} = K_1 f_p^{TE_{10}^z} \frac{V_p^s}{V_p} \tag{3.29}$$

where

$$K_1 = \frac{j\pi}{a} B_{\mu_{10}}\left(k_\rho^{TE_{10}^z}\rho_2\right)\sqrt{\frac{2\mu_{10}}{\omega\mu G_0 a N_{\mu_{10}}\left(k_\rho^{TE_{10}^z}\right)^2}} \tag{3.30}$$

$$f_p^{TE_{10}^z} = -\frac{\left(\pi/\phi_0^p\right)\cos\left(\mu_{10}\phi_0^p\right)}{\left(\pi/2\phi_0^p\right)^2 - \mu_{10}^2}\sin\left(\frac{\pi z_p}{a}\right) \tag{3.31}$$

3.1.2.3. Derivation of the Second Active Admittance Formula

The second active admittance formula contains the self-slot admittance and the related mutual coupling terms used to modify the self-slot admittance. In order to obtain the second design equation, the sources of the slot voltage, V_p^s are examined for the p^{th} slot in the waveguide. The slot voltage can be considered as composed of four parts as follows

$$V_p^s = V_{p,1}^s + V_{p,2}^s + V_{p,3}^s + V_{p,4}^s \tag{3.32}$$

where $V_{p,1}^s$ is the slot voltage due to the TE_{10}^z mode excitation of the waveguide and $V_{p,2}^s$ is the slot voltage excited by the TE_{10}^z mode reflected from the succeeding slots.

$V_{p,3}^{s}$ is the slot voltage caused by the external couplings of the slot with the other slots while $V_{p,4}^{s}$ is due to the internal higher order mode couplings in the waveguide.

First of all, the p^{th} slot is assumed to be the only slot in the E-plane bend regular waveguide. Hence, the active admittance in Figure 3.5 becomes a self-slot admittance, Y_p^s/G_0 which corresponds to the slot voltage, $V_{p,1}^{s}$. This case corresponds to a transmission line model with a shunt self-admittance which is excited by the incident voltage with amplitude A_{10} and scattering coefficients B_{10} and C_{10} appear as a result of this excitation. Since there are no other slots in the waveguide $D_{10} = 0$. Hence using (3.25), the self-admittance is given by

$$\frac{Y_p^s}{G_0} = \frac{2\left(B_{10}/A_{10}\right)}{1-\left(B_{10}/A_{10}\right)} \tag{3.33}$$

The term $\left(B_p^{TE_{10}^z}/A_p^{TE_{10}^z}\right)$ is equivalent to $\left(B_{10}/A_{10}\right)$ and if it is used in (3.33), following equation is obtained.

$$B_p^{TE_{10}^z} = \frac{\dfrac{Y_p^s}{G_0}}{2+\dfrac{Y_p^s}{G_0}} A_p^{TE_{10}^z} \tag{3.34}$$

Using (3.21) for the relation between $B_p^{TE_{10}^z}$ and $V_{p,1}^{s}$ for the single slot case, it is obtained that

$$V_{p,1}^{s} = \frac{1}{f_p^{TE_{10}^z} K^{TE_{10}^z}} \frac{\dfrac{Y_p^s}{G_0}}{2+\dfrac{Y_p^s}{G_0}} A_p^{TE_{10}^z} \tag{3.35}$$

If the other slots exist in the waveguide, there is TE_{10}^{z} mode incident from $-\hat{a}_{\phi}$-direction with mode amplitude, $D_p^{TE_{10}^{z}}$ which causes the slot voltage, $V_{p,2}^{s}$. The relation between $D_p^{TE_{10}^{z}}$ and $V_{p,2}^{s}$ is given by

$$V_{p,2}^{s} = -\frac{1}{f_p^{TE_{10}^{z}} K^{TE_{10}^{z}}} \frac{\frac{Y_p^s}{G_0}}{2+\frac{Y_p^s}{G_0}} D_p^{TE_{10}^{z}} \tag{3.36}$$

If all the calculations are carried out till (3.21) to find the back scattering coefficient for $D_p^{TE_{10}^{z}}$ excitation, it will be clear that the back scattering coefficient for $D_p^{TE_{10}^{z}}$ excitation is similar to finding the forward scattering coefficient, $C_p^{TE_{10}^{z}}$, for $A_p^{TE_{10}^{z}}$ excitation. Since $C_p^{TE_{10}^{z}} = -B_p^{TE_{10}^{z}}$, there is a sign difference between (3.35) and (3.36).

Up to now, the slot voltage terms due to TE_{10}^{z} mode in the waveguide are found. The slot voltages $V_{p,3}^{s}$ and $V_{p,4}^{s}$ due to external and internal couplings, respectively, will be derived using reciprocity theorem. In the derivations, the similar procedure presented in [34] and [36] will be used. First of all, only the p^{th} and q^{th} slots are assumed to be present in the slot array as shown in Figure 3.6. In Figure 3.6, the bended regular waveguide is excited by TE_{10}^{z} mode with amplitude $A^{TE_{10}^{z}}$ from Port1. Port2 is terminated by a matched load in order to obtain traveling wave array. As a result of this excitation, the voltages V_p^s and V_q^s appears between the terminals of the p^{th} and q^{th} slots, respectively. V_p^s and V_q^s are the voltages which takes all the internal and external couplings into account. If the backward scattered mode amplitude in the p^{th} slot due to the slot voltage V_q^s is found then it can be related to the slot voltages $V_{p,3}^{s}$ and $V_{p,4}^{s}$ using (3.21).

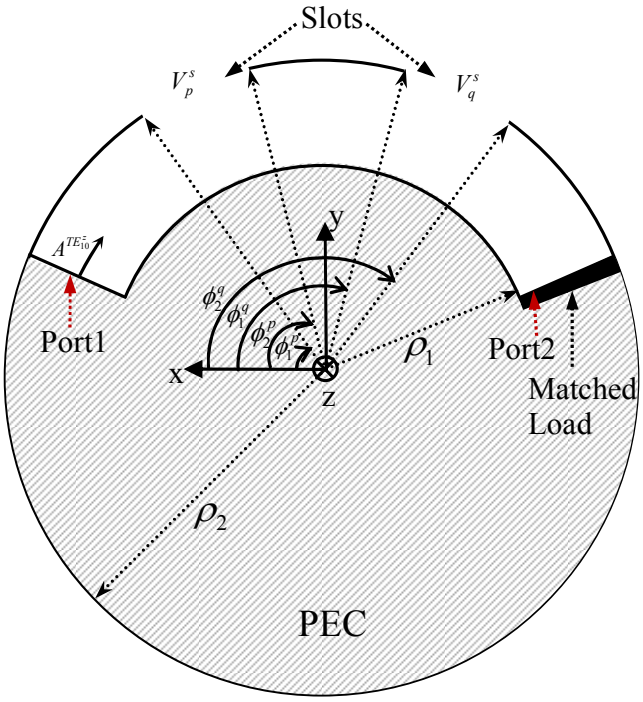

Figure 3.6: Longitudinal slot array composed of p^{th} and q^{th} slots on bended regular waveguide.

Two different cases, namely, case "a" and case "b" are defined to apply the reciprocity theorem. In case "a", the E-plane bend regular waveguide is excited from Port1 when only the p^{th} slot exist in the array while in case "b", q^{th} slot is assumed to exist in addition to p^{th} slot in the waveguide where only the q^{th} slot is excited which causes the slot voltages $V_{p,3}^s$ and $V_{p,4}^s$ in the p^{th} slot. The reciprocity theorem applied between two cases is given by, [33]

$$\int_V \left(\overline{E}^b . \overline{J}^a - \overline{H}^b . \overline{M}^a\right) dV = \int_V \left(\overline{E}^a . \overline{J}^b - \overline{H}^a . \overline{M}^b\right) dV \tag{3.37}$$

where the superscripts "a" and "b" are used to describe case "a" and case "b", respectively. $\overline{J}^a$ and $\overline{M}^a$ are the equivalent electric and magnetic currents,

respectively, which are the sources of the fields $\overline{E}^a$ and $\overline{H}^a$ in volume V in case "a". Similarly, $\overline{J}^b$ and $\overline{M}^b$ are the equivalent electric and magnetic currents, respectively, which are the sources of the fields $\overline{E}^b$ and $\overline{H}^b$ in volume V in case "b". The volume V is the same for "a" and "b" cases. The detailed description of volume V, case "a" and case "b" will be given in the following steps of the derivation.

The sources in "a" and "b" cases are the incident field at Port1 and the slot voltage, V_q^s, respectively, as shown in Figure 3.6. In order to obtain reaction of the incident field at Port1 on the q^{th} slot, the slot voltage V_q^s should be killed in case "a". This is accomplished by covering the q^{th} slot by a conducting tape such that $V_q^s = 0$ as shown in Figure 3.7 (a). In Figure 3.7 (a), case "a" is described such that TE_{10}^z mode with amplitude A^a is incident from Port1 while Port2 is terminated by a matched

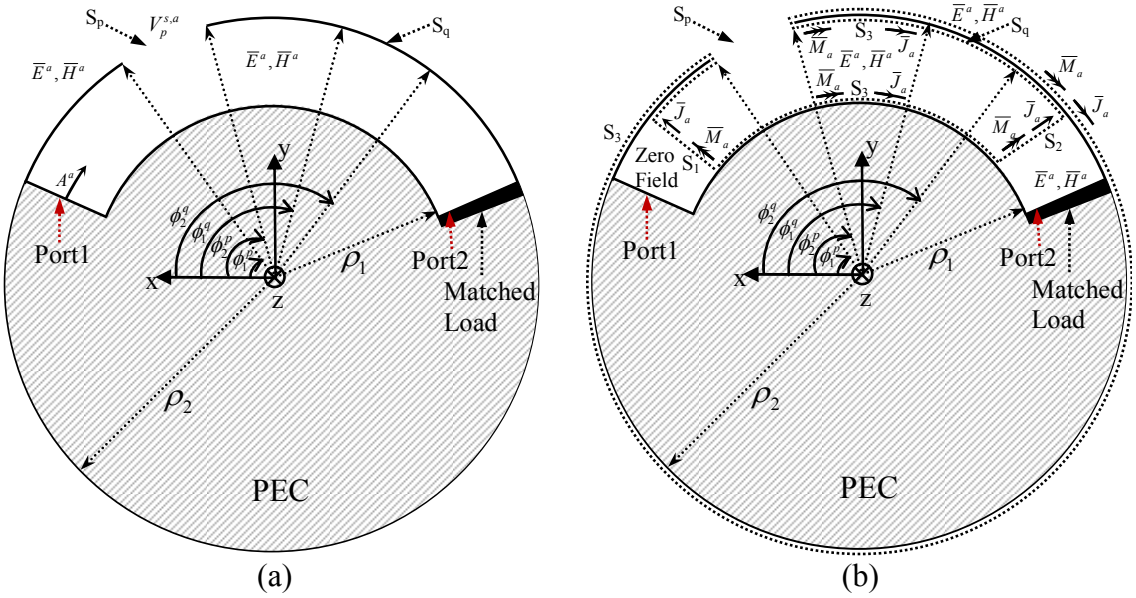

Figure 3.7: (a) Longitudinal slot array with q^{th} slot is covered by conducting tape (case "a"). (b) Equivalent problem.

load and q^{th} slot is shorted. As a result of this excitation, the voltage $V_p^{s,a}$ is excited at the center of the slot and TE_{10}^z modes with amplitude B^a and C^a are scattered in $-\hat{a}_\phi$ and $\hat{a}_\phi$-directions, respectively.

The equivalent problem of case "a" is shown in Figure 3.7 (b) where the equivalent currents on the fictitious surface S are defined using equivalence principle. The volume V in case "a" is defined by the fictitious surface S as shown in Figure 3.7 (b). The surface S is composed of three parts which are S_1, S_2, and S_3. S_1 and S_2 are the surfaces used to describe the cross-section of the bended regular waveguide in front of Port1 and Port2, respectively. The surface S_3 is located at $\rho = \rho_1$ and $\rho = \rho_2$. The surface S_3 extends outside the waveguide and covers the full circumference of the cylinder except the p^{th} slot surface S_p. S_3 contains the q^{th} slot surface S_q at both inside and outside the waveguide. Moreover, S_3 is also defined on the waveguide walls at $z = z_1$ and $z = z_2$ inside the waveguide and the surface S_3 extends to infinity in $\pm\hat{a}_z$-directions outside the waveguide. The fields $\overline{E}^a$ and $\overline{H}^a$ in case "a" shown in Figure 3.7 (a) are supported by the equivalent currents $\overline{J}^a$ and $\overline{M}^a$ on surface S in the equivalent problem shown in Figure 3.7 (b). Using the field expressions derived in Appendix A, the equivalent currents $\overline{J}^a$ and $\overline{M}^a$ on S_1 and S_2 are given by

$$\overline{J}^a = \begin{cases} \left[\begin{array}{l} -\dfrac{1}{\hat{z}}\dfrac{\pi}{a}\cos\left(\dfrac{\pi z}{a}\right) B'_{\mu_{10}}\left(k_\rho^{TE_{10}^z}\rho\right) k_\rho^{TE_{10}^z}\hat{a}_z \\ +\dfrac{\left(k_\rho^{TE_{10}^z}\right)^2}{\hat{z}}\sin\left(\dfrac{\pi z}{a}\right) B_{\mu_{10}}\left(k_\rho^{TE_{10}^z}\rho\right)\hat{a}_\rho \end{array} \right] \left(\begin{array}{l} A^a e^{-j\mu_{10}(\phi-\phi^p)} + \\ B^a e^{j\mu_{10}(\phi-\phi^p)} \end{array} \right) & (\phi,\rho,z) \in S_1 \\ 0 & (\phi,\rho,z) \in S_2 \end{cases} \tag{3.38}$$

$$\overline{M}^a = \begin{cases} \dfrac{j}{\rho}\sin\left(\dfrac{\pi z}{a}\right) B_{\mu_{10}}\left(k_\rho^{TE_{10}^z}\rho\right)\mu_{10}\hat{a}_z \left(\begin{array}{l} A^a e^{-j\mu_{10}(\phi-\phi^p)} - \\ B^a e^{j\mu_{10}(\phi-\phi^p)} \end{array} \right) & (\phi,\rho,z) \in S_1 \\ 0 & (\phi,\rho,z) \in S_2 \end{cases} \tag{3.39}$$

Since the fields are set to zero between Port1 and the surface S_1, both $\overline{J}^a$ and $\overline{M}^a$ are found on S_1. In [34], the surface S_2 is let to go to infinity in planar waveguides and no obstacles are assumed which causes reflections. Hence, no sources are assumed from the matched side of the waveguide. In Figure 3.7 (b), matched load is used at Port2 which avoids the reflections, and hence, there are no sources incident from $-\hat{a}_\phi$-direction. Since the fields between the surface S_2 and Port2 exist both in Figure 3.7 (a) and (b) due to the matched load at Port2, the equivalent currents $\overline{J}^a$ and $\overline{M}^a$ on S_2 are found as zero. Regarding the equivalent currents on S_3, it can be stated that only equivalent electric currents ($\overline{J}^a$) exist on S_3 because the tangential electric field in case "a", $\overline{E}^a_{\tan g} = 0$ on S_3. It will be understood that $\overline{J}^a$ on S_3 need not to be determined in applying the reciprocity theorem. Moreover, only the field $\overline{H}^a$ is required to be determined on the surface S_q.

In case "b", Port1 in the slot array shown in Figure 3.6 is not excited and it is terminated by a matched load. Case "b" is described as in Figure 3.8 (a). In Figure 3.8 (a), the q^{th} slot is excited by slot voltage, $V_q^{s,b}$ while Port1 and Port2 are terminated by a matched load. As a result of this excitation, TE_{10}^z modes with amplitude B_{all}^b and C_{all}^b are scattered in $-\hat{a}_\phi$ and $\hat{a}_\phi$-directions, respectively.

The equivalent problem for case "b" is shown in Figure 3.8 (b). The surface S shown in Figure 3.8 (b) is exactly the same as the surface presented in Figure 3.7 (b). Hence, the volumes V in case "a" and "b" defined by the surface S are the same and the reciprocity theorem given in (3.37) can be applied between "a" and "b" cases. In the equivalent problem of case "b"shown in Figure 3.8 (b), since the fields $\overline{E}^b$ and $\overline{H}^b$ exist between Port1 and surface S_1 and also between Port2 and surface S_2, $\overline{J}^b = \overline{M}^b = 0$ on S_1 and S_2. Moreover, only the equivalent electric currents ($\overline{J}^b$) exist on the surface S_3 because the tangential electric field in case "b", $\overline{E}^b_{\tan g} = 0$ on S_3. Equivalent magnetic sources are placed external and internal to the waveguide on

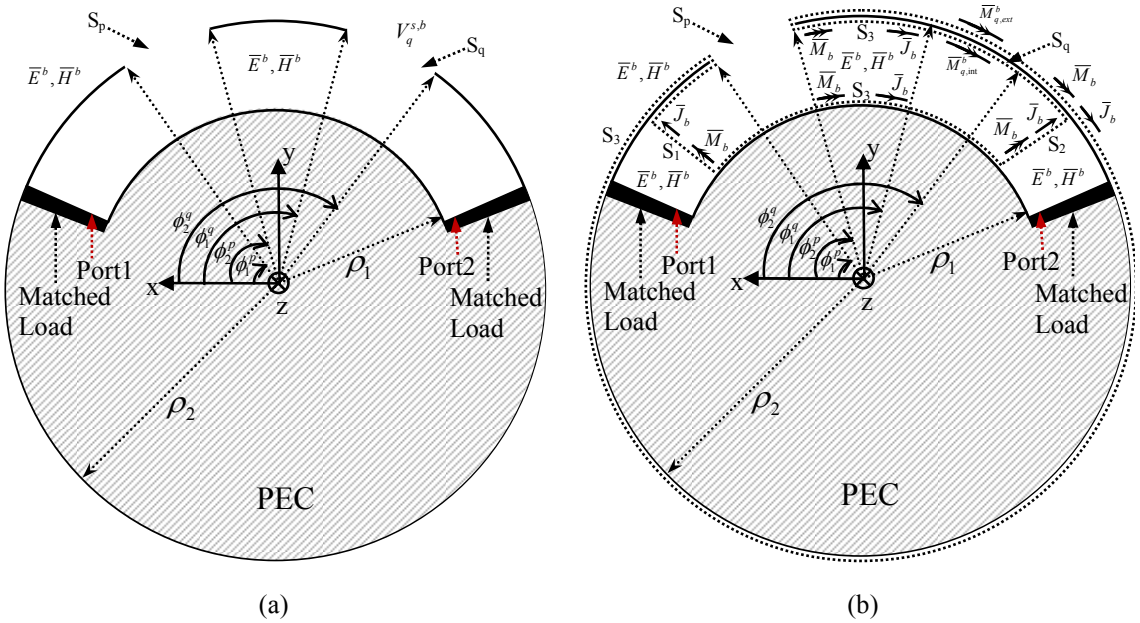

Figure 3.8: (a) Longitudinal slot array composed of p^{th} and q^{th} slots on bended regular waveguide with q^{th} slot is excited (case "b"). (b) Equivalent problem.

the surface of the q^{th} slot, S_q, and the q^{th} slot is covered by PEC. The equivalent magnetic currents located exterior and interior of the bended regular waveguide are indicated as $\overline{M}^b_{q,ext}$ and $\overline{M}^b_{q,\text{int}}$, respectively, in Figure 3.8 (b).

The field components of $\overline{E}^b$ and $\overline{H}^b$ are assumed to be single mode which is TE^z_{10} mode in the bended regular waveguide. The values of $\overline{E}^b$ and $\overline{H}^b$ on S_2 and S_3 are not needed in applying the reciprocity theorem, and hence, $\overline{E}^b$ and $\overline{H}^b$ fields on S_1 are given by

$$E^b_\rho = -\frac{j}{\rho}\sin\left(\frac{\pi z}{a}\right)B_{\mu_{10}}\left(k_\rho^{TE^z_{10}}\rho\right)\mu_{10}B^b_{all}e^{j\mu_{10}\left(\phi-\phi^p\right)},\ (\phi,\rho,z)\in S_1 \qquad (3.40)$$

$$E_{\phi}^{b} = \sin\left(\frac{\pi z}{a}\right) B'_{\mu_{10}}\left(k_{\rho}^{TE_{10}^{z}}\rho\right) k_{\rho}^{TE_{10}^{z}} B_{all}^{b} e^{j\mu_{10}\left(\phi-\phi^{p}\right)},\ (\phi,\rho,z)\in S_1 \tag{3.41}$$

$$E_{z}^{b} = 0\ ,\ (\phi,\rho,z)\in S_1 \tag{3.42}$$

$$H_{\rho}^{b} = \frac{1}{\hat{z}}\frac{\pi}{a}\cos\left(\frac{\pi z}{a}\right) B'_{\mu_{10}}\left(k_{\rho}^{TE_{10}^{z}}\rho\right) k_{\rho}^{TE_{10}^{z}} B_{all}^{b} e^{j\mu_{10}\left(\phi-\phi^{p}\right)},\ (\phi,\rho,z)\in S_1 \tag{3.43}$$

$$H_{\phi}^{b} = \frac{j}{\hat{z}\rho}\frac{\pi}{a}\cos\left(\frac{\pi z}{a}\right) B_{\mu_{10}}\left(k_{\rho}^{TE_{10}^{z}}\rho\right) \mu_{10} B_{all}^{b} e^{j\mu_{10}\left(\phi-\phi^{p}\right)},\ (\phi,\rho,z)\in S_1 \tag{3.44}$$

$$H_{z}^{b} = \frac{\left(k_{\rho}^{TE_{10}^{z}}\right)^{2}}{\hat{z}}\sin\left(\frac{\pi z}{a}\right) B_{\mu_{10}}\left(k_{\rho}^{TE_{10}^{z}}\rho\right) B_{all}^{b} e^{j\mu_{10}\left(\phi-\phi^{p}\right)},\ (\phi,\rho,z)\in S_1 \tag{3.45}$$

The reciprocity theorem given in (3.37) is applied between case "a" and case "b". If it is considered that all the equivalent currents are defined on the surface *S*, only the tangential field components on the surface *S* are required to be determined. Moreover, (3.37) reduces to the surface integral in the regions where the current sources are located. Hence, (3.37) becomes

$$\int_{S}\left(\overline{E}^{b}.\overline{J}^{a} - \overline{H}^{b}.\overline{M}^{a}\right)dS = \int_{S}\left(\overline{E}^{a}.\overline{J}^{b} - \overline{H}^{a}.\overline{M}^{b}\right)dS\ ,\ S = S_1 \cup S_2 \cup S_3 \tag{3.46}$$

Since $\overline{J}^{a} = \overline{M}^{a} = 0$ on S_2, $\overline{M}^{a} = 0$ on S_3, and $\overline{E}_{\tan g}^{b} = 0$ on S_3, the left hand side (LHS) of (3.46) becomes

$$\int_{S}\left(\overline{E}^{b}.\overline{J}^{a} - \overline{H}^{b}.\overline{M}^{a}\right)dS = \int_{S_1}\left(\overline{E}^{b}.\overline{J}^{a} - \overline{H}^{b}.\overline{M}^{a}\right)dS_1 \tag{3.47}$$

In (3.46), $\int_S \left(\overline{E}^a . \overline{J}^b\right) dS = 0$ because $\overline{E}^a_{\tan g} = 0$ on S_3 and $\overline{J}^b = 0$ on S_1 and S_2. Moreover, $\int_S \left(\overline{H}^a . \overline{M}^b\right) dS = \int_{S_q} \left(\overline{H}^a_{ext} . \overline{M}^b_{q,ext} + \overline{H}^a_{\text{int}} . \overline{M}^b_{q,\text{int}}\right) dS_q$ because $\overline{M}^b_{q,ext} = \overline{M}^b_{q,\text{int}} = 0$ on S_1, S_2, and S_3-S_q where $\overline{H}^a_{\text{int}}$ and $\overline{H}^a_{ext}$ are the magnetic fields inside and outside the bended regular waveguide in case "a". Hence, RHS of (3.46) becomes

$$\int_S \left(\overline{E}^a . \overline{J}^b - \overline{H}^a . \overline{M}^b\right) dS = -\int_{S_q} \left(\overline{H}^a_{ext} . \overline{M}^b_{q,ext} + \overline{H}^a_{\text{int}} . \overline{M}^b_{q,\text{int}}\right) dS_q \tag{3.48}$$

Equating RHS of (3.47) and RHS of (3.48), (3.37) becomes

$$\int_{S_1} \left(\overline{E}^b . \overline{J}^a - \overline{H}^b . \overline{M}^a\right) dS_1 = -\int_{S_q} \left(\overline{H}^a_{ext} . \overline{M}^b_{q,ext} + \overline{H}^a_{\text{int}} . \overline{M}^b_{q,\text{int}}\right) dS_q \tag{3.49}$$

In (3.49), only the q^{th} slot is assumed in addition to the p^{th} slot in the waveguide. If the other slots are also assumed to exist in the waveguide, (3.49) can be generalized as, [34], [36],

$$\int_{S_1} \left(\overline{E}^b . \overline{J}^a - \overline{H}^b . \overline{M}^a\right) dS_1 = -\sum_{q=1}^{N}{}' \int_{S_q} \left(\overline{H}^a_{ext} . \overline{M}^b_{q,ext}\right) dS_q - \sum_{q=1}^{M}{}' \int_{S_q} \left(\overline{H}^a_{\text{int}} . \overline{M}^b_{q,\text{int}}\right) dS_q \tag{3.50}$$

where M is the total number of the slots in the same waveguide and N is the total number of the slots in the array. The prime signs on the summations in (3.50) indicates that the case $q = p$ is excluded from the summations.

Inserting (3.38), (3.39), and (3.40)-(3.45) into (3.50), the expression for the backward scattered mode amplitude, B^b_{all} is derived for the p^{th} slot as

$$B_{all}^{b} = \frac{1}{jaN_{\mu_{10}}\mu_{10}\left(\left(k_{\rho}^{TE_{10}^{z}}\right)^{2}/\hat{z}\right)}\left[\begin{array}{l}\sum_{q=1}^{N}{}' \int_{S_q}\left(\frac{\overline{H}_{ext}^{a}}{A^{a}}.\overline{M}_{q,ext}^{b}\right)dS_q + \\ \sum_{q=1}^{M}{}' \int_{S_q}\left(\frac{\overline{H}_{\text{int}}^{a}}{A^{a}}.\overline{M}_{q,\text{int}}^{b}\right)dS_q\end{array}\right] \tag{3.51}$$

where $\overline{H}_{\text{int}}^{a}$ is composed of two parts for the scattered fields in case "*a*" given by

$$\overline{H}_{\text{int}}^{a} = \overline{H}_{\text{int}}^{a,1} + \overline{H}_{\text{int}}^{a,2} \tag{3.52}$$

where $\overline{H}_{\text{int}}^{a,1}$ and $\overline{H}_{\text{int}}^{a,2}$ are TE_{10}^{z} and TE_{m0}^{z} mode components of $\overline{H}_{\text{int}}^{a}$, respectively. B_{all}^{b} can be divided into four parts as follows

$$B_{1}^{b} = \frac{1}{jaN_{\mu_{10}}\mu_{10}\left(\left(k_{\rho}^{TE_{10}^{z}}\right)^{2}/\hat{z}\right)}\sum_{q=1}^{p-1}\int_{S_q}\frac{\overline{H}_{\text{int}}^{a,1}}{A^{a}}.\overline{M}_{q,\text{int}}^{b}dS_q \tag{3.53}$$

$$B_{2}^{b} = \frac{1}{jaN_{\mu_{10}}\mu_{10}\left(\left(k_{\rho}^{TE_{10}^{z}}\right)^{2}/\hat{z}\right)}\sum_{q=p+1}^{M}\int_{S_q}\frac{\overline{H}_{\text{int}}^{a,1}}{A^{a}}.\overline{M}_{q,\text{int}}^{b}dS_q \tag{3.54}$$

$$B_{3}^{b} = \frac{1}{jaN_{\mu_{10}}\mu_{10}\left(\left(k_{\rho}^{TE_{10}^{z}}\right)^{2}/\hat{z}\right)}\sum_{q=1}^{N}{}'\int_{S_q}\left(\frac{\overline{H}_{ext}^{a}}{A^{a}}.\overline{M}_{q,ext}^{b}\right)dS_q \tag{3.55}$$

$$B_{4}^{b} = \frac{1}{jaN_{\mu_{10}}\mu_{10}\left(\left(k_{\rho}^{TE_{10}^{z}}\right)^{2}/\hat{z}\right)}\left[\int_{S_{p-1}}\frac{\overline{H}_{\text{int}}^{a,2}}{A^{a}}.\overline{M}_{p-1,\text{int}}^{b}dS_{p-1} + \int_{S_{p+1}}\frac{\overline{H}_{\text{int}}^{a,2}}{A^{a}}.\overline{M}_{p+1,\text{int}}^{b}dS_{p+1}\right] \tag{3.56}$$

where B_{1}^{b} is the internal TE_{10}^{z} backward scattering mode amplitudes due to the TE_{10}^{z} mode excitation of the slot array and also due to the TE_{10}^{z} mode reflections of all the slots before the p^{th} slot. B_{2}^{b} is the internal TE_{10}^{z} backward scattering mode amplitudes

due to the TE_{10}^{z} mode reflections of the slots located after the p^{th} slot. The effect of B_1^b and B_2^b has already been treated in (3.35) and (3.36). B_3^b and B_4^b are the backward scattering TE_{10}^{z} mode amplitudes due to the external and internal couplings, respectively. B_3^b is caused by the slot voltage, $V_{p,3}^s$. Using (3.55), $V_{p,3}^s$ can be derived.

In (3.55), $\overline{H}_{ext}^a$ is the magnetic field radiated by the slot with slot voltage $V_p^{s,a}$. The equivalent magnetic source for the q^{th} slot is given by

$$\overline{M}_{q,ext}^b = \frac{V_q^{s,b}}{w^s}\cos\left(\frac{\pi\left(\phi-\phi^q\right)}{2\phi_0^q}\right)\hat{a}_\phi \tag{3.57}$$

where $V_q^{s,b}$ is the slot voltage of the q^{th} slot in case "*b*". Since $\overline{M}_{q,ext}^b$ has only $\hat{a}_\phi$-component, only $\hat{a}_\phi$- component of $\overline{H}_{ext}^a$ is needed in (3.55). The $\hat{a}_\phi$- component of $\overline{H}_{ext}^a$ is given using the derivations presented in Appendix B, [38] as

$$H_{ext,\phi}^a\left(\rho_2,\phi,z\right) = \frac{1}{2\pi}\sum_{n=-\infty}^{\infty} e^{jn\phi}\int_{-\infty}^{\infty}\left\{\begin{bmatrix} j\dfrac{\widetilde{E}_z^a\left(n,k_z\right)}{\sqrt{k_0^2-k_z^2}}x \\ \left(\dfrac{nk_z}{\rho_2}\right)^2\dfrac{1}{\omega\mu_0\left(k_0^2-k_z^2\right)}\dfrac{1}{W\left(n,k_z\right)} \\ -\omega\varepsilon_0 W\left(n,k_z\right)\end{bmatrix}e^{jk_z z}\right\}dk_z \tag{3.58}$$

where

$$W\left(n,k_z\right) = \frac{H_n'^{(2)}\left(\rho_2\sqrt{k_0^2-k_z^2}\right)}{H_n^{(2)}\left(\rho_2\sqrt{k_0^2-k_z^2}\right)} \tag{3.59}$$

and where

$$\widetilde{E}_z^a(n,k_z)=\frac{1}{\pi}\frac{V_p^{s,a}}{w^s}\frac{e^{-jk_z z^p}}{k_z}\sin\left(\frac{k_z w^s}{2}\right)e^{-jn\phi^p}\cos\left(n\phi_0^p\right)\left[\frac{\frac{\pi}{\phi_0^p}}{\left(\frac{\pi}{2\phi_0^p}\right)^2-n^2}\right] \tag{3.60}$$

Hence inserting (3.57) and (3.58) into (3.55), and carrying out the calculations, (3.55) becomes

$$B_3^b=\frac{1}{jaN_{\mu_{10}}\mu_{10}\left(\left(k_\rho^{TE_{10}^z}\right)^2/\hat{z}\right)}\sum_{q=1}^{N}{}'\frac{V_q^{s,b}V_p^{s,a}}{A^a}T_{pq} \tag{3.61}$$

where

$$T_{pq}=\sum_{n=-\infty}^{\infty}F_{pq}(n)G_z^{pq}(n) \tag{3.62}$$

and where

$$F_{pq}(n)=e^{jn\left(\phi^q-\phi^p\right)}\cos\left(n\phi_0^q\right)\cos\left(n\phi_0^p\right)\left[\frac{\frac{1}{\phi_0^q}}{\left(\frac{\pi}{2\phi_0^q}\right)^2-n^2}\right]\left[\frac{\frac{1}{\phi_0^p}}{\left(\frac{\pi}{2\phi_0^p}\right)^2-n^2}\right] \tag{3.63}$$

$$G_z^{pq}(n)=\int_0^\infty\frac{j\cos\left(k_z\left(z^q-z^p\right)\right)}{2\sqrt{k_0^2-k_z^2}}\left[\sin c\left(\frac{k_z w^s}{2\pi}\right)\right]^2\left[\begin{array}{c}\frac{(nk_z)^2}{\omega\mu_0\rho_2\left(k_0^2-k_z^2\right)}\frac{1}{W(n,k_z)}\\-\omega\varepsilon_0\rho_2 W(n,k_z)\end{array}\right]dk_z \tag{3.64}$$

In (3.61), $V_q^{s,b}$ is the slot voltage of the q^{th} slot in the slot array, i.e., when all the slots exist in the waveguide array. Hence the superscript "*b*" can be dropped in $V_q^{s,b}$. Moreover, it is clear that $V_p^{s,a} = V_{p,1}^s$ and the ratio, $V_p^{s,a} \big/ A^a$ in (3.61) can be found using (3.35). Note that $A_p^{TE_{10}^z} = A^a$ in (3.61) because A^a is TE_{10}^z mode voltage amplitude used to excite the waveguide in the absence of the other slots as described in case "*a*". When these changes are made in (3.61) and also using (3.21) for the relation between $V_{p,3}^s$ and B_3^b, $V_{p,3}^s$ is found as

$$V_{p,3}^s = \frac{\hat{z} N_{\mu_{10}} a^3 \left(k_\rho^{TE_{10}^z}\right)^2}{\left[B_{\mu_{10}}\left(k_\rho^{TE_{10}^z}\rho_2\right)\right]^2 \pi^2 j\mu_{10}\left(f_p^{TE_{10}^z}\right)^2} \frac{\dfrac{Y_p^s}{G_0}}{2+\dfrac{Y_p^s}{G_0}} \sum_{q=1}^{N}{}' V_q^s T_{pq} \tag{3.65}$$

The last voltage value to be found is $V_{p,4}^s$ which is due to the internal higher order mode couplings. The internal couplings is derived for the general case of TE_{m0}^z couplings because the effect of the internal couplings becomes significant when the height of the waveguide is small, [36] and many TE_{m0}^z modes appear before TM_{mn}^z modes as shown in Table 3.1. Similar procedure described in [36] is used to derive the internal couplings of the slots. The backward scattering TE_{10}^z mode amplitude, B_4^b due to the TE_{m0}^z couplings is derived in (3.56). As a result of the internal couplings, the slot voltage, $V_{p,4}^s$ induces across the terminals of the slot. Hence, the backward scattering TE_{10}^z mode amplitude, B_4^b is scattered due to the slot voltage $V_{p,4}^s$. Note that in deriving (3.56) from (3.51), the expression for B_4^b is found only for the neighbors of the p^{th} slot for simplicity. The equivalent magnetic currents, $\overline{M}_{p-1,\text{int}}^b$ and $\overline{M}_{p+1,\text{int}}^b$, in (3.56) are given by

$$\overline{M}^{\,b}_{p-1,\text{int}} = -\frac{V^s_{p-1}}{w^s}\cos\left(\frac{\pi\left(\phi-\phi^{p-1}\right)}{2\phi_0^{p-1}}\right)\hat{a}_\phi \tag{3.66}$$

$$\overline{M}^{\,b}_{p+1,\text{int}} = -\frac{V^s_{p+1}}{w^s}\cos\left(\frac{\pi\left(\phi-\phi^{p+1}\right)}{2\phi_0^{p+1}}\right)\hat{a}_\phi \tag{3.67}$$

Note that similar to the external coupling derivations using (3.35), the superscript "*b*" is dropped in V^s_{p-1} and V^s_{p+1} in (3.66) and (3.67), respectively. Since $\overline{M}^{\,b}_{p-1,\text{int}}$ and $\overline{M}^{\,b}_{p+1,\text{int}}$ are $\hat{a}_\phi$- directed, only $\hat{a}_\phi$- components of $\overline{H}^{\,a,2}_{\text{int}}$ are needed in (3.56) and they are given by

$$H^{a,2}_{\text{int},\phi} = \begin{cases} B_p^{TE^z_{m0}}\dfrac{j}{\hat{z}\rho_2}\dfrac{m\pi}{a}\cos\left(\dfrac{m\pi z}{a}\right)B_{\mu_{m0}}\left(k_\rho^{TE^z_{m0}}\rho_2\right)\mu_{m0}e^{j\mu_{m0}\left(\phi-\phi^p\right)} & (\phi,z)\in S_{p-1} \\ -C_p^{TE^z_{m0}}\dfrac{j}{\hat{z}\rho_2}\dfrac{m\pi}{a}\cos\left(\dfrac{m\pi z}{a}\right)B_{\mu_{m0}}\left(k_\rho^{TE^z_{m0}}\rho_2\right)\mu_{m0}e^{-j\mu_{m0}\left(\phi-\phi^p\right)} & (\phi,z)\in S_{p+1} \end{cases} \tag{3.68}$$

Using (3.20) and (3.21) for the calculation of $C_p^{TE^z_{m0}}$ and $B_p^{TE^z_{m0}}$, respectively, and inserting (3.66)-(3.68) into (3.56), it is found after lengthy derivations that

$$B_4^b = -\frac{1}{jaN_{\mu_{10}}\mu_{10}\left(\left(k_\rho^{TE^z_{10}}\right)^2/\hat{z}\right)}\frac{V_p^{s,a}}{A^a}\sum_{m=2}^{T}h''_{p,m}\left[h'_{p-1,m}V^s_{p-1}+h'_{p+1,m}V^s_{p+1}\right] \tag{3.69}$$

where

$$h''_{p,m} = K^{TE^z_{m0}}f_p^{TE^z_{m0}} \tag{3.70}$$

$$h'_{p-1,m} = \frac{j}{\hat{z}}\frac{m\pi}{a}\mu_{m0}B_{\mu_{m0}}\left(k_\rho^{TE^z_{m0}}\rho_2\right)\sin c\left(\frac{mw^s}{2a}\right)e^{j\mu_{m0}\left(\phi^{p-1}-\phi^p\right)}f_{p-1}^{TE^z_{m0}} \tag{3.71}$$

$$h'_{p+1,m} = \frac{j}{\hat{z}}\frac{m\pi}{a}\mu_{m0}B_{\mu_{m0}}\left(k_\rho^{TE^z_{m0}}\rho_2\right)\sin c\left(\frac{mw^s}{2a}\right)e^{-j\mu_{m0}\left(\phi^{p+1}-\phi^p\right)}f_{p+1}^{TE^z_{m0}} \tag{3.72}$$

Using the relation between B_4^b and $V_{p,4}^s$ given in (3.21) for TE_{10}^z mode and also using (3.35) for the ratio $V_p^{s,a}/A^a$, $V_{p,4}^s$ is derived using (3.69) as

$$V_{p,4}^s = -\frac{\hat{z}a^3\left(k_\rho^{TE^z_{10}}\right)^2 N_{\mu_{10}}}{j\mu_{10}\pi^2\left[B_{\mu_{10}}\left(k_\rho^{TE^z_{10}}\rho_2\right)\right]^2}\frac{1}{\left(f_p^{TE^z_{10}}\right)^2}\frac{\frac{Y_p^s}{G_0}}{2+\frac{Y_p^s}{G_0}}\sum_{m=2}^{T}h''_{p,m}\left[h'_{p-1,m}V_{p-1}^s + h'_{p+1,m}V_{p+1}^s\right] \tag{3.73}$$

The active admittance formula of the shunt slot in terms of the incident and scattered mode amplitudes in the circuit model can be derived as [33], [34]

$$\frac{Y_p^a}{G_0} = \frac{2B_{10}^p}{A_{10}^p - D_{10}^p - B_{10}^p} \tag{3.74}$$

where A_{10}^p and D_{10}^p are the incident mode voltage amplitudes while B_{10}^p is the scattered mode voltage amplitude for the p^{th} slot as described in Figure 3.5. In (3.74), A_{10}^p and D_{10}^p can be replaced by $A_p^{TE^z_{10}}$ and $D_p^{TE^z_{10}}$ while B_{10}^p can be replaced by B_{all}^b. The values of $A_p^{TE^z_{10}}$ and $D_p^{TE^z_{10}}$ can be found from (3.35) and (3.36), respectively. Also using (3.21) to obtain $B_{all}^b = K^{TE^z_{10}}f_p^{TE^z_{10}}V_p^s$, where $V_p^s = V_{p,1}^s + V_{p,2}^s + V_{p,3}^s + V_{p,4}^s$ derived in this section, one can arrive at the second active admittance formula given by

$$\frac{Y_p^a}{G_0} = \frac{2\left(f_p^{TE_{10}^z}\right)^2}{\dfrac{2\left(f_p^{TE_{10}^z}\right)^2}{\dfrac{Y_p^s}{G_0}} - \dfrac{\hat{z}N_{\mu_{10}}a^3\left(k_\rho^{TE_{10}^z}\right)^2}{\left[B_{\mu_{10}}\left(k_\rho^{TE_{10}^z}\rho_2\right)\right]^2\pi^2 j\mu_{10}}\left(\sum_{q=1}^{N}{}' \frac{V_q^s}{V_p^s}T_{pq} - \sum_{m=2}^{T} h''_{p,m}\left[h'_{p-1,m}\frac{V_{p-1}^s}{V_p^s} + h'_{p+1,m}\frac{V_{p+1}^s}{V_p^s}\right]\right)} \quad (3.75)$$

In (3.75), T is the total number of higher order TE_{m0}^z modes before TM_{mn}^z modes excite. It is usually enough to consider only the TE_{20}^z higher order mode couplings. Hence, T is taken as *2* in (3.75) for the calculation of the active admittances carried out in this thesis.

3.2. Design Procedure of Slotted CSIW Array

The active admittances derived in Section 3.1 can be used to design slotted CSIW arrays. In this study, the design procedure presented by Elliott [34], [40] for the planar slotted waveguides is used. There are two types of planar slotted waveguide arrays, namely, standing wave and traveling wave slot array which can be designed using the active admittance formulations. Since a traveling wave type of array is considered to be implemented on CSIW, the design procedure for the traveling wave type of slot waveguide array is outlined which can be used for CSIW case. The traveling wave slot array is excited from one side and the other side of the array is terminated by a match load. The slots are usually placed in an alternating manner as shown in Figure 1.2 which causes a phase shift of π in addition to the phase delay between the succeeding slots. The spacing between the slot elements in the design is slightly greater or smaller than $\lambda_g/2$ in order to prevent the reflections at each slot to add up, and hence, to prevent the mismatch. Since the slots are not separated by $\lambda_g/2$, allocating alternating slots does not help to have the same phase for all the slots. Hence beam is tilted from broadside of the array. If the slots are placed in an

alternating manner, the element spacing lower than $\lambda_g/2$ and greater than $\lambda_g/2$ corresponds to backward firing and forward firing radiation cases, respectively [33].

The admittance of the single longitudinal slot is the self-admittance of the slot characterized in Section 2.3. For the p^{th} slot in the waveguide, the self-admittance is abbreviated as Y_p^s / G_0 in (3.75). The self-admittance is usually found by full wave simulators such as HFSS and then characterization polynomials are derived. The characterization polynomials are used in the design of the slotted waveguide array. When the other slots are present in the array, the slot admittance is presented by the active shunt admittances that include the effects of mutual couplings with the other slots as in (3.75). The circuit model of the traveling wave array composed of longitudinal slots on the broad wall of the waveguide is shown in Figure 3.9. The circuit model is constructed by using the normalized active slot admittances, Y_p^a for $p = 1, 2, \ldots, M$ where M is the total number of the slots in the same waveguide with spacing, d, in the array. The slot separations need not necessarily to be taken as uniform and the design procedure can be modified for non-uniform slot separation values. The normalization of the active slot admittances are carried out with respect to the characteristic impedance of the waveguide. The power-voltage definition of the characteristic impedance of the waveguide is used in normalizing the active slot admittances [41]. Since the reflections from the end of the circuit are not desired in the traveling wave array, the circuit model is terminated by a match load at the end.

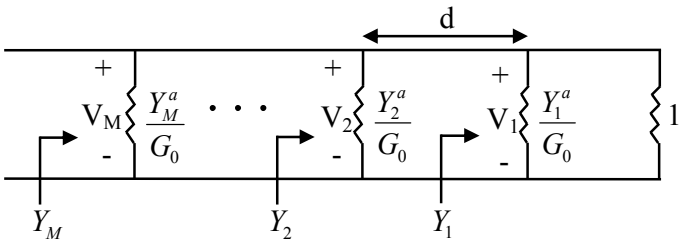

Figure 3.9: Circuit model representation of a traveling wave shunt slot array.

The design of the slotted waveguide array is based on two equations derived in Section 3.1.2. Using (3.29), the ratio of the active admittances of two slots in the waveguide can be written as

$$\frac{Y_p^a\left(z_p,l_p\right)}{Y_q^a\left(z_q,l_q\right)}=\frac{f_p^{TE_{10}^z}\left(z_p,l_p\right)V_p^sV_q}{f_q^{TE_{10}^z}\left(z_q,l_q\right)V_q^sV_p} \tag{3.76}$$

where z_p is the slot offset and $l_p=\rho_2\phi_0^p$ is the half-length of the p^{th} slot, respectively.

Total admittance seen by the p^{th} slot is given by

$$Y_p=Y_p^a+\frac{Y_{p-1}\cos\left(\beta_{10}d\right)+j\sin\left(\beta_{10}d\right)}{\cos\left(\beta_{10}d\right)+jY_{p-1}\sin\left(\beta_{10}d\right)} \tag{3.77}$$

where Y_p is total admittance seen from right in the region of the p^{th} slot shown in Figure 3.9 and β_{10} is the propagation constant of the fundamental mode in the waveguide.

The complex mode voltages of consecutive slots are related by

$$V_p=V_{p-1}\left[\cos\left(\beta_{10}d\right)+jY_{p-1}\sin\left(\beta_{10}d\right)\right] \tag{3.78}$$

Using (3.77) and (3.78), (3.76) can be rewritten for two successive slots as

$$\frac{Y_p^a\left(z_p,l_p\right)}{f_p^{TE_{10}^z}\left(z_p,l_p\right)}=\frac{Y_{p-1}^a\left(z_{p-1},l_{p-1}\right)}{f_{p-1}^{TE_{10}^z}\left(z_{p-1},l_{p-1}\right)}\frac{V_p^s/V_{p-1}^s}{\cos\left(\beta_{10}d\right)+jY_{p-1}\sin\left(\beta_{10}d\right)} \tag{3.79}$$

The design procedure can be summarized as follows:

- The ratio of the complex slot voltages V_p^s / V_q^s are determined by the pattern requirements, such as low SLL or desired beam shape. The phases of the slot voltages should be taken into wherever needed, such as in the mutual coupling calculations and in (3.79).
- The spacing d between the elements is determined by the pattern requirements such as direction of the maximum radiation and avoiding grating lobes. Small d may cause strong mutual coupling that might not allow making a design.
- Mutual coupling terms in (3.75) are calculated assuming zero slot offsets and resonant slot lengths for all the slots in the array.
- An initial value for the last slot offset z_1 is chosen. It will affect the values of the other slot offsets and determine the power dissipated at the load.
- The mode voltage at the first slot is taken as unity. In case of multiple parallel waveguides fed by coherent modes, the phase of the mode voltage is determined by the phase of the mode at the input port of the waveguide. If the first slot is desired to be at resonance, the phase value for the slot which is the same as the phase of the mode voltage is used. Although there are complex multiplicative terms in (3.29), this convention can still be used which causes a phase shift with the same amount for all the slots in all the waveguides. Slot length l_1 is determined by diminishing the imaginary part of (3.75) if the first slot is desired to be at resonance. If the first slot is not at resonance, l_1 is determined such that the required phase value is satisfied in (3.75). The amount of deviation of the slot from resonance is determined by the deviation of the phase of the slot voltage from the phase of the mode voltage. Using the slot offset, z_1 and length, l_1, the self-admittance of the slot is determined by the characterization polynomials. Hence, $Y_1^a(z_1, l_1) / f_1^{TE_{10}^z}(z_1, l_1)$ is determined. Y_1 is found using (3.77). The value of $Y_2^a(z_2, l_2) / f_2^{TE_{10}^z}(z_2, l_2)$ is determined using (3.79).

- Next step is to search for (z_2, l_2) such that the same $Y_2^a(z_2, l_2) / f_2^{TE_{10}^z}(z_2, l_2)$ value is found as the previous step using (3.75). The error function is formed by taking the absolute value of the difference between two $Y_2^a(z_2, l_2) / f_2^{TE_{10}^z}(z_2, l_2)$ values found using different equations, i.e., using (3.75) and (3.79). The error function is minimized to find the best slot offset and length pair which satisfies desired active admittance value.
- The procedure is repeated until all (z_N, l_N) pairs are found.
- The mutual coupling terms in (3.75) are recalculated with new set of slot offsets and lengths. The procedure listed above is repeated until final slot offsets and lengths converge.
- If the value of Y_M does not give good matching, the separation *d* between the slots can be altered slightly and the design procedure should be repeated.

After finding all the slot offsets and lengths, power delivered load is calculated using the power dissipated at the p^{th} slot which is given by

$$P_p = \frac{1}{2}\mathrm{Re}\left(V_p V_p^* \left(\frac{Y_p^a}{G_0} \right)^* \right) \tag{3.80}$$

and power delivered to load can be written as

$$P_L = \frac{\frac{1}{2} V_1 V_1^*}{\frac{1}{2} V_1 V_1^* + \sum_{p=1}^{M} P_p} \tag{3.81}$$

If the power delivered to the load is greater than the desired limit, the value of the initial slot offset, z_1 should be increased and the design procedure should be repeated.

3.3. Numerical Results

The numerical results are presented to examine the mutual couplings of the slots using the formulations carried out in Section 3.1. The validity of the Elliott's design procedure has already been proved in the literature for the slotted planar waveguides and also in Chapter 4 for the slotted CSIW. In this part, the derived mutual coupling formulas are compared with the planar formulations, formulations of previous studies, and HFSS simulations.

There are some difficulties in the internal and external coupling calculations. In the calculation of the internal couplings, the evaluations of the Bessel functions with complex orders are required in some of the terms such as in (3.24) and (A.31). Such kind of calculations is carried out using the Symbolic Math Toolbox in MATLAB. The calculation of the external couplings requires the numerical integral to be taken over complex domain because the term, $G_z^{pq}(n)$ in (3.64) has poles at $k_z = k_0$. In order to avoid pole and branch point singularities, the integral path is deformed as shown in Figure 3.10. In order to avoid computer underflow and overflow while carrying out the calculations of the Hankel function terms in (3.64) are written in the form of ratios as in (3.59) and the asymptotic forms for the ratios of the Hankel

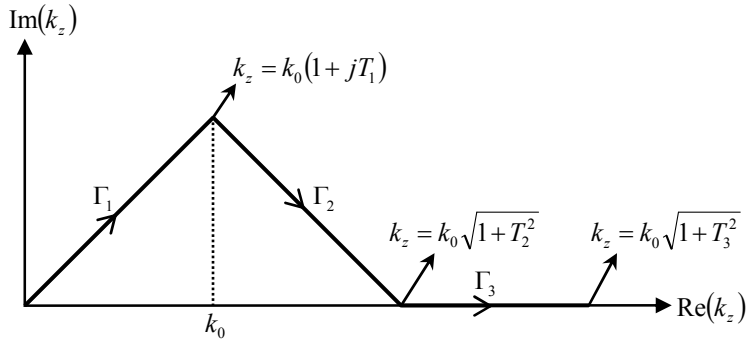

Figure 3.10: Deformed integration path.

functions of large orders and arguments derived in Appendix C are used wherever needed in the integration.

The path of integration shown in Figure 3.10 is divided into three regions, similar to the ones presented in [42] - [44]. Three regions are represented as

$$\Gamma_1 : k_z = k_0\left(1 + jT_1\right)\frac{t_1}{T_1}, \quad 0 \le t_1 \le T_1 \tag{3.82}$$

$$\Gamma_2 : k_z = k_0\left[1 + jT_1 + \left(\sqrt{1+T_2^2} - \left(1 + jT_1\right)\right)\frac{t_2}{T_2 - T_1}\right], \quad 0 \le t_2 \le T_2 - T_1 \tag{3.83}$$

$$\Gamma_3 : k_z = k_0\left[\sqrt{1+T_2^2} + \left(\sqrt{1+T_3^2} - \sqrt{1+T_2^2}\right)\frac{t_3}{T_3 - T_2}\right], \quad 0 \le t_3 \le T_3 - T_2 \tag{3.84}$$

where Γ_1, Γ_2, and Γ_3 are paths of integration shown in Figure 3.10.

Three regions in Figure 3.10 are uniformly sampled. The mutual coupling term presented in (3.62) is computed by assuming resonant slots at *25 GHz*. Two different codes are generated to calculate (3.62) at *25 GHz*. The number of *n* values to be summed at each step is kept constant in both of the codes. In the first code, the value of T_3 is kept constant and the summation is carried out over *n* in (3.62) till convergence is obtained. In the second code, the value of T_3 is extended at each summation step and the summation is also carried out for previous and new *n* values. The first code is preferred to be used in the calculations because it is faster due to the constant value of T_3. Two codes are compared and the parameters are determined for the first code as $T_1 = 0.1$, $T_2 = 1$, $T_3 = 30$, and maximum number of terms in (3.62) to be summed over *n* at each step is determined as *200* including positive and negative *n* values.

3.3.1. External Couplings of Two Slots on PEC Cylinder

The external coupling formulations derived for the slots on cylindrical surface in this thesis are compared with the literature. For this purpose, two slots are assumed to be placed on PEC cylinder as shown in Figure 3.11. Mutual admittance of the slots are calculated and compared with the results presented in [45]. The widths of the slots in [45] shown Figure 3.11 are $w_p = w_q = 0.4\ in$ and lengths of the slots are $L_p = L_q = 0.9\ in$. The radius of the cylinder is $\rho_2 = 1.991\ in$. The angular displacement between the centers of the slots is ϕ_0 while the displacement between the centers of the slots in $\hat{a}_z$-direction is z_0. The mutual admittance calculation frequency is *9 GHz*. Similar to the mutual admittance definition given in [45], the mutual admittance of the slots on PEC cylinder is defined as

$$Y_{pq} = -\frac{1}{V_q^s V_p^s} \int_{S_q} \left(\overline{H}^p . \overline{M}_q \right) dS_q \tag{3.85}$$

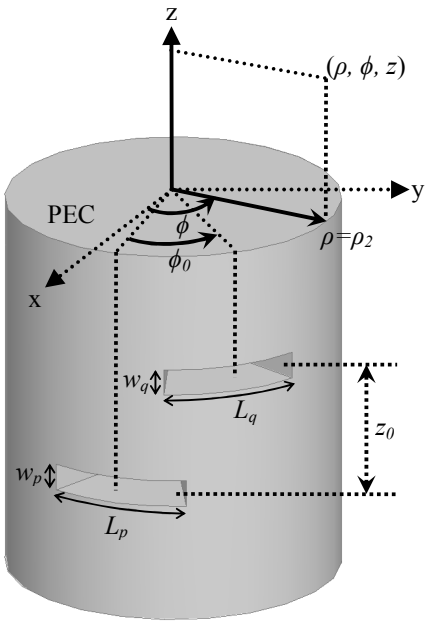

Figure 3.11: Two slots on cylindrical PEC.

where V_p^s and V_q^s are the slot voltages while $\overline{H}^p$ is the magnetic field radiated by the p^{th} slot. $\overline{M}_q$ is the equivalent magnetic current of the q^{th} slot defined on the surface of the q^{th} slot, S_q. The magnitude of the mutual admittance in dB scale is given by

$$\left(Y_{pq}\right)_{dB} = 20\log_{10}\left(\left|Y_{pq}\right|\right) \tag{3.86}$$

The mutual admittance values presented by (3.85) are derived for cylindrical PEC case by using the formulations similar to the ones derived in Section 3.1.2.3. It is found that the mutual admittance given in (3.85) equals to the minus of the external mutual coupling term, $-T_{pq}$, presented in (3.62). Hence, comparing the mutual admittance calculations with the literature also tests the accuracy of the external coupling formulations derived in this thesis.

Modal solution, asymptotic solution and geometrical theory of diffraction (GTD) solution for the mutual admittance of the slots are derived in [45]. Modal solution is the exact solution. In [45], the mutual admittance of the slots is calculated for various ϕ_0 and z_0 values at *9 GHz* using modal solution, asymptotic solution, and GTD solution and they are listed in Table 3.2, Table 3.3, and Table 3.4. In Table 3.2 and

Table 3.2: Comparison of the Y_{pq} values for $z_0 = 0$" with the literature [45].

$z_0 = 0$"	Modal Solution [45]	Asymptotic Solutions			This Thesis
ϕ_0		Chang [46]	Lee [47]	Asymptotic [45]	
30°	-81.33 *dB* -77°	-83.14 *dB* -60°	-81.34 *dB* -75°	-80.83 *dB* -81°	-80.18 *dB* -77.28°
40°	-89.87 *dB* 168°	-91.11 *dB* 180°	-90.02 *dB* 170°	-88.69 *dB* 159°	-88.71 *dB* -168.20°
50°	-96.37 *dB* 58°	-97.43 *dB* 69°	-96.72 *dB* 61°	-94.35 *dB* 45°	-95.30 *dB* 58.58°
60°	-101.97 *dB* -49°	-102.93 *dB* -39°	-102.48 *dB* -47°	-98.96 *dB* -66°	-101.03 *dB* -49.57°

Table 3.3, the modal solution and asymptotic solution derived in [45] are compared with the asymptotic solutions given in [46] and [47] while the modal solution and GTD solution derived in [45] are compared in Table 3.4.

Table 3.3: Comparison of the Y_{pq} values for $\phi_0 = 0°$ with the literature [45].

$\phi_0 = 0°$	Modal Solution [45]	Asymptotic Solutions			This Thesis
z_0		Chang [46]	Lee [47]	Asymptotic [45]	
0.5"	-62.62 *dB* -72°	-61.7 *dB* -68°	-62.54 *dB* -72°	-62.41 *dB* -73°	-61.53 *dB* -72.07°
2"	-71.78 *dB* -117°	-70.96 *dB* -118°	-71.66 *dB* -116°	-71.84 *dB* -119°	-70.76 *dB* -116.09°
8"	-81.84 *dB* 34°	-80.80 *dB* 34°	-81.83 *dB* 37°	-82.18 *dB* 30°	-80.61 *dB* 31.95°
16"	-86.48 *dB* -4°	-85.26 *dB* -4°	-86.6 *dB* -1°	-86.96 *dB* -9°	-84.92 *dB* -7.02°
40"	-91.95 *dB* -115°	-90.83 *dB* -112°	-92.46 *dB* -110°	-92.77 *dB* -120°	-91.05 *dB* -113.20°

The mutual admittance calculations of the slots are carried out using the formulations derived in this thesis and they are compared with the results presented in [45], [46], and [47] as shown in Table 3.2, Table 3.3, and Table 3.4. As it is seen in Table 3.2, Table 3.3, and Table 3.4, the calculations carried out using the formulations derived in this thesis is in a good agreement with the results presented in [45], [46], and [47].

Table 3.4: Comparison of the Y_{pq} values for various z_0 and ϕ_0 values with the literature [45].

ϕ_0	z_0	Modal Solution [45]	GTD Solution [45]	This Thesis
0°	0.5"	-62.62 *dB* -72°	-62.54 *dB* -72°	-61.53 *dB* -72.07°
	2"	-71.78 *dB* -117°	-71.66 *dB* -116°	-70.76 *dB* -116.09°
	8"	-81.84 *dB* 34°	-81.83 *dB* 37°	-80.61 *dB* 31.95°
	40"	-91.95 *dB* -115°	-92.46 *dB* -110°	-91.05 *dB* -113.20°
30°	2"	-77.42 *dB* 175°	-77.69 *dB* 177°	-76.46 *dB* 175.49°
60°		-90.00 *dB* -3°	-90.17 *dB* -1°	-88.74 *dB* -4.11°
90°		-102.52 *dB* 120°	-103.10 *dB* 116°	-101.99 *dB* 114.00°
30°	0"	-81.33 *dB* -77°	-81.34 *dB* -75°	-80.18 *dB* -77.28°
40°		-89.87 *dB* 168°	-90.02 *dB* 170°	-88.72 *dB* 168.20°
60°		-101.97 *dB* -49°	-102.48 *dB* -47°	-101.03 *dB* -49.57°

3.3.2. External and Internal Couplings of Two Slots on CSIW

The formulations derived for external and internal couplings of the slots on E-plane bend regular waveguides are compared with the simulations to see the validity of them. For this purpose the CSIW with longitudinal slot structure is chosen with the same CSIW parameters presented in Section 2.1. The CSIW with radius R is used in the calculations at *25 GHz* as shown in Figure 1.2. Two different cases are considered as shown in Figure 3.12 (a) and (b), respectively. In the first case shown in Figure 3.12 (a), two slots with slot offsets z_p and z_q, respectively, and lengths L_p and L_q, respectively, lie in the same CSIW while in the second case shown in Figure 3.12 (b), the slots are located at two separate parallel CSIW structures. The CSIW structure is formed using *0.5 mm*-thick Rogers *3003* substrate. The diameter and period of the vias are *0.8 mm* and *1 mm*, respectively. The widths of the slots are chosen as *0.25 mm*. The width of the CSIW, W measured from the centers of the vias, is *6 mm*. In Figure 3.12, the wave ports are used to excite the CSIW at *25 GHz*

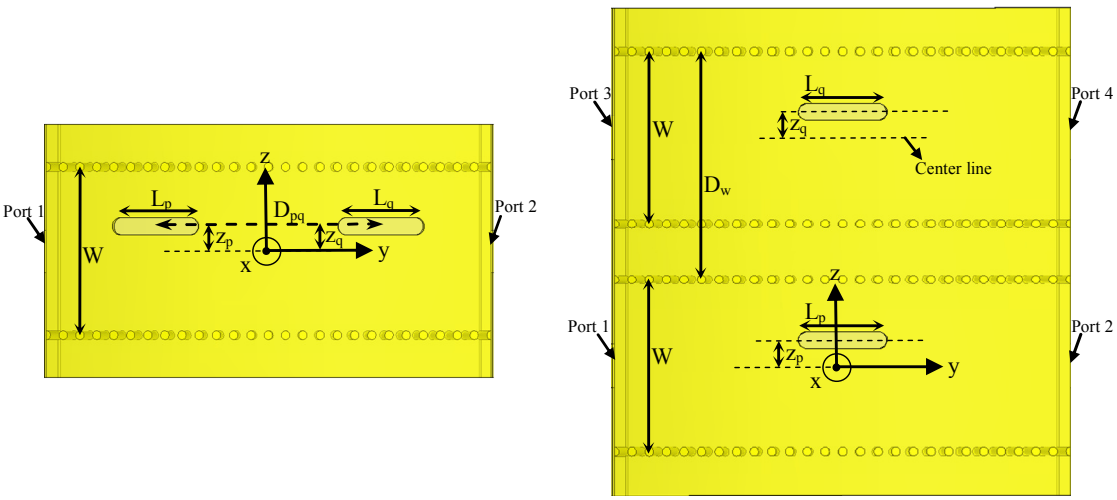

(a) (b)

Figure 3.12: (a) Longitudinal slots on the same CSIW. (b) Longitudinal slots on two parallel CSIW.

instead of the microstrip transitions. Port1 is excited in Figure 3.12 (a) while Port1 and Port3 are excited in Figure 3.12 (b). All the other ports are terminated by a matched load. The width of the wave port is chosen as the equivalent width of the CSIW in order to reduce the reflections at the ports.

In both of the cases shown in Figure 3.12 (a) and (b), the simulation results are compared with the transmission line models composed of shunt active admittances representing the slots. The active admittance calculations are carried out using the active admittance formulation given in (3.75). Note that both external and internal coupling terms are used in (3.75) for the case given in Figure 3.12 (a) while only the external coupling terms are used for the structure given in Figure 3.12 (b). Furthermore, all the s-parameters are also calculated by ignoring the mutual couplings and also by using the planar coupling formulations given in [34] and [36]. The calculations for the planar case are carried out by modifying the self-admittance term in (3.75) by the coupling terms derived for the planar case given in [34] and [36].

First of all, the first case is considered as shown in Figure 3.12 (a). The circuit model of two longitudinal slots on the same CSIW shown in Figure 3.12 (a) is presented in Figure 3.13. In the simulations, both of the slots are excited when Port1 is excited. Hence, the circuit model shown in Figure 3.13 contains active admittance terms. However, s-parameters calculated using the circuit model shown in Figure 3.13 corresponds to the passive s-parameters in the simulator because Port2 is terminated

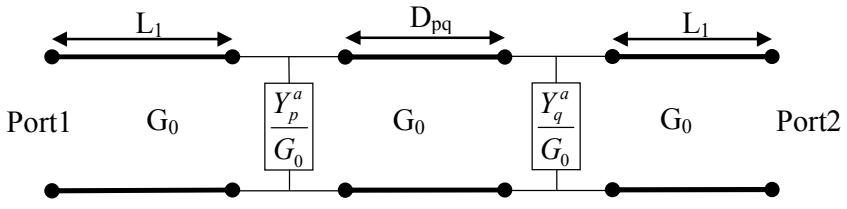

Figure 3.13: Circuit model of two longitudinal slots on the same CSIW.

by a matched load in the calculation of S_{11} parameter in the simulations. The derived active admittance formulas are used in the transmission line model shown in Figure 3.13 and the related s-parameters are calculated. In the calculations, the effect of the transmission line lengths, L_1 are extracted and ports are embedded till the centers of the slots both in the simulations and closed form calculations. In order to see the effect of slot offset in Figure 3.12 (a) for $R = 10\ cm$, the value of the slot separation distance D_{pq} is kept constant at $5\ mm$ and z_q is set to $0.5\ mm$. The slot offset z_p is varied between $-0.5\ mm$ and $0.5\ mm$ while the slot lengths are $L_p = L_q = 4.2\ mm$ and the results are compared in Figure 3.14. As it is seen in Figure 3.14, there is almost perfect agreement between the formulations with mutual coupling calculations and simulations. Since the couplings for cylindrical and planar cases almost converge for radius values greater than $2\lambda_0$, there is almost no difference between the calculations using planar and cylindrical formulations.

The effect of the distance between slots, D_{pq} measured from centers of the slots, are examined by setting the slot offsets, $z_p = 0.2\ mm$, $z_q = 0.5\ mm$ and by setting the lengths, $L_p = L_q = 4.2\ mm$ for $R = 10\ cm$. The value of D_{pq} is varied between $5\ mm$

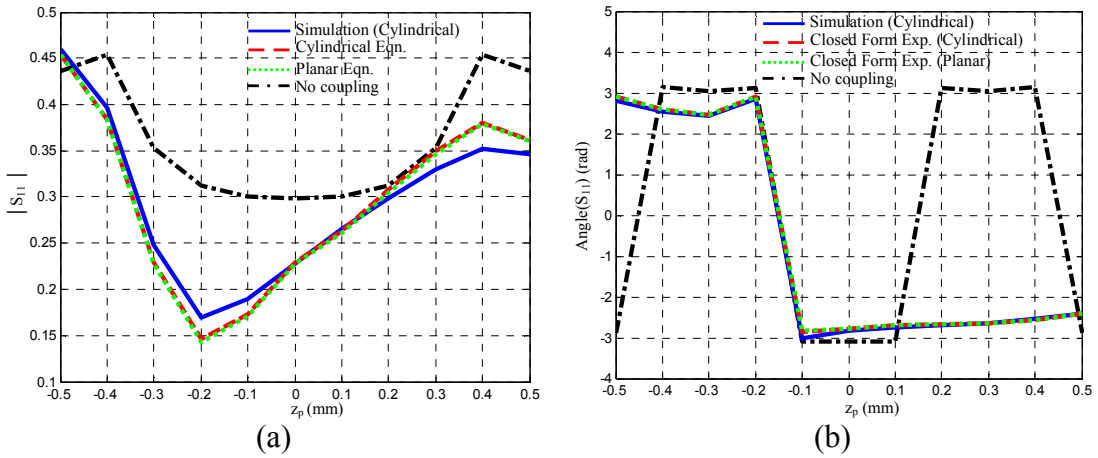

(a) (b)

Figure 3.14: (a) Magnitude and (b) phase of S_{11} ($R = 10\ cm$, $D_{pq} = 5\ mm$, and $z_q = 0.5\ mm$).

and *25 mm* and the simulations are carried out by exciting the structure from Port1 while Port2 is terminated by a matched load. The simulations are compared with the calculations carried out using active admittance formulas and transmission line model in Figure 3.15. As it is seen in Figure 3.15, there is almost no difference between the s-parameters in different cases. Since the effect of the mutual couplings are not significant for $z_p = 0.2\ mm$ in Figure 3.14 (a), there is almost no difference between the calculations carried out by considering and ignoring the mutual coupling effects in Figure 3.15 (a).

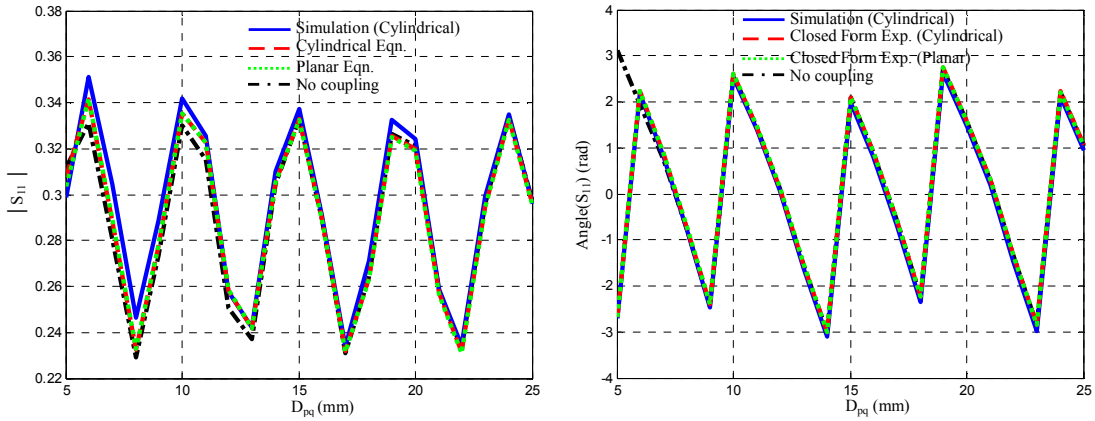

Figure 3.15: (a) Magnitude and (b) phase of S_{11} ($R = 10\ cm$, $z_p = 0.2\ mm$, and $z_q = 0.5\ mm$).

The calculations and simulations shown in Figure 3.15 are repeated for the case where $z_p = -0.2\ mm$ for $R = 10\ cm$ to see the effect of the mutual coupling. The simulated and calculated results are compared in Figure 3.16. As it is seen in Figure 3.16, the mutual couplings are significant for the D_{pq} values between *5 mm* and *6 mm*. The simulated response is in a good agreement with the values obtained by taking the mutual coupling into account; however, there is almost no difference between the planar and cylindrical equations.

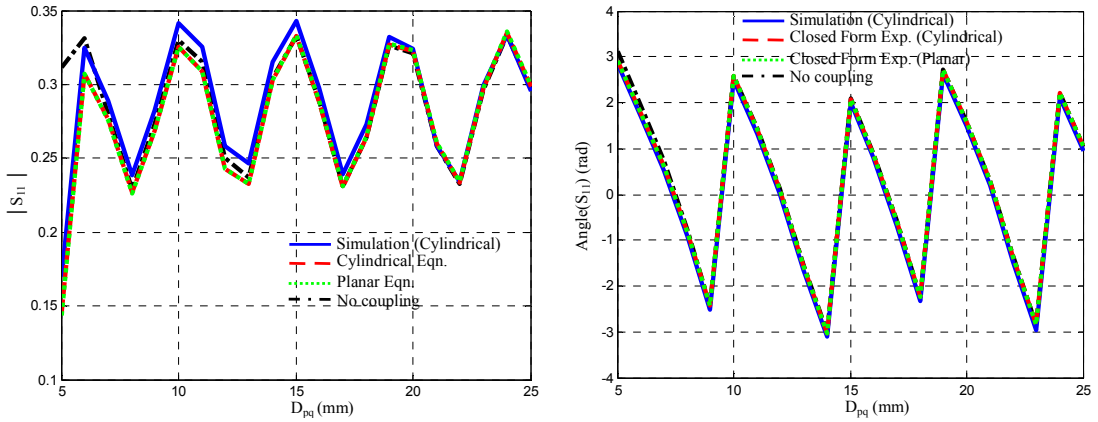

(a) (b)

Figure 3.16: (a) Magnitude and (b) phase of S_{11} (R = *10 cm*, z_p = *-0.2 mm,* and z_q = *0.5 mm*).

In order to see the difference between the cylindrical and planar equations, the value of the radius R is reduced from *10 cm* to *0.6 cm* for the case presented in Figure 3.16. The simulations and calculations are carried out and presented in Figure 3.17. As it is

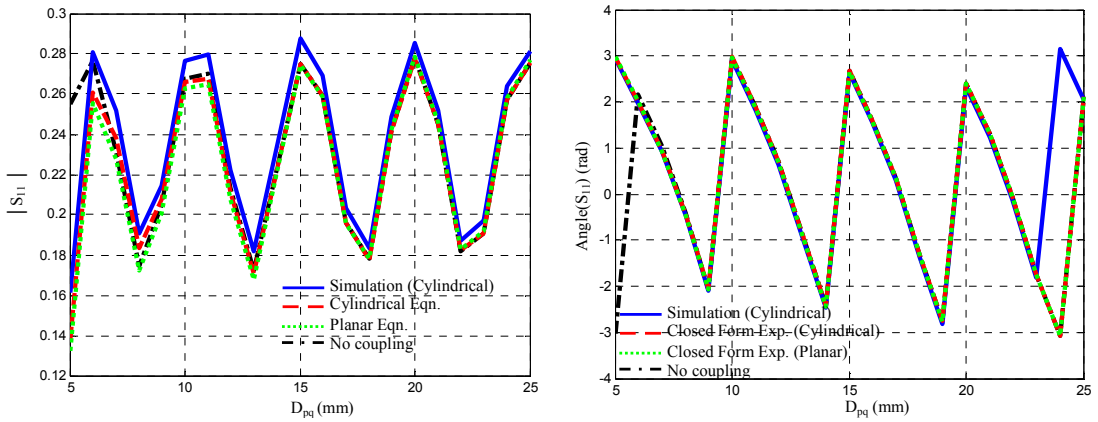

(a) (b)

Figure 3.17: (a) Magnitude and (b) phase of S_{11} (R = *0.6 cm*, z_p = *-0.2 mm,* and z_q = *0.5 mm*).

seem in Figure 3.17, the results are similar to the ones presented in Figure 3.16. Using such a low radius value does not make any difference between the cylindrical and planar equations.

Secondly, similar calculations are carried out for the case shown in Figure 3.12 (b). The circuit model of the p^{th} slot shown in Figure 3.12 (b) is presented in Figure 3.18. In Figure 3.18, the active admittance model is used because both Port1 and Port3 are excited with the same amplitude and phase in Figure 3.12 (b). In the calculations, the effect of the transmission line lengths L_1 are extracted and ports are embedded till the centers of the slots both in the simulations and closed form calculations. In the circuit model, the s-parameters calculated using active admittance values corresponds to calculating the active s-parameters in the simulator. The active s-parameters calculated in the simulator is given by

$$ActiveS_{nn} = \sum_{m=1}^{M'} a_m S_{mn} \tag{3.87}$$

where n stands for the port number and a_m is the excitation coefficient at Port m. M' is the total number of ports in the structure and S_{mn} is the s-parameter representing the coupling between Port m and Port n.

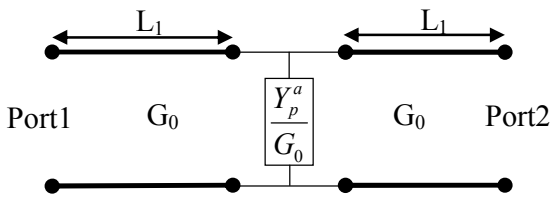

Figure 3.18: Circuit model of the longitudinal slot on CSIW.

First of all, the waveguide separation, D_w, is kept constant at *6 mm* with $z_q = 0.5\ mm$ in Figure 3.12 (b) for $R = 10\ cm$. Then the value of z_p is varied by setting $L_p = L_q = 4.2\ mm$. The calculated results are compared with the simulations in Figure 3.19. As it is seen in Figure 3.19, there is good agreement between different cases. The other simulations are carried out by sweeping D_w between *6 mm* and *24 mm* for $R = 10\ cm$, $z_p = 0.2\ mm$, $z_q = 0.5\ mm$, and $L_p = L_q = 4.2\ mm$. The closed form calculations are also carried out for the same D_w values and they are compared with the simulations in Figure 3.20. Again good agreement between the closed form calculations carried out by transmission line model and simulations is obtained and mutual couplings are nicely expected. Almost no difference between the planar and cylindrical formulations is obtained because of electrically large radius as stated before.

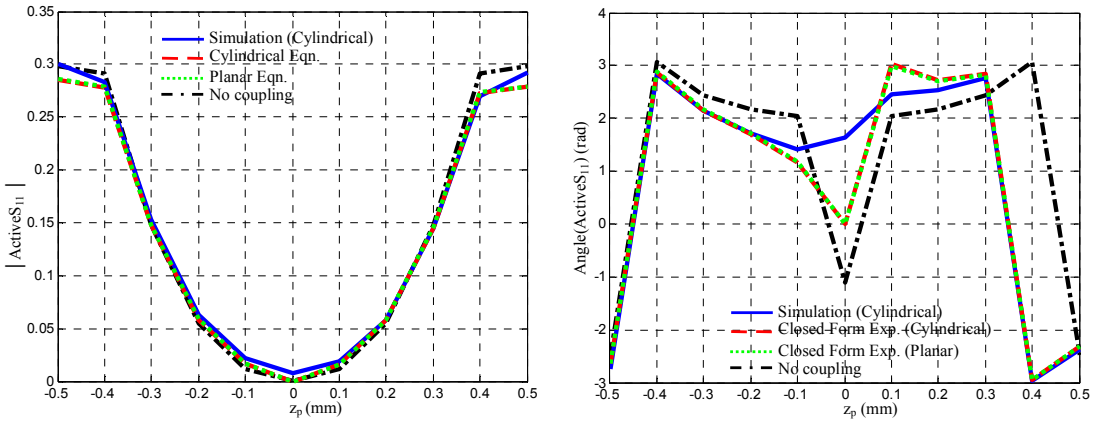

(a) (b)

Figure 3.19: (a) Magnitude and (b) phase of active S_{11} ($R = 10\ cm$, $z_q = 0.5\ mm$ and $D_w = 6\ mm$).

In Figure 3.14 and Figure 3.19, symmetrical s-parameter graphs are obtained when the mutual couplings are not taken into account. This is because; the slots are coupled in different manner when the signs of the slot offsets are changed since the

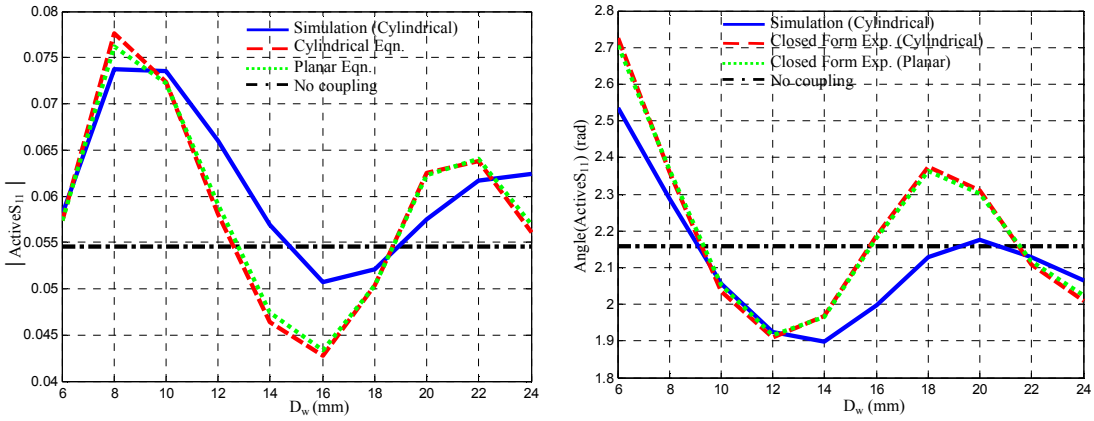

Figure 3.20: (a) Magnitude and (b) phase of active S_{11} ($R = 10\ cm$, $z_p = 0.2\ mm$ and $z_q = 0.5\ mm$).

distance between the slots change. When the mutual couplings are ignored, the active admittance values in the circuit model become self-slot admittances which can be seen in (3.75). Since the self-slot admittances are not affected by the sign change in the slot offset, the s-parameter graphs in Figure 3.14 and Figure 3.19 becomes symmetrical. The phases are also not affected by the sign change in the slot offset because both the slot offset V_p^s and the term $f_p^{TE_{10}^z}$ in (3.31) experience $180°$ phase shift as a result of the change in the sign of the slot offset. Hence, the phase value of the admittance does not change in (3.29) with respect to the sign of the slot offset.

CHAPTER 4

DESIGN OF TRAVELING WAVE CSIW SLOT ARRAY

This chapter presents different designs of traveling wave longitudinal slot array on CSIW at *25 GHz*. The designs of slot array on CSIW are carried out using non-uniformly distributed slot elements near resonance and uniformly spaced slot elements with large deviations from resonance. In both of the methods applied in slot separations, the aperture projection method is used to reduce SLL. The non-uniform slot array is designed on CSIW for beam steering applications while the uniform slot array is designed for pattern synthesis applications. The slotted CSIW arrays presented in this chapter look like periodic leaky wave antennas in the sense that the fundamental mode propagating in the CSIW is a slow wave for frequencies above *20 GHz* due to dielectric filling in the CSIW. The slow waves do not radiate and the radiation into free space is obtained by periodic placement of the slots as in the periodic leaky wave antennas. Hence, the radiation into both backward and forward quadrants, i.e., before and after the broadside direction, can be obtained by frequency change [48].

Section 4.1 examines the pattern synthesis methods, specifically the aperture projection method for the slotted CSIW arrays. Section 4.2 presents the slotted CSIW array with non-uniformly distributed slot elements near resonance while Section 4.3 shows a pattern synthesis application with uniformly distributed slot array on CSIW where the slot elements are largely deviated from resonance. The fabrication and measurements of the traveling wave slot arrays on CSIW are given in each section.

4.1. Pattern Synthesis Methods

Pattern synthesis of an array can be carried out by considering different objectives, such as pencil beam and low SLL, shaped beam synthesis, and some performance indices such as directivity, cross-polarization, and bandwidth. For conformal array applications, some of the classical methods such as Woodward-Lawson, Dolph-Chebyshev synthesis, Fourier synthesis and the methods using Taylor line source synthesis or optimization tools such as genetic algorithm and particle swarm optimization can be used [1], [49]. In this thesis, the aim is to obtain low SLL and narrow HPBW using slot array on CSIW. So, aperture projection method as shown in Figure 4.1 is used together with Taylor line source distribution to reduce the SLL. Genetic algorithm optimization is used together with the aperture projection method to design the phases of the elements in the pattern synthesis applied in Section 4.3. The aperture projection method is examined in detail for the slot array on cylindrical surface in the next section. The effect of the uniform and non-uniform sampling of the Taylor line source distribution, i.e., the effect of the element density on the array weights, [50], [51], is searched by considering the isotropic sources on cylindrical surface and then the study is extended by taking the effect of the element pattern into account.

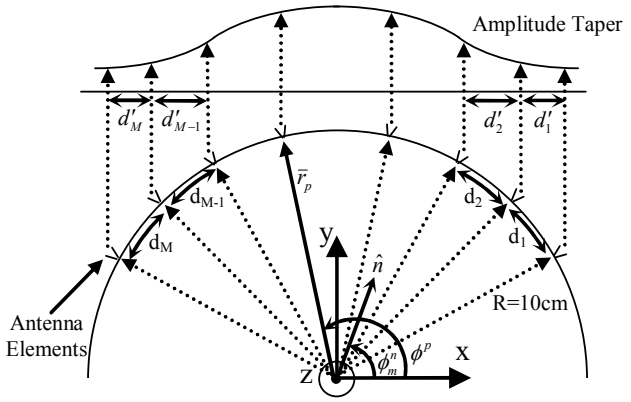

Figure 4.1: Sampling of the Taylor distribution using aperture projection method.

4.1.1. Aperture Projection Method

The aperture projection method is used to determine the excitation of the antenna elements distributed on conformal surface such as cylindrical surface as shown in Figure 4.1. The method is applied by assuming a planar aperture constructed by projecting the antenna element positions onto the planar aperture as shown in Figure 4.1. In the aperture projection, the element weights are determined by the desired amplitude taper such as Taylor distribution, the radiation pattern of which is known. The effect of element pattern and sampling density is taken into account to determine the excitation amplitudes of the slot elements. Before examining the aperture projection method, the pattern synthesis using Taylor line source sampling is examined for planar arrays in terms of uniform and non-uniform sampling.

4.1.1.1. Taylor Line Source Sampling for Planar Arrays

To examine Taylor line source sampling, continuous Taylor line source distribution of length $5\lambda_0$, where λ_0 is the free space wavelength, is assumed on z-axis. Uniform phase distribution is assumed, and hence, the broadside of the radiating source is $\theta = 90°$. The Taylor line source assumed is *-20* dB SLL ($\tilde{n} = 3$) distribution for all the cases as shown in Figure 4.2 (a). The radiation pattern corresponding to the continuous Taylor line source is plotted in Figure 4.2 (b). As it is seen in Figure 4.2 (b), the radiation pattern of the Taylor line source satisfies *-20* dB SLL as expected. Different sampling cases of this distribution are carried out by assuming isotropic elements.

First of all, the Taylor line source is sampled by *100* isotropic elements the positions of which are randomly chosen within the Taylor line source length. A uniform probability density function is used to determine the positions of *100* elements within

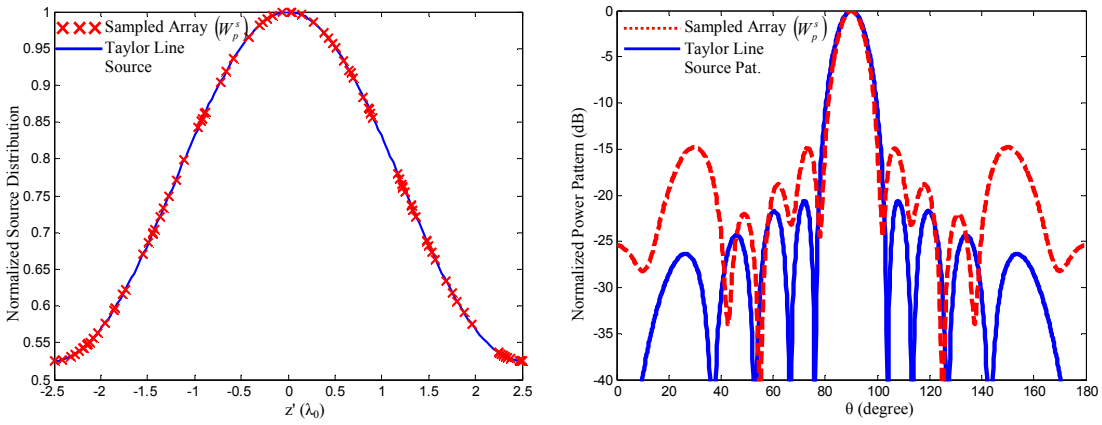

Figure 4.2: (a) Sampling Taylor line source distribution randomly with *100* elements. (b) Corresponding radiation patterns.

the Taylor line source. The weights of the sampled elements, W_p^s are shown by red crosses in Figure 4.2 (a) where p stands for the p^{th} element in the array. The radiation pattern of the sampled array shown in Figure 4.2 (b) indicates that non-uniform sampling has adverse effects on the radiation pattern such that the desired SLL could not be achieved.

Secondly, half of the Taylor line source is sampled randomly by *100* elements starting from $z' = -2.5\ \lambda_0$ till $z' = 0$ as shown in Figure 4.3 (a) and symmetric weights, and hence, symmetric element positions are used for the other half (between $z' = 0$ and $z' = 2.5\ \lambda_0$) resulting in total *200* element array. The corresponding radiation patterns are shown in Figure 4.3 (b). Figure 4.3(b) indicates that randomly sampling half side of the Taylor distribution and using symmetric weights for the other half does not help to obtain desired SLL.

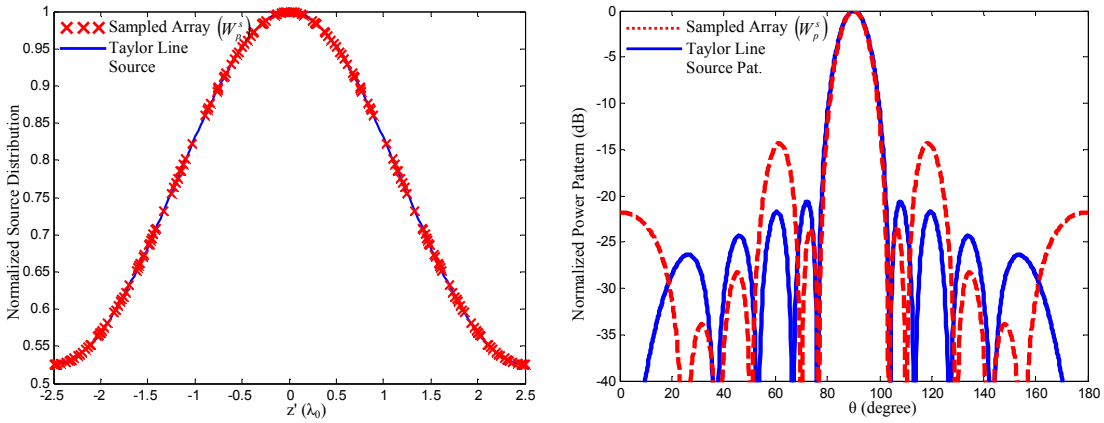

(a) (b)

Figure 4.3: (a) Sampling half side of the Taylor line source distribution randomly and allocating symmetric weights for the other half (Total *200* elements). (b) Corresponding radiation patterns.

In the third case, the Taylor line source is sampled randomly with *1000* elements as shown in Figure 4.4 (a) and the corresponding radiation patterns are plotted in Figure 4.4 (b). As it is seen in Figure 4.4 (b), the radiation pattern of the sampled array gets

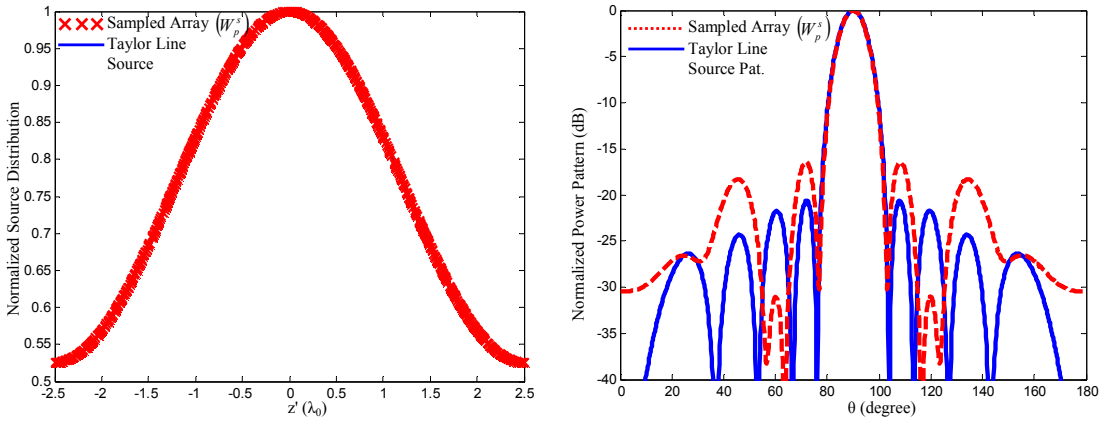

(a) (b)

Figure 4.4: (a) Sampling Taylor line source distribution randomly with 1000 elements. (b) Corresponding radiation patterns.

closer to the ideal Taylor source pattern but there are still side lobes above *-20 dB* even if such a large number of sampling is carried out. In Figure 4.4 (b), the sampling of Taylor line source is carried out many times. The SLL values close to the ideal case are usually obtained. Although, the radiation pattern graph shown in Figure 4.4 (b) is rarely encountered among the trials, it is chosen to indicate that using such kind of large number of elements to sample the Taylor line source distribution might not be enough to satisfy desired SLL and radiation pattern.

Finally, the Taylor line source is uniformly sampled by *11* elements with half a free space wavelength, $\lambda_0/2$, spacing as shown in Figure 4.5 (a). As it is seen in the corresponding radiation patterns presented in Figure 4.5 (b), although the nulls of the array does not coincide with the nulls of the desired radiation pattern, *-20 dB* SLL is satisfied with this uniform sampling. Hence, it can be concluded that non-uniform sampling the Taylor line source has adverse effects on SLL.

In order to examine the effect of the element density, again different cases of sampling the Taylor line distribution are examined. First of all, the Taylor line source

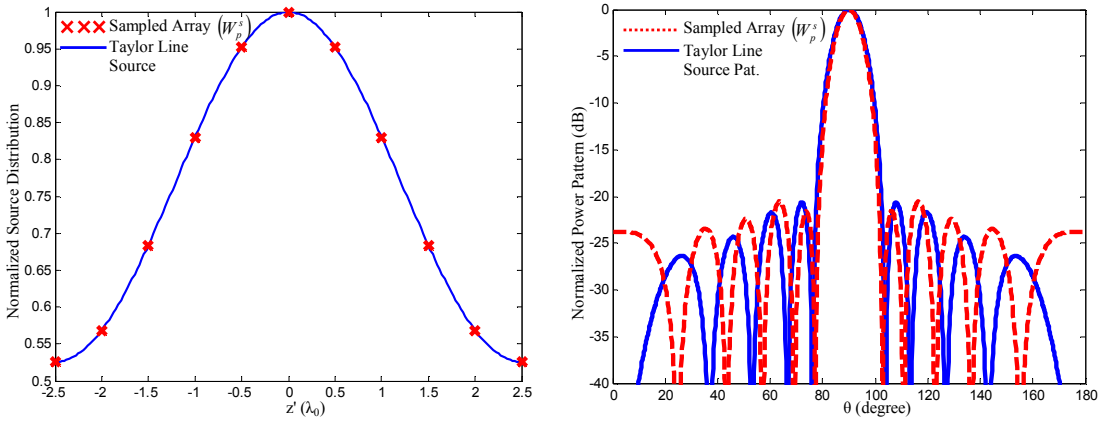

(a) (b)

Figure 4.5: (a) Sampling Taylor line source distribution uniformly with *11* elements. (b) Corresponding radiation patterns.

distribution is sampled again randomly with *100* elements as shown in Figure 4.6 (a). Then the weights of the isotropic antenna elements are determined by altering the sampled the Taylor line source weights with the element density using

$$W_p^D = \frac{W_p^s}{D_p} \tag{4.1}$$

where W_p^s is the weight determined by directly sampling the Taylor line source indicated by red crosses in Figure 4.6 (a). D_p is the element density of the p^{th} element in the array and W_p^D is the weight of the p^{th} element corrected by the element density. The element density is defined as

$$D_p = \begin{cases} \dfrac{2}{d'_p + d'_{p-1}} & p = 2,3,\ldots,M-1 \\ \dfrac{1}{d'_p} & p = 1, M \end{cases} \tag{4.2}$$

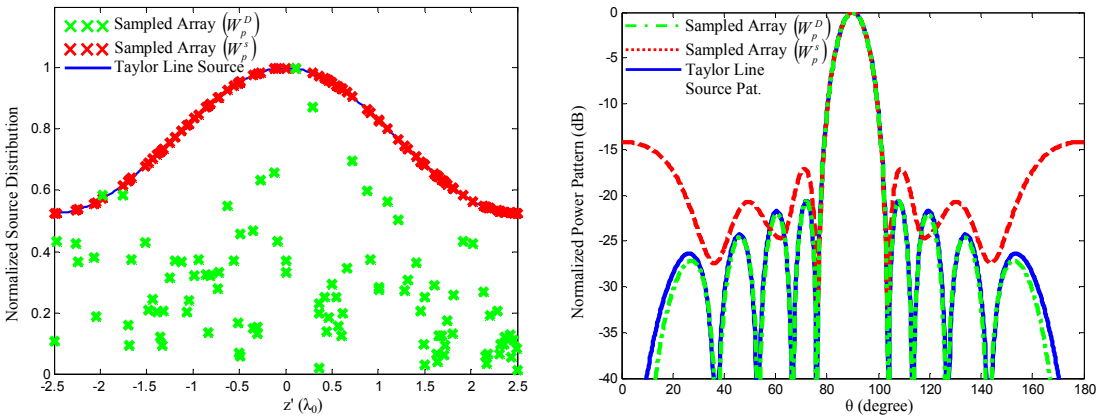

(a) (b)

Figure 4.6: (a) Sampling Taylor line source distribution randomly with *100* elements and adjusting the sampled weights using element density. (b) Corresponding radiation patterns.

where M is the total number of slot elements in the waveguide and d'_p is the element separation of the sampled Taylor line source distribution as shown in Figure 4.1. The weights of the elements corrected by the element density, W_p^D using (4.1), are presented by green crosses in Figure 4.6 (a). As it is seen in Figure 4.6 (a) that the weights are substantially altered by the element density and as a result of this alteration, the expected SLL values can be obtained as shown in Figure 4.6 (b) where the pattern shape of the sampled array is quite close the ideal Taylor line source pattern. Secondly, the Taylor line source is sampled randomly by *20* elements and the element weights are also adjusted using element density as shown in Figure 4.7 (a). The corresponding radiation patterns presented in Figure 4.7 (b) indicates that considering only the element density is not suitable and spacing between some of the elements should not be too large to cause undesired SLL values. When drawing this result, the experiment shown in Figure 4.6 is repeated many times, and each time desired SLL value is reached. This is because the number of elements in Figure 4.6 (a) is high enough so that the element spacing is not too high for some of the elements resulting in high SLL values.

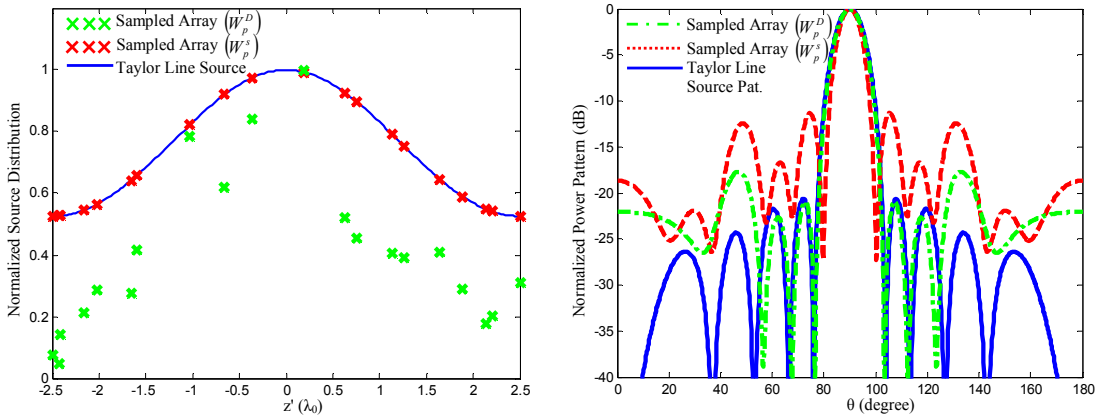

(a) (b)

Figure 4.7: (a) Sampling Taylor line source distribution randomly with *20* elements and adjusting the sampled weights using element density. (b) Corresponding radiation patterns.

4.1.1.2. Taylor Line Source Sampling for Slotted CSIW Array

In this part, the aperture projection method using Taylor line source sampling is examined for the slot arrays placed on cylindrical surface shown in Figure 4.1. Different cases are examined at *25* GHz for *R = 10cm*. The far-field coordinates shown Figure 4.1 are used in the radiation pattern graphs presented in this section. Moreover, only the first half of the radiation patterns are plotted for the region $0° < \phi < 90°$ to enhance the visibility of the patterns plotted on the same graph. The other half in region $90° < \phi < 180°$ can be found by taking the symmetry of the first half with respect to the y-axis. In Figure 4.1, $\hat{n}$ is the normal vector showing the desired main beam direction, ϕ_m^n. $\bar{r}_p$ is the position vector of the p^{th} element in the array. The phase of the p^{th} element in the array is determined as $-k_0 \hat{n}.\bar{r}_p$ where k_0 is the wavenumber in free space, and hence, the element phases are compensated and main beam is directed to ϕ_m^n. In this section, all the element phases are determined so that $\phi_m^n = 90°$.

First of all, *40* slot elements are assumed in order to cover large angular area. Using *40* slot elements equally spaced by $0.7\lambda_g = 0.531\ \lambda_0$, about *142.33°* angular region is covered by the slot elements as shown in Figure 4.8 (a) where λ_g stands for the guided wavelength determined by using the CSIW parameters given in Section 2.1. By using the projected positions of the slot elements, the element positions of the linear array are obtained as shown in Figure 4.8 (a). The element weights for the linear array, W_p^S are found by sampling *-20* dB SLL Taylor ($\tilde{n}=3$) distribution as shown in Figure 4.8 (b). The array factor for the linear array is calculated by assuming isotropic elements and it is compared with the ideal Taylor line source radiation pattern in Figure 4.8 (c). As it is seen in Figure 4.8 (c), the array factor of the linear array deviates from the desired pattern. The weights of the linear array elements are scaled by the element density of the linear array using (4.1) and the

coefficients for the linear array, W_p^D are found. The array factor calculated using the coefficients, W_p^D is seen to successfully mimic the ideal radiation pattern in Figure 4.8 (c). This is an expected result as shown previously in Section 4.1.1.1. Hence, the element density of the linear array is required to be taken into account while finding the element coefficients for the cylindrical slot array.

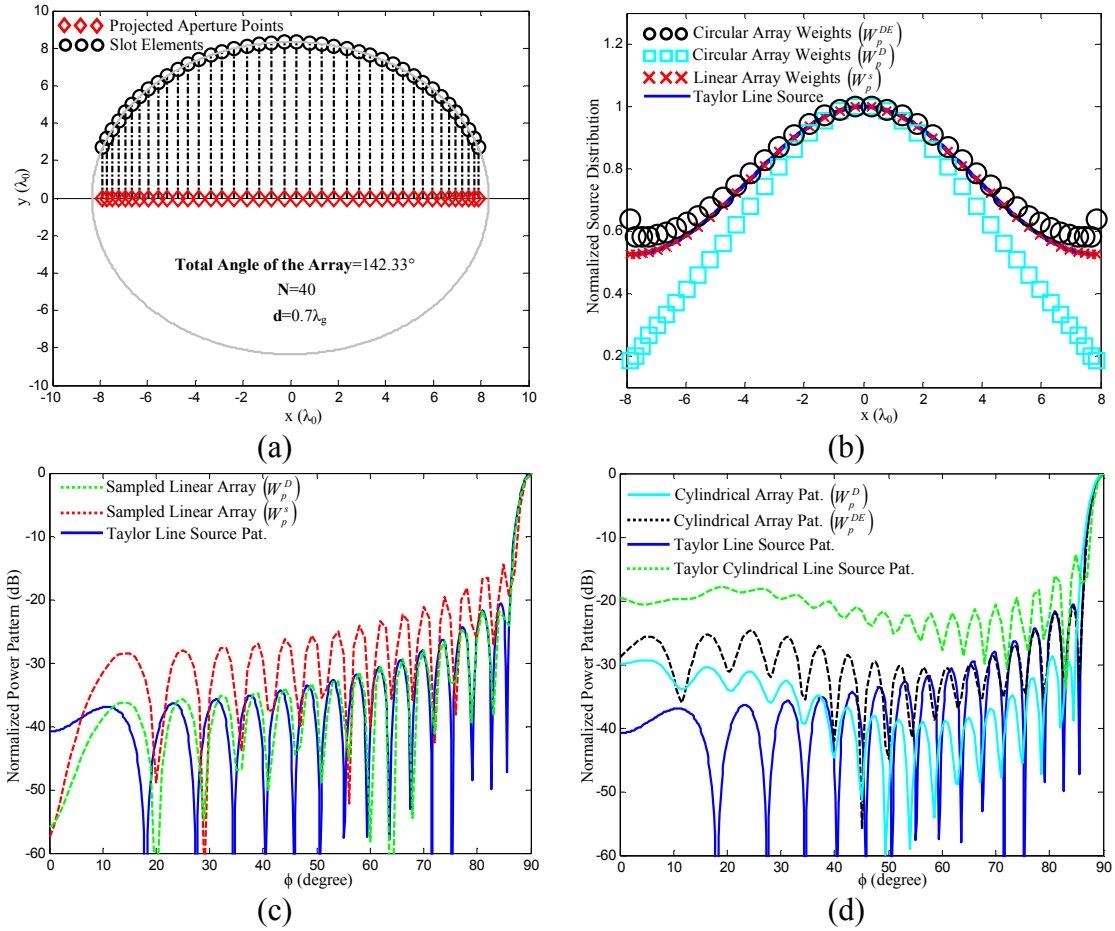

Figure 4.8: (a) Element positions of the slotted CSIW array and element positions at the projected aperture (*40* element array). (b) Sampling Taylor line source distribution using projected aperture positions. (c) Corresponding radiation patterns for linear arrays. (d) Corresponding radiation patterns for cylindrical slot arrays.

The coefficients, W_p^D, are presented by square markers in Figure 4.8 (b) while circle markers in Figure 4.8 (b) shows the element weights for the cylindrical slot array calculated by taking both the element density and element factor into account which is given by

$$W_p^{DE} = \frac{W_p^s}{D_p E_p} \tag{4.3}$$

where E_p is the element pattern of the slot toward the broadside of the array and W_p^{DE} is the excitation coefficient of the p^{th} element scaled by both element density and element factor.

The radiation patterns for the cylindrical slot array are calculated using closed form expressions by assuming that the slot elements have required phases to compensate the phase delays due to different path lengths measured from the position of the slot element to the planar aperture. In the pattern calculations, the effect of element pattern is taken into account. The radiation patterns of the cylindrical slot array are calculated using both of the coefficients, W_p^D and W_p^{DE}. The radiation patterns of the cylindrical slot array are compared with the ideal Taylor line source radiation pattern in Figure 4.8 (d). In Figure 4.8 (d), although there are increased side lobes compared to the ideal Taylor line source radiation pattern due to the slot elements located at the regions close to the beginning and the end of the array, both cases satisfy desired *-20 dB* SLL. To examine the radiation toward the regions close to $\phi = 0°$ and $\phi = 180°$, the same Taylor line source distribution with length equal to the length of the cylindrical slot array is conformed to a cylindrical surface and the radiation pattern of Taylor cylindrical line source pattern is computed. As it is seen in Figure 4.8 (d), the Taylor cylindrical line source pattern has larger side lobes compared to the cylindrical slot array patterns because of conforming the Taylor line source distribution on a cylindrical surface. In Figure 4.8 (d), lower side lobes are obtained

by using the coefficients W_p^D compared to using the coefficients W_p^{DE} for the cylindrical slot array because the coefficients W_p^D looks like the Taylor line source distribution with SLL lower than *-20 dB*. However, the cylindrical slot array pattern with excitation coefficients W_p^{DE} mimics the desired radiation pattern better around the main beam. In Figure 4.8 (b), the increased element density toward edges is compensated by fall off of the element pattern and the element weights, W_p^{DE} does not deviate much from the weights, W_p^s obtained by direct sampling of Taylor line source distribution. So, directly using Taylor weights, W_p^s can be employed for slot array on CSIW with uniform slot separation around the cylinder.

The same analysis using *40* elements and $0.7\lambda_g$ element spacing is carried out using *-30* dB SLL Taylor ($\tilde{n}=3$) and *-40* dB SLL Taylor ($\tilde{n}=6$) distributions. The resultant radiation patterns are presented in Figure 4.9 (a) and (b), respectively. As it is seen in Figure 4.9 (a) and (b), *-35* dB SLL is the limit for *40* element slot array such that

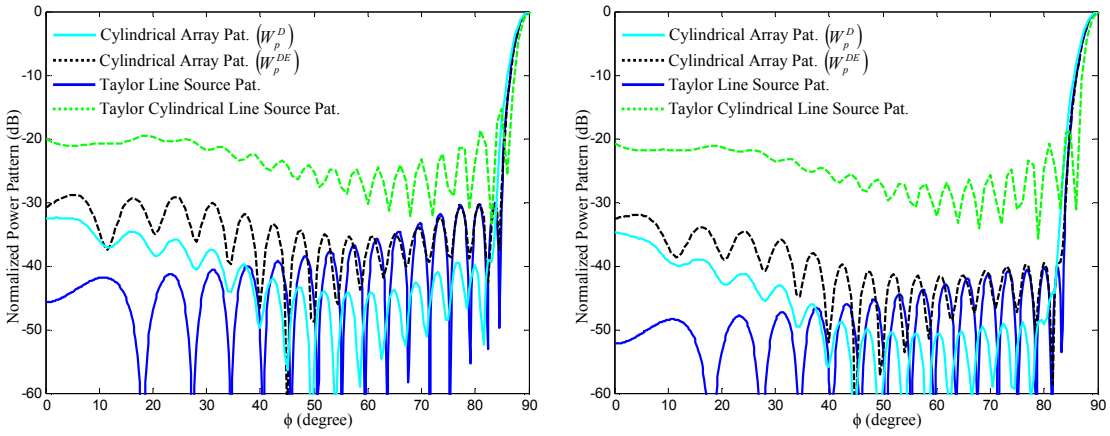

Figure 4.9: (a) Radiation patterns for the slotted CSIW array using (a) *-30 dB* and (b) *-40 dB SLL* Taylor weights.

using *-40 dB* SLL Taylor distribution gives minimum *-34.7 dB* SLL in the radiation patterns. By employing the number of elements less than *40* on radius *R = 10 cm*, the SLL can be reduced below -35 *dB* using *-35 dB* SLL or *-40 dB* SLL Taylor weights.

By considering the directivity requirements, the total angular coverage of the slot elements on CSIW is determined as about *80°*. With this reduced angular coverage compared to the case presented in Figure 4.8, the full wave simulations of the CSIW array is easier to carry out. Moreover, the time in the Elliott's design procedure to determine the slot offsets and lengths are reduced. Using the aperture projection method, the slotted CSIW arrays are designed with non-uniform and uniform slot separation values. First of all, the element spacings are determined to compensate the phases of the cylindrical slot array to get in phase contributions from each element toward the broadside direction and this configuration is achieved by *16* slot elements with about *76°* angular coverage. Hence, non-uniform slot separations are used in this design. Although, the slots are required to be close to the resonance which is easier to design, some of the element spacings are quite far away from $0.7\lambda_g$ which increases the SLL. This design is presented in Section 4.2. The other design allocates *25* slot elements uniformly distributed with $0.7\lambda_g$ spacing which has about *87°* angular coverage as shown in Figure 4.10 (a) and the phase compensation is achieved using slots largely deviating from resonance.

The same analysis as explained in Figure 4.8 is carried out in Figure 4.10 which starts by sampling the *-20 dB* SLL Taylor (ñ=3) line source distribution as shown Figure 4.10 (b). As it is seen in Figure 4.10 (c) and (d), all of the patterns satisfy *-20 dB* SLL criteria. Since the element weights, W_p^{DE} are close to the Taylor line source distribution as mentioned before, *25* element array with uniform slot separations on CSIW is decided to be designed in the Elliot's code with element weights, W_p^{DE}. The design of this array is presented in Section 4.3.

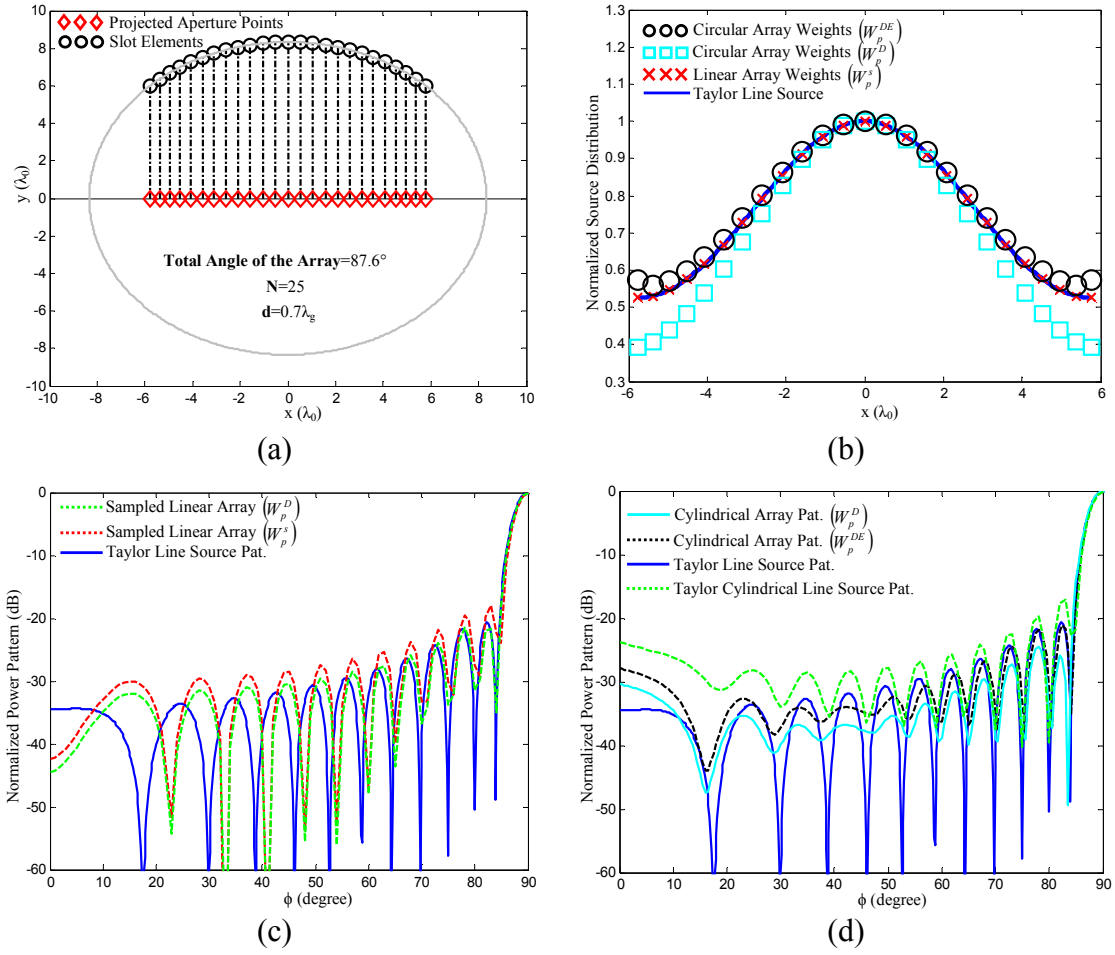

Figure 4.10: (a) Element positions of the slotted CSIW array and element positions at the projected aperture (*25* element array). (b) Sampling Taylor line source distribution using projected aperture positions. (c) Corresponding radiation patterns for linear array. (d) Corresponding radiation patterns for cylindrical slot array.

4.2. Slot Array Design on CSIW with Non-Uniform Slot Separation

The design of *1 x 16* element longitudinal slot array on CSIW is carried out at *25 GHz* for radius, *R = 10 cm*. The schematic view of the slotted CSIW array used in the simulations is shown in Figure 1.2. The slotted CSIW array is formed using the CSIW and substrate parameters mentioned in Section 2.1. The slot width is chosen as $w^s = 0.25\ mm$. The aim of this design is to develop a proof-of-a-concept prototype to demonstrate a frequency scanning with circumferential slot array on CSIW. Hence, a directivity of the radiation pattern should be high to observe the rotation of the beam clearly. Moreover, the SLL is desired to be low. Hence, the excitation amplitudes of the slot elements, W_p^s are determined by sampling *-20 dB* SLL Taylor ($\tilde{n} = 3$) distribution as shown in Figure 4.1. Distances between the slots (d_p, $p = 1, 2, .., 15$) shown in Figure 4.1 are determined to obtain the slot element phases such that in phase contribution from each element is achieved and directive main beam is obtained in $\hat{a}_y$-direction. Without compensating the phases of the elements and using uniform element spacing, larger HPBW values can be obtained by using *-40 dB SLL* Taylor (ñ = 3) distribution [52], however, the frequency steering might not be clearly observed with such a high HPBW values especially when the narrow bandwidth of the slotted waveguide array is considered. In the schematic view of *1 x 16* slot array on CSIW shown Figure 1.2 which is used in the simulations, the array is excited from Port 1, i.e., the traveling wave propagates in $-\hat{a}_\phi$-direction, and Port 2 is terminated by a matched load. The same convention used in Figure 4.1 such that the traveling wave propagates in $-\hat{a}_\phi$-direction and the first element having separation d_1 in Figure 4.1 is the one closest to the matched load. The only difference between Figure 4.1 and *1 x 16* slot array simulations is that the broadside of the array in Figure 4.1 is in $\hat{a}_y$-direction while the broadside of *1 x 16* slot array is located at $\phi = 48°$ in the simulations. This difference is caused by locating the first slot element at $\phi = 4.57°$ after designing the array using the convention presented in Figure 4.1, and hence, the last slot element position coincides at $\phi = 80.57°$ in the simulations.

The phase compensation procedure, i.e, determining the slot separation values, is carried out using three different slot alternation schemes. In the first case, all the slots are located at the same half side of the CSIW, i.e., the slots are not alternated. In the second case, slots are alternated sequentially as shown in Figure 1.2 (b). In the third case, some of the slots are alternated and some of them are not alternated with respect the previous slot. In the third case, the alternation of the p^{th} slot is determined by the aim that gives minimum d_{p-1} value, i.e., d_{p-1} values are calculated by altering and not altering the p^{th} slot and alternation is decided if it gives minimum slot separation d_{p-1}. Hence, three set of slot separations are obtained and plotted in Figure 4.11 (a). For all three cases, there is minimum allowed slot separation value. If some of the element separations are below the minimum limit, high mutual coupling levels do not allow making the Elliott's design. The minimum allowed slot separation value is determined by iteratively decreasing the minimum allowed slot separation value and applying the Elliott's design procedure till the Elliott's design procedure cannot be achieved due to high mutual couplings. The minimum allowed slot separation value is found to be nearly the same for all three cases.

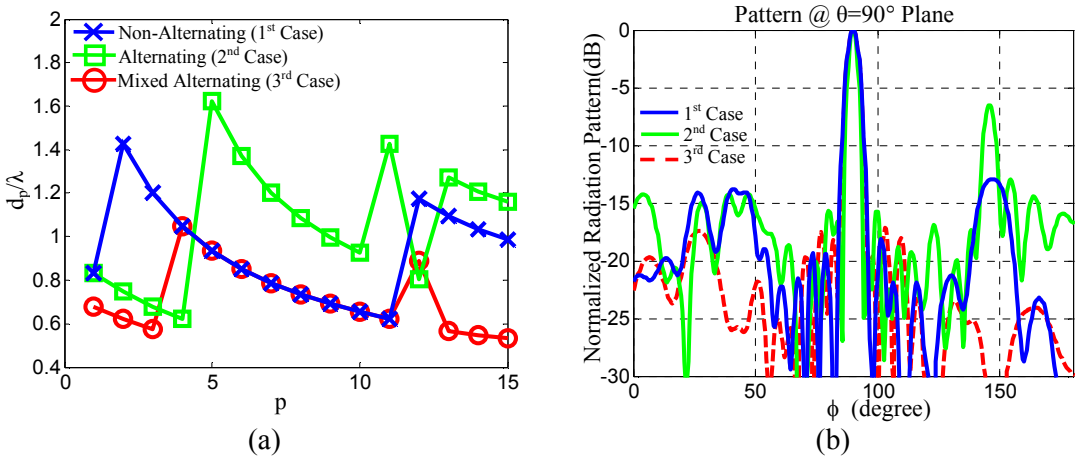

Figure 4.11: (a) Element spacing and (b) calculated patterns of *1 x 16* slot array on CSIW (*R = 10 cm*) for three different slot separation schemes.

An in-house code is developed that calculates the far-field pattern of slot array on cylindrical surface. The slot elements are assumed to be tangentially placed on the cylindrical surface and the element factors are also taken into account. The patterns of *1 x 16* slot array for three different slot separation cases are calculated and plotted as shown in Figure 4.11 (b). The radiation patterns are plotted at $\theta = 90°$ plane with respect to the coordinate system indicated in Figure 4.1. The patterns show about *5°* HPBW which is enough to observe the frequency scanning. Although, *-20 dB* SLL Taylor ($\tilde{n} = 3$) distribution is used to determine the weights of the elements, *-20 dB* SLL could not be obtained in the radiation pattern graphs in Figure 4.11 (b) in all three cases, because the Taylor distribution is not sampled dense enough and because of large slot separation values obtained after compensating the element phases as described in Section 4.1.1. As it can be seen in Figure 4.11 (a), the minimum value for the average of the slot separations is obtained for the third case which provides lowest SLL values in Figure 4.11 (b). Hence, the slot separation values in the third case are decided to be used in the further design steps and the fabrication.

The propagation constant and the characterization polynomials derived for the CSIW is used together with the slot separation values for the third case in the Elliott design procedure described in Section 3.2. The Elliott's design procedure is modified to be used with different slot separation values. In Chapter 2, it is observed that the shunt admittance model is not affected much by the radius of the curvature and almost no difference between the planar SIW and CSIW is observed for $R = 10\ cm$. Moreover, almost no difference is observed between the radius $R = 10\ cm$ ($8.33\lambda_0$ *at 25 GHz*) and planar case in terms of mutual couplings in Section 3.3 and in [53]. Hence, the active admittance formulations derived for the planar case given in [34] and [36] are used in the Elliott's design procedure. The Elliott's design procedure is implemented in MATLAB to determine the slot offsets and lengths of the slot array on CSIW.

In the Elliott's design, the slot offsets and lengths which satisfy desired complex slot voltages are determined. The Elliott's design procedure is a complicated routine such

that the pattern requirements, i.e., the complex slot voltages, are required to be satisfied together with a good input match. In the planar case, usually the slot separations are changed if the required input match is not obtained, however, slot separations affect the phase compensation and it is required to obtain directive main beam in slotted CSIW array. The value of the first slot element can be varied to improve the input match, however, the first slot offset determines the power delivered to load as mentioned in Section 3.2. The other parameters which can be changed to improve the input match are the slot separation values or number of elements used in the slotted CSIW array. In the design, the number of elements can be changed or minimum allowed slot separation value might be increased and phase compensation can be reapplied till obtaining a good input match in the Elliott's design procedure. Increasing the number of elements or slot separations might increase SLL.

In the Elliott's design procedure, a *1 x 16* slot array on CSIW (*R = 10 cm*) with separation values determined by the third case given in Figure 4.11 (a) is considered and the slot offsets and lengths are determined at *25 GHz*. The calculated slot offset and length values are tabulated in Table 4.1. Since there is no input match problem encountered in the Elliott's design procedure, the slot separations or number of elements are not changed to improve input match as mentioned previously. The array designed by Elliott's design procedure is simulated in HFSS without microstrip

Table 4.1: Slot offsets and lengths of *1 x 16* slot array on CSIW determined by Elliott's design procedure.

Element #	**1**	**2**	**3**	**4**	**5**	**6**	**7**	**8**
Slot Offsets (mm)	-0.250	-0.290	-0.176	-0.164	-0.161	0.223	0.232	0.204
Slot Lengths (mm)	4.012	4.066	4.006	3.954	3.939	4.009	3.986	3.960
Element #	**9**	**10**	**11**	**12**	**13**	**14**	**15**	**16**
Slot Offsets (mm)	0.179	0.164	0.153	0.118	0.078	0.058	-0.087	0.055
Slot Lengths (mm)	3.953	3.952	3.953	3.956	3.906	3.908	3.924	3.932

transitions to compare with the Elliott's design code implemented in MATLAB. The simulation results are shown in Figure 4.12. In the Elliott's design, the power delivered to load at *25 GHz* is calculated as *9.1 %* and S_{11} value at *25 GHz* is found as *-18.05 dB*. The simulated results of the array show about *-19.7 dB* S_{11} value at *25 GHz* which is in a quite good agreement with the Elliott's design code. The simulated value of S_{21} is *-9.59 dB* at *25 GHz* which indicates that *11 %* of the power is delivered to load. In the Elliott's design code, the power delivered to load is found as *9.1 %* which shows the validity of the Elliott's design procedure implemented in a MATLAB code. Small difference between the results can be caused due to the loss tangent of the substrate not taken into account in the Elliott's design procedure.

The simulated radiation patterns of the *1 x 16* slot array designed by Elliott's design procedure is plotted between *24 GHz* and *26 GHz* as shown in Figure 4.13 (a). As it is seen in Figure 4.13 (a), about *10°* beam steering is obtained when the frequency is steered between *24-26 GHz* band. Note that the main beam is directed to $\phi = 48°$ at *25 GHz* which is different from the pattern given in Figure 4.11 (b) as stated before. The SLL around *-16 dB* is obtained at *25 GHz* both in the simulated patterns shown in Figure 4.13 (a) and in the patterns calculated by closed form expressions given in

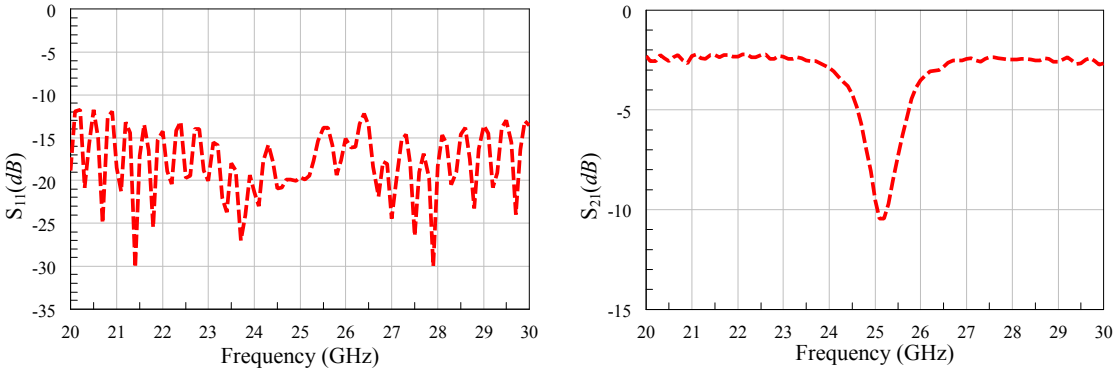

Figure 4.12: (a) S_{11} and (b) S_{21} results of *1 x 16* SIW slot array on CSIW designed by Elliott's design procedure.

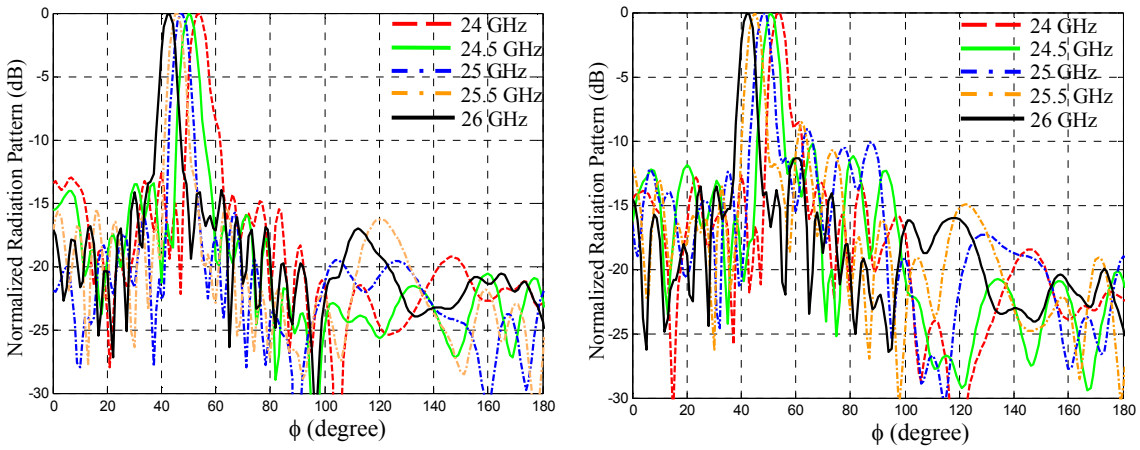

Figure 4.13: Simulated radiation patterns of *1 x 16* arrays (a) designed using Elliott's design procedure and (b) optimized array.

Figure 4.11 (b). In Figure 4.13 (a), the SLL increases to about *-13 dB* as a result of frequency steering. Desired *-20 dB* SLL is not obtained because of large element spacing as stated before. The simulation results of the accepted power and radiation efficiency of the slotted CSIW array designed by Elliott's design procedure are presented in Figure 4.14. The accepted power is calculated by subtracting the sum of reflected power and the power absorbed at the matched load from the power incident to the slot array. It can be seen in Figure 4.14, about *88 %* power is accepted around *25 GHz*. Part of the accepted power is radiated and the other part is dissipated as dielectric and conductor losses. Due to these losses, the efficiency of *1 x 16* slot array reduces to *55 %* at *25 GHz*.

In order to increase the bandwidth of the *1 x 16* slot array for beam steering applications, the slot lengths shown in Table 4.1 are optimized in Ansys HFSS to increase the radiated power, and hence, the efficiency. The sequential nonlinear programming optimization in Ansys HFSS is carried out to maximize the accepted power of the array between *24 GHz* and *26 GHz* in the simulations. The accepted

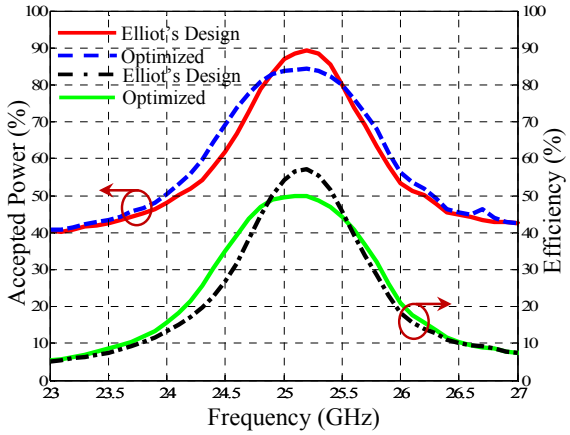

Figure 4.14: Comparison of the accepted powers and efficiencies of two *1 x 16* array on CSIW (*R = 10 cm*).

power is used in the optimizations because fast frequency sweeps can be used to calculate the accepted power in Ansys HFSS which is faster compared to the calculating and saving the fields radiated by the antenna at each frequency step and then calculating the radiated power. As a result of the optimizations, about *200 MHz* increase is obtained in the *70 %* accepted power bandwidth as shown in Figure 4.14. The slot offsets and lengths found after the optimizations are presented Table 4.2. As it is seen in Table 4.2, the slot offsets are not changed compared to the values given in Table 4.1 because only the slot lengths are optimized. After the optimizations, the efficiency values of the array are calculated and presented in Figure 4.14. As it is seen in Figure 4.14, the efficiency bandwidth also increases as a result of increasing the accepted power bandwidth. The simulated radiation patterns of the optimized *1 x 16* slot array are shown in Figure 4.13 (b). The band of the slot array is increased at the expense of increased SLL. As it is seen in Figure 4.13 (b), the SLL is increased to about *-10 dB* compared to the patterns before the optimization presented in Figure 4.13 (a).

Table 4.2: Slot offsets and lengths determined after the optimization of *1 x 16* slot array on CSIW designed by Elliott's design procedure.

Element #	**1**	**2**	**3**	**4**	**5**	**6**	**7**	**8**
Slot Offset (mm)	-0.250	-0.290	-0.176	-0.164	-0.161	0.223	0.232	0.204
Slot Length (mm)	3.941	4.047	3.956	4.154	3.900	4.040	4.122	3.890
Element #	**9**	**10**	**11**	**12**	**13**	**14**	**15**	**16**
Slot Offset (mm)	0.179	0.164	0.153	0.118	0.078	0.058	-0.087	0.055
Slot Length (mm)	3.997	4.138	3.829	3.909	3.989	4.103	4.119	3.801

The efficiency calculations are also carried out by setting both dielectric and conductor losses to zero in the optimized *1 x 16* slot array antenna simulations. The efficiency results are compared with the results obtained by simulations where all the losses are taken into account in Table 4.3. As it is seen in Table 4.3, the efficiency of the optimized array is below *50 %* because of high dielectric and conductor losses of large SIW array at K band.

Table 4.3: Comparison of the simulated efficiency values of optimized *1 x 16* slot array on CSIW

Frequency	**Lossy**	**Lossless**
24 GHz	15.7 %	22.0 %
24.5 GHz	34.9 %	53.9 %
25 GHz	49.6 %	79.2 %
25.5 GHz	44.3 %	70.5 %
26 GHz	21.0 %	29.3 %

4.2.1. Fabrication and Measurements

The optimized *1 x 16* slot array is selected to be fabricated. Moreover, *4 x 16* slot array on CSIW is formed and fabricated by using *1 x 16* optimized slot arrays connected using a *1 x 4* SIW power divider. The fabrication of the slot arrays are carried out in in-house facilities by using standard PCB process. SIW structures are formed by via hole plating process. The fabrications are carried out using *0.5 mm* thick Rogers *3003* substrate. The substrate has *35 μm* thick copper cladding on both sides. First of all, via holes are drilled which is followed by electroplating process for about *2* hours to coat the walls of drilled holes with copper. Then microstrip lines and slots are formed by stripping the excess copper using PCB milling.

4.2.1.1. 1 x 16 Optimized Slot Array on CSIW

The optimized *1 x 16* slot array with parameters indicated in Table 4.2 is fabricated and it is shown in Figure 4.15 (a). The structure is measured and the s-parameters are compared with the simulations in Figure 4.15 (b) and (c). In Figure 4.15 (b) and (c), very good agreement between the measured and simulated results is obtained. The matching of the structure is below *-10 dB* between *20 GHz* and *30 GHz*. The measured and simulated S_{11} value at *25 GHz* is about *-20 dB*. S_{21} values at *25 GHz* are *-8.15 dB* and *-10.3 dB* for the simulations and measurements, respectively. Hence, the power delivered to load is calculated as about *15.3 %* for the simulations and *9.3 %* for the measurements at *25 GHz*. Using the loss values calculated for the transition and SIW parts without slots in Section 2.2 and also using the measured s-parameters shown in Figure 4.15 (b) and (c), the radiated power of the antenna can be roughly calculated by ignoring the effect of slots at *25 GHz*. The radiated power is calculated as around *40 %* of the input power, i.e., the efficiency of the antenna is expected to be around *40 %* at *25 GHz*.

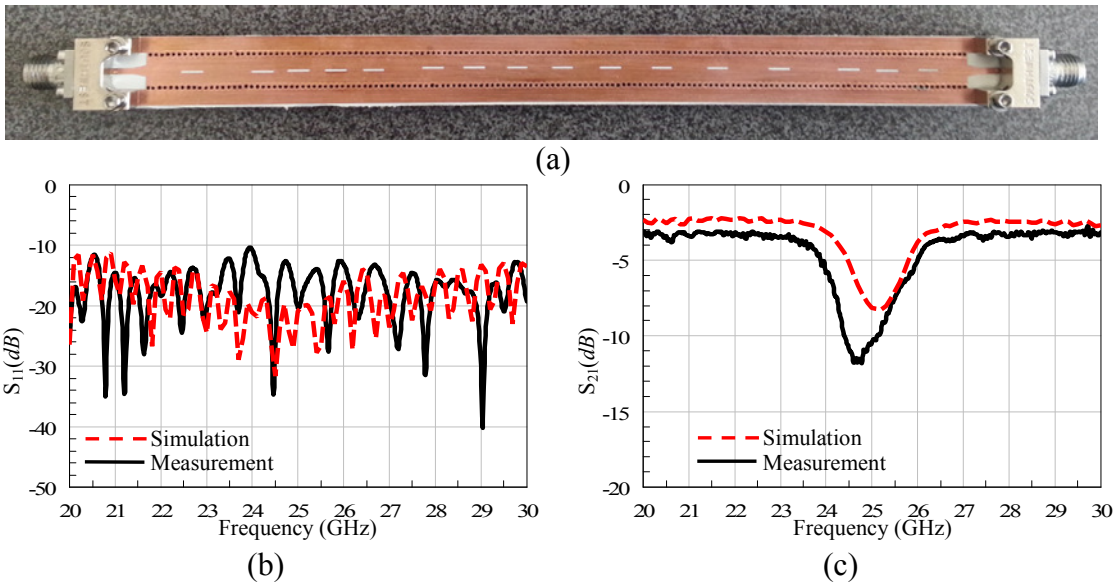

Figure 4.15: (a) Fabricated traveling wave optimized *1 x 16* slot array on SIW. (b) S_{11} and (c) S_{21} results of the optimized *1 x 16* slotted SIW array.

The radiation patterns and the gain of the antenna are measured in an anechoic chamber using the measurement setup shown in Figure 4.16. The radiation pattern measurements are taken with *1°* resolution in the H-plane. The H-plane pattern

Figure 4.16: Measurement setup of *1 x 16* slot array on CSIW (*R = 10 cm*).

measurements are taken between *24 GHz* and *26 GHz* with *0.5 GHz* steps and the measured patterns are compared with the simulated results in Figure 4.17. In Figure 4.17 (a) - (e), the measured radiation patterns between *24 GHz* and *26 GHz* are compared with the simulation results. Good agreement between the simulated and measured data is obtained around the main beam.

In Figure 4.17 (a)-(e), some of the measured side lobes are seen to be deviating from the simulations. This deviation might be due to some fabrication imperfections. For example, the difference between the slot offset values required to be satisfied is too small as shown in Table 4.2 which might not accurately be satisfied in PCB milling process. Moreover, the substrate is heated in the electroplated step which causes substrate to expand which causes a stress on the substrate. In addition to the substrate stress, the stress level of the copper changes after the electroplating process which cause misalignment problems encountered between drill and the milling layers in the fabrication. This misalignment can easily affect values of the slot offsets required to be satisfied.

In Figure 4.17 (f), the main beam positions of the measured radiation patterns are compared with the simulations to observe the frequency steering. As it is seen in Figure 4.17 (f), about *10°* beam steering is observed as a result of frequency scanning between *24 GHz* and *26 GHz*. The maximum deviation of the measured beam positions from the simulated data is about *1°* for each measurement frequency. *1°* error in the main beam positions is an expected result when it is considered that the measurements are taken with *1°* angular resolution.

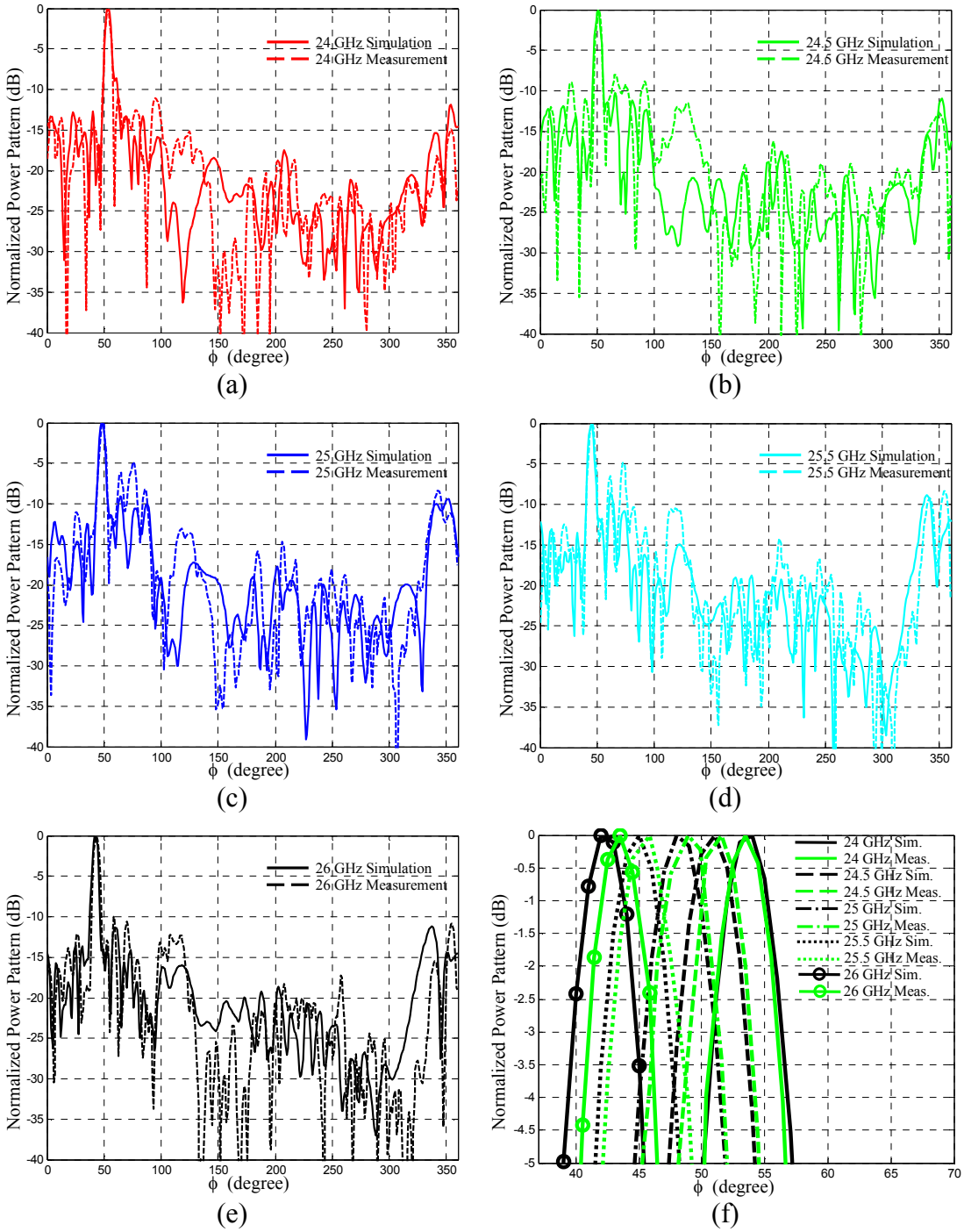

Figure 4.17: Radiation patterns of *1 x 16* slot array on CSIW.

The HPBW values are computed by interpolating the simulated and measured H-plane patterns originally generated by *1°* angular resolution and then calculating the HPBW numerically. The measured HPBW and cross-polarization values are compared with the simulations in Table 4.4. As it is seen in Table 4.4, there is a very good agreement between the simulated and measured results.

Table 4.4: Simulated and measured HPBW and cross-polarization values of *1 x 16* slot array on CSIW.

	HPBW		**Cross-pol.**	
Frequency	**Meas.**	**Sim.**	**Meas.**	**Sim.**
24 GHz	5°	5°	-20.63 dB	-19.65 dB
24.5 GHz	5.36°	5.18°	-20.13 dB	-23.00 dB
25 GHz	5.19°	5.59°	-20.21 dB	-22.81 dB
25.5 GHz	4.85°	5.36°	-17.37 dB	-22.72 dB
26 GHz	5.15°	5.47°	-13.46 dB	-18.65 dB

The gain of the array is measured using the standard gain horn antenna. The measured gain and efficiency values are compared with the simulations in Figure 4.18. Since there is a good agreement between the measured radiation patterns and the simulations in Figure 4.17, the directivity values in the simulations are used to calculate the measured efficiency values. About *11.8 dB* gain is obtained at *25 GHz* in the simulations while the measured gain is about *11.58* dB which is quite close to the simulated gain. The behaviors of the simulations and measurements are the same and there is maximum about *2.5 dB* difference between measured and simulated gain values at *24 GHz*. The efficiency of the antenna is expected as *40 %* at *25 GHz* using measured s-parameters at the beginning of Section 4.2.1.1, and it is found around *45 %* in the simulations and the measurements which is quite close to the expected value.

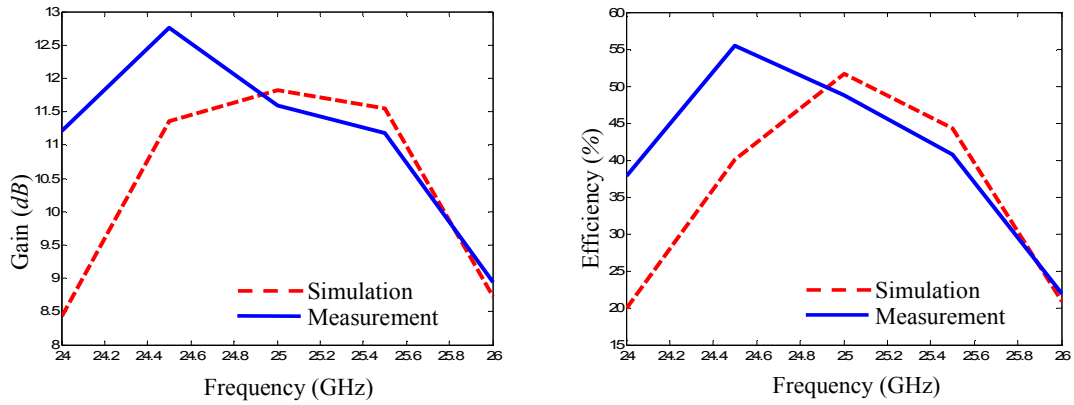

(a) (b)

Figure 4.18: (a) Gain and (b) efficiency results of *1 x 16* SIW slot array.

4.2.1.2. 1 x 4 SIW Power Divider

A *1 x 4* SIW power divider structure is designed and fabricated to feed *4 x 16* CSIW slot array. Two power dividers are connected back to back and fabricated. The picture of the fabricated power divider is shown in Figure 4.19 (a). T-junction structure presented in [5] is used to obtain *1 x 2* power division. Then H-plane Y-junctions are implemented to obtain *1 x 4* power division. Additional vias are implemented at two sides of the Y-junction to have equal power division in the simulations. The power divider is fed by optimized microstrip line to SIW transition with $L_f = 7.5\ mm$. The other transition, substrate and via parameters are the same as the ones listed in Section 2.1 and Section 2.2. The positions and the diameters of three vias at each side of the power divider shown in Figure 4.19 (a) are optimized in Ansys HFSS to have a good transition between *24 GHz* and *26 GHz*.

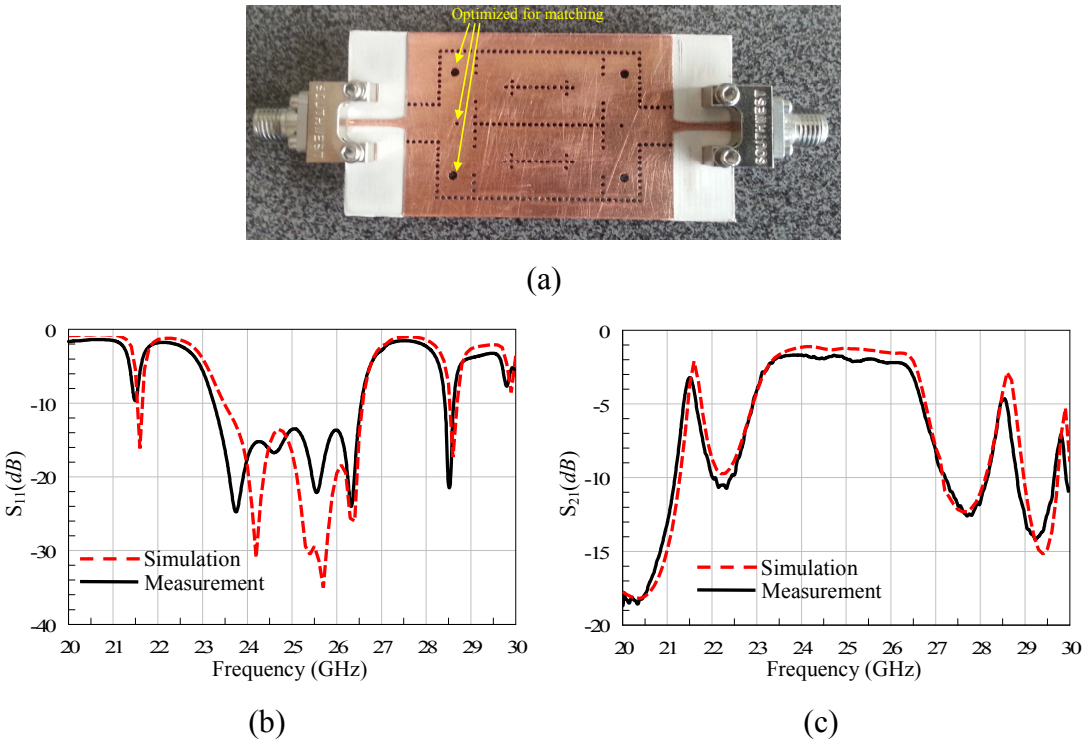

Figure 4.19: (a) Fabricated two back to back *1 x 4* power dividers. (b) S_{11} and (c) S_{21} results of the back to back power divider structure.

The measured s-parameters of the power divider structure are compared with the simulated results in Figure 4.19 (b) and (c). A good agreement between simulation and measurement results is obtained. Input matching of the power divider is better than *-10 dB* and insertion loss is about *2 dB* between *24 GHz* and *26 GHz* band. The transition structures as shown in Figure 2.3 with $L_f = 7.5\ mm$ are also manufactured for different SIW lengths and the transition loss in the power divider is measured as *0.56 dB* at *25 GHz* for one sided transition. Considering *1.92 dB* insertion loss of the power divider structure at *25 GHz* shown Figure 4.19 (a) and using *0.56 dB* loss due to the transition, the insertion loss of only the SIW part of back to back power divider structure can be calculated as *0.8 dB*. Hence, the insertion loss in the SIW part of one sided power divider structure is *0.4 dB*. Although *1.92 dB* insertion loss is good enough for most of the applications, the losses due to the transition to SIW can be

reduced by using shorter feed lines and/or by using CPW feed line which has lower radiation losses or by using aperture coupled feeding of the SIW by another waveguide which does not have radiation losses. In *4 x 16* slot array structure, a shorter transition with $L_f = 4\ mm$ is used to reduce the loss and also to avoid the microstrip cracks which occur while bending the antenna.

4.2.1.3. 4 x 16 Slot Array on CSIW

The fabricated traveling wave *4 x 16* slot array is shown in Figure 4.20. The array is composed of microstrip line to SIW transition mentioned in Section 2.2, *1 x 16* slot array optimized as described in Section 4.2, and *1 x 4* SIW power divider structure mentioned in Section 4.2.1.2. Total length of the array is *19.82 cm*. If the transition parts with lengths $L_f = 4\ mm$ and $L_t = 2.1\ mm$ are excluded from the structure the length of SIW region in the *4 x 16* array is found as *18.6 cm*.

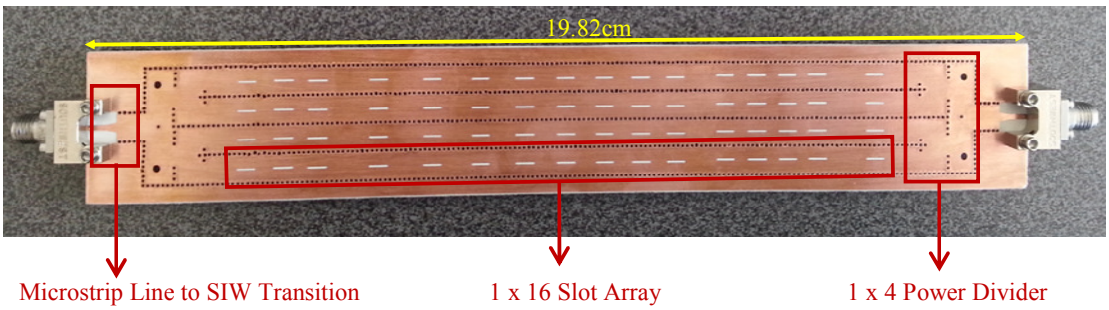

Figure 4.20: Fabricated traveling wave *4 x 16* slot array on SIW.

The s-parameters of the fabricated *4 x 16* slot array are measured and compared with the simulations in Figure 4.21. The simulations of *4 x 16* CSIW array are carried out

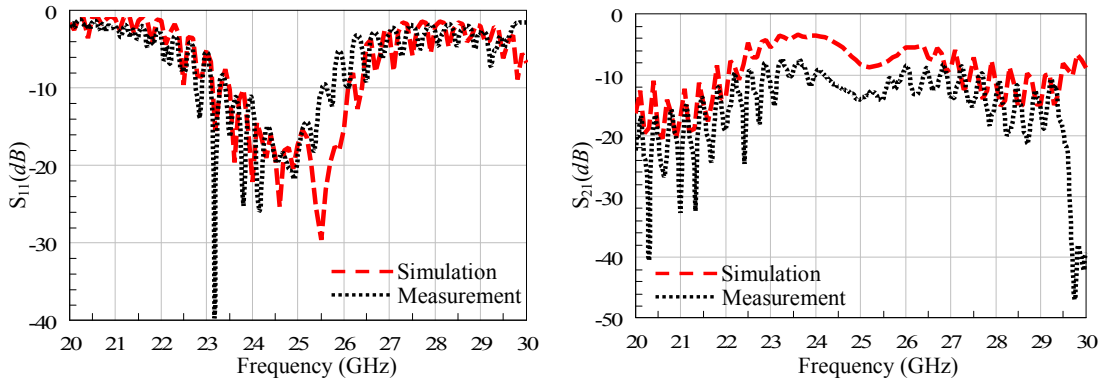

(a) (b)

Figure 4.21: (a) S_{11} and (b) S_{21} results of *4 x 16* SIW slot array.

by taking the effect of connectors into account. Good agreement between the simulations and measurements are obtained except about *5 dB* difference in S_{21} values between *24 GHz* and *25.5 GHz*. The reason for the discrepancy between the S_{21} values are searched by conducting some experiments on SIW (without slots) pieces and microstrip lines fabricated on the same material. During the measurements, non-uniform manufacturing of the devices are observed between the same types of samples from the same production cycle. It is observed that there is a good agreement between the measured and simulated S_{21} values of microstrip lines. On the other hand, *1-2 dB* differences are observed in the S_{21} values of SIW transitions. It is predicted that these additional losses observed in the measurements are due to the fabrication imperfections.

The radiation patterns of the fabricated array are measured in an anechoic in the H-plane using the measurement setup shown in Figure 4.22. The radiation patterns of the array are measured by *1°* angular resolution between *24 GHz* and *26 GHz* band with *0.5 GHz* steps. The measured patterns are compared with the simulations in Figure 4.23. In Figure 4.23 (a)-(e), the simulated and measured patterns are compared between *24 GHz* and *26 GHz* with *0.5 GHz* steps. It can be seen in

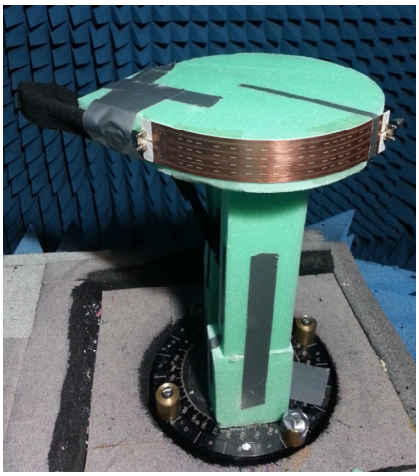

Figure 4.22: Measurement setup of *4 x 16* slot array on CSIW (*R = 10 cm*).

Figure 4.23 (a)-(e) that measured patterns are in a very good agreement with the simulations. Better agreement between the measured and simulated SLL values is obtained compared to *1 x 16* slot array patterns shown in Figure 4.17. Small discrepancies in SLL values might be caused by small errors in the placement of the array on foam cylinder which is quite flexible material. Moreover, it is inevitable to have rough surface while cutting the foam to make a cylindrical surface.

In order to observe the amount of frequency steering, the measured main beam positions are compared with the simulations in Figure 4.23 (f). As it is seen in Figure 4.23 (f), about *10°* beam steering is observed as a result of frequency scanning between *24 GHz* and *26 GHz*. There is about *1°* maximum error observed at *24 GHz*. This is a good result when the measurements taken with *1°* angular steps are concerned. The cross polarization levels and HPBW values of the patterns are also measured and compared with the simulations in Table 4.5. Good agreement between the measured and simulated cross polarization levels is obtained. The HPBW values are calculated by interpolating the measured and simulated radiation patterns and they are also in a good agreement with each other as shown in Table 4.5.

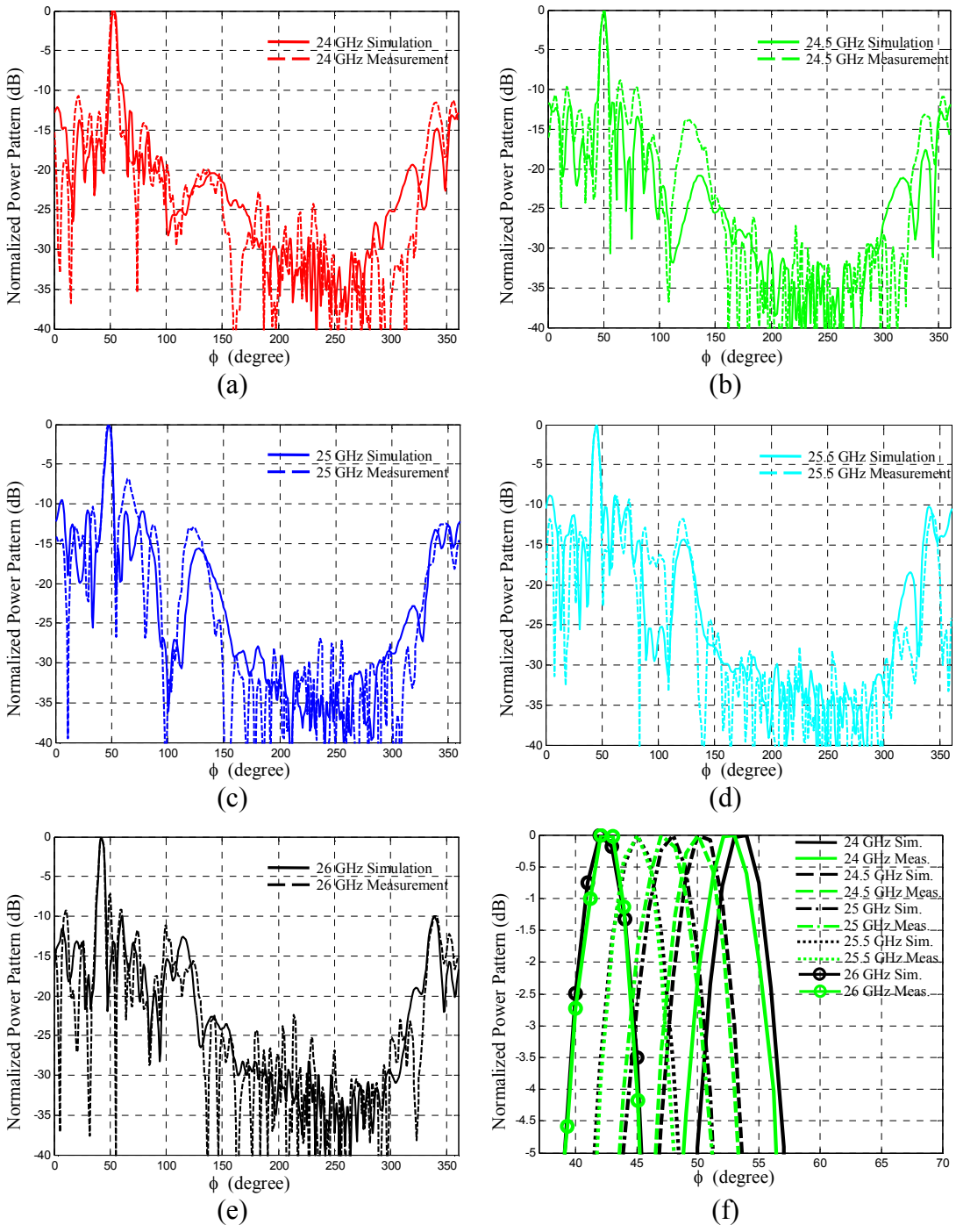

Figure 4.23: Radiation patterns of *4 x 16* slot array on CSIW.

Table 4.5: Simulated and measured HPBW and cross-polarization values of *4 x 16* slot array on CSIW.

	HPBW		Cross-pol.	
Frequency	**Meas.**	**Sim.**	**Meas.**	**Sim.**
24 GHz	5.92°	5.49°	-21.56 dB	-18.48 dB
24.5 GHz	5.39°	5.34°	-23.44 dB	-24.84 dB
25 GHz	5.79°	5.75°	-24.23 dB	-23.90 dB
25.5 GHz	4.91°	5.36°	-23.36 dB	-23.35 dB
26 GHz	4.77°	4.96°	-17.51 dB	-20.57 dB

The gain of the array is measured for different frequencies using the standard gain horn antenna. The measured gain and efficiency values of *4 x 16* slot array on CSIW are compared with the simulations in Figure 4.24. Since there is a good agreement between the measured radiation patterns and the simulations in Figure 4.23, the directivity values in the simulations are used to calculate the measured efficiency values. About *16 dB* gain is obtained at *25 GHz* in the simulations while the measured gain is about *14.5 dB*. There is about maximum *2.5 dB* deviation between measured and simulated gain values at *26 GHz*. As it is seen in Figure 4.24, the

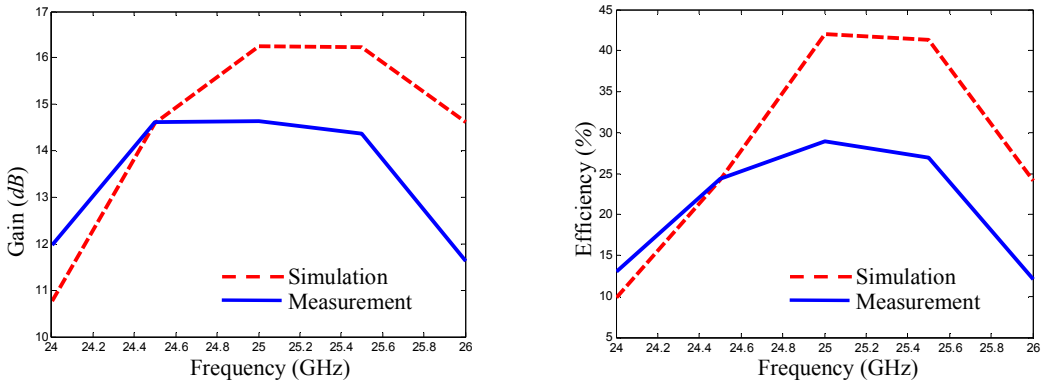

(a) (b)

Figure 4.24: (a) Gain and (b) efficiency results of *4 x 16* SIW slot array.

measured and simulated data is consistent. The dielectric and conductor losses cause degradation in the efficiency values which is proved in the results presented in Table 4.3. The differences between the simulations and measurements in the gain and efficiency values are due to the fabrication imperfections. The fabrication imperfections may cause a considerable degradation in the performance of the structure designed at such high frequency applications which require high precision in the fabrication.

4.3. Slot Array Design on CSIW with Uniform Slot Separation

In this section, different *1 x 25* slotted CSIW arrays are designed at *25 GHz* to satisfy predefined radiation pattern criteria, i.e. the slotted CSIW array designs are examined in terms of pattern synthesis problem. For this purpose, a SLL value below *-20 dB* with pencil beam pattern is determined to be achieved by a traveling wave slot array on CSIW. Three different designs are carried out using the substrate and microstrip to SIW transition parameters mentioned in Section 2.1 and Section 2.2. *25* slot elements are used where the slot elements are uniformly distributed by $0.7\lambda_g$ spacing on CSIW with $R = 10\ cm$ as shown in Figure 4.1. In the designs, first of all the required slot voltages are determined which gives the desired radiation pattern. The expression of the required slot voltage to be satisfied by the p^{th} slot in the array is given by

$$V_p^s = a_p e^{j\psi_p} \tag{4.4}$$

where a_p and ψ_p are the amplitude and phase of the required p^{th} slot voltage, respectively. Then using these required slot voltages, the proper slot offset and length values are found by applying Elliott's design procedure as shown in Figure 4.25.

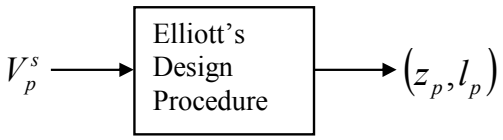

Figure 4.25: The function of the Elliott's design.

In the *1st 1 x 25* uniform slot array design, the aperture projection method is used to determine the excitation amplitudes, W_p^{DE} shown in Figure 4.10 (b) where these weights are determined for one of the design cases presented in Section 4.1.1.2. Hence, the required slot amplitudes are chosen as $a_p = W_p^{DE}$ for $p = 1, 2, ..., 25$. In order to increase the directivity in the desired direction, $\hat{n}$, which is not necessarily in $\hat{a}_y$-direction as shown in Figure 4.1, the proper slot phase values, ψ_p are determined which compensate phase delays due to different path lengths between the slots and planar aperture where the normal vector of the planar aperture, $\hat{n}$ shows the direction of the main beam. In the *1st* design, the direction of the main beam is determined as $\phi_m^n = 92°$ and the slot phases are determined as $\psi_p = -k_0 \hat{n}.\bar{r}_p$. The reason of choosing the main beam direction as *92°* will be explained later. The slot phases are satisfied by allowing large deviations in the slot lengths from their resonance values in the design. In order to expect the deviation of the slot from the resonance, the mode voltages are initially assumed to be traveling only in the excitation direction exciting each slot without encountering any reflections due to the slots as shown in Figure 4.26. Hence, the mode voltage exciting the p^{th} slot is given by

$$V_p' = a_p^v e^{j\varphi_p} \tag{4.5}$$

where a_p^v and $\varphi_p = -L_p \beta_{10}$ are amplitude and phase of the mode voltage. β_{10} is the propagation constant of the fundamental mode used to excite the waveguide and L_p

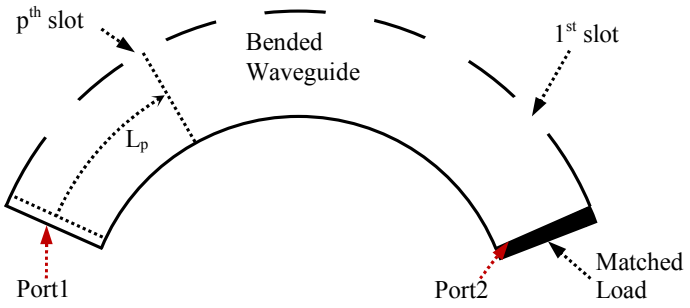

Figure 4.26: Slot array on bended regular waveguide.

is the distance between the Port1 and the center of the slot as shown in Figure 4.26. In (4.5), prime sign is used in the mode voltage expression in order to discriminate the mode voltage calculated in (4.5) from the actual mode voltage calculated in (3.78). The difference between (3.78) and (4.5) is that the actual mode voltages are calculated in (3.78) while the Elliott's design procedure is applied; however, the approximate mode voltages in (4.5) are used before the Elliott's design procedure while making initial design on the slot voltages. The actual mode voltages found using (3.78) are given by

$$V_p = a_p^e e^{j\varphi_p^e} \tag{4.6}$$

where a_p^e and φ_p^e are the amplitude and phase of the actual mode voltage for the p^{th} slot, respectively.

The relation between the slot voltage and mode voltage is previously derived in (3.29). In order a slot to be at resonance, the active admittance presented in (3.29) should be purely real positive. Since the term K_1 in the active admittance formula in (3.29) is purely imaginary, there should be $90°$ phase difference between the slot phase and mode voltage phase when the slot is at resonance. Hence, the phase value, φ_p^1 is defined as $\varphi_p^1 = \varphi_p - 90^0$ such that the slot is assumed to be at resonance if

$\varphi_p^1 = \psi_p$ or $\varphi_p^1 = \psi_p + 180^0$. Note that the case where $\varphi_p^1 = \psi_p + 180^0$ corresponds to alternating the slot to the other half side of the waveguide compared to the case where $\varphi_p^1 = \psi_p$. The deviation of the slot from resonance is defined for the p^{th} slot as

$$D_p^1 = e^{j\left(\psi_p - \varphi_p^1\right)} \tag{4.7}$$

Similarly, the phase value, φ_p^2 is defined as $\varphi_p^2 = \varphi_p^e - 90^0$ such that the slot is actually at resonance if $\varphi_p^2 = \psi_p$ or $\varphi_p^2 = \psi_p + 180^0$. The actual deviation of the slot from resonance is defined for the p^{th} slot as

$$D_p^2 = e^{j\left(\psi_p - \varphi_p^2\right)} \tag{4.8}$$

Since the values of D_p^2 are not known before determining the slot offsets and lengths in the Elliott's design procedure, the initial design of slot phases, ψ_p are carried out using (4.7).

In the *1st 1 x 25* uniform slot array design, D_p^1 is plotted by cross labels in Figure 4.27 (a) on the unit circle. The slots corresponding to the D_p^1 points located at *0°* and *180°* in Figure 4.27 (a) are considered to be at resonance for the positive and negative slot offset directions, respectively. The deviation of the slot phase, ψ_p from the phase, φ_p^1 determines the deviation of the slot from the resonance. ±*50°* deviation from the resonance is considered to be safe enough to avoid numerical problems [54]. Moreover, the decrease in the efficiency of the array due to allocating elements out of resonance is limited by preventing the slots to deviate from resonance more than *50°*.

The graph shown in Figure 4.27 (a) is divided into four regions using the constant phase lines defined by ±*50°* deviation from *0°* and *180°*. The regions I and III in Figure 4.27 (a) are considered to be the safe regions in which the slots deviate from resonance by maximum amount of ±*50°*. In Figure 4.27 (a), changing the resonant slot element requires a constant phase shift applied in ψ_p values for all the elements. Hence, it causes a rotation of the phase deviation values on the unit circle. Changing

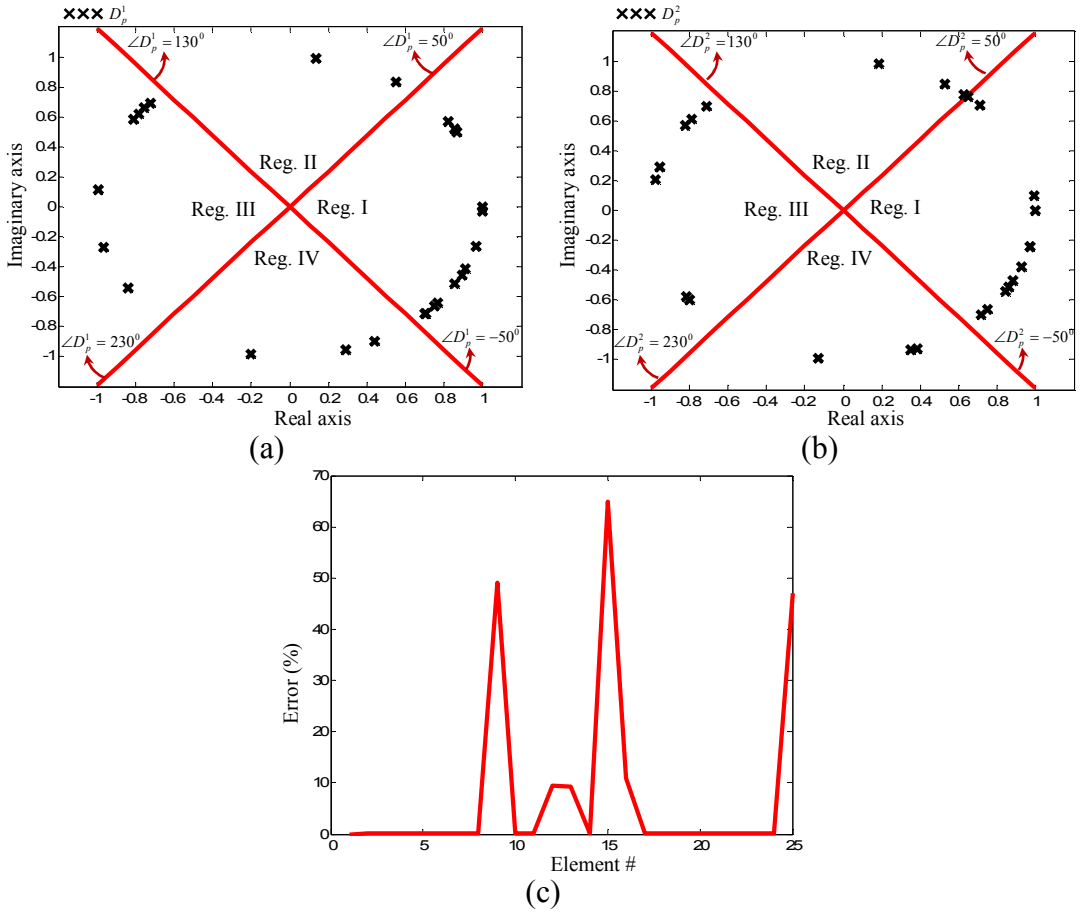

Figure 4.27. Phase and error graphs for *1 x 25* slot array on CSIW (*1st* design): (a) Deviation of slot phases from mode voltage phases ($\angle D_p^1$). (b) Deviation of slot phases from mode voltage phases in Elliott's design ($\angle D_p^2$). (c) Error in the Elliot's design.

the desired main beam direction also affects the required slot phases. Hence, the main beam direction, ϕ_m^n is chosen as *92°* as shown in Figure 4.1 and also the first element which is closest to the match load in the CSIW is chosen as a resonant element in order to maximize the phase points in regions I and III. The phase of the resonant element is adjusted by applying a constant phase shift on all of the desired slot voltage phases found by $\psi_p = -k_0 \hat{n}.\bar{r}_p$ so that $\varphi_1^1 = \psi_1$. Hence, the required slot phases are determined.

The Elliott's design procedure is applied using the slot excitation amplitudes, a_p and phases, ψ_p to determine the slot offsets and lengths for the *1st* design. In the Elliott's design, the active admittance formulas derived for longitudinal slot array on cylindrical waveguide in Section 3.1.2 are used. The slot offsets and lengths found for the *1st 1 x 25* slot array design on CSIW are listed in Table 4.6. The phase deviations of the slots, D_p^2 calculated after the Elliott's design, are plotted on the unit

Table 4.6: Slot offsets and lengths for *1 x 25* slot array on CSIW (*1st* design).

Element #	Slot Offset (mm)	Slot Length (mm)	**Element #**	Slot Offset (mm)	Slot Length (mm)
1	0.250	4.089	**14**	-0.262	4.043
2	0.145	4.093	**15**	-0.123	3.748
3	0.190	4.122	**16**	0.227	3.801
4	0.242	4.188	**17**	-0.122	3.925
5	0.175	4.075	**18**	0.096	3.920
6	0.203	4.028	**19**	-0.191	4.086
7	0.177	3.947	**20**	0.090	4.049
8	0.314	3.899	**21**	-0.087	3.971
9	0.282	3.843	**22**	0.064	4.015
10	-0.271	4.091	**23**	-0.053	3.899
11	-0.255	3.846	**24**	0.108	3.871
12	0.467	4.519	**25**	0.070	4.153
13	0.191	3.778			

circle in Figure 4.27 (b). As it is seen Figure 4.27 (b), some of the phase values get closer to the $+50°$ line compared to the phase values shown in Figure 4.27 (a). Although, the slot phases are affected by initially assuming a traveling wave mode voltage, Figure 4.27 (a) and (b) shows that designing the slot phases by assuming D_p^1 is a good approximation.

The error function used in the Elliott's design procedure is defined in Section 3.2. The error function calculated at the final step in the Elliott's design procedure is plotted for each slot in Figure 4.27 (c). As it is seen in Figure 4.27 (c), there is large error above *50 %*. The large error observed at the 25^{th} slot in Figure 4.27 (c) is due to the small slot offset value as listed in Table 4.6 for the 25^{th} slot. In the Elliott's design, numerical errors might be encountered when it is required to find the small slot offset values because small slot offsets have small shunt admittance values which are highly affected by the mutual couplings. Hence, numerical errors might be encountered if the slot offset value required to be determined is small depending on the value of the mutual coupling value for the slot under concern. The error above *10 %* for the slots other than 25^{th} slot occurs for 9^{th}, 12^{th}, 13^{th}, 15^{th}, and 16^{th} slots which are close to the center of the array. These errors in *5* different slots are caused by *5* slots largely deviating from resonance as shown in Figure 4.27 (b). Since the imaginary part of the self-admittance shown in Figure 2.10 (b) has a limited range, $\pm 90°$ deviation from the resonance cannot be reached and errors increase as the slots deviate from resonance.

The slot amplitudes, a_p and phases, ψ_p desired to be satisfied in the 1^{st} *1 x 25* slot array design is compared to the HFSS simulations in Figure 4.28 (a) and (b), respectively. The HFSS simulations are carried out by using the slot offsets and lengths given in Table 4.6 determined by the Elliott's design procedure. In Figure 4.28 (a), the maximum relative deviation of the amplitude coefficients found by using Elliott's design from the desired taper is about *0.18*. This amount of error is

usually encountered in the Elliott's design. However, large fluctuations observed at the peak positions are unusual if Elliott's design is successfully applied.

The radiation pattern of the slots on CSIW are calculated in the H-plane by using an in-house code developed for calculating the slot array pattern where the slot element pattern is taken into account in the code. Using the desired slot excitation coefficients (V_p^s), the radiation pattern of the desired slot array on CSIW is calculated. The

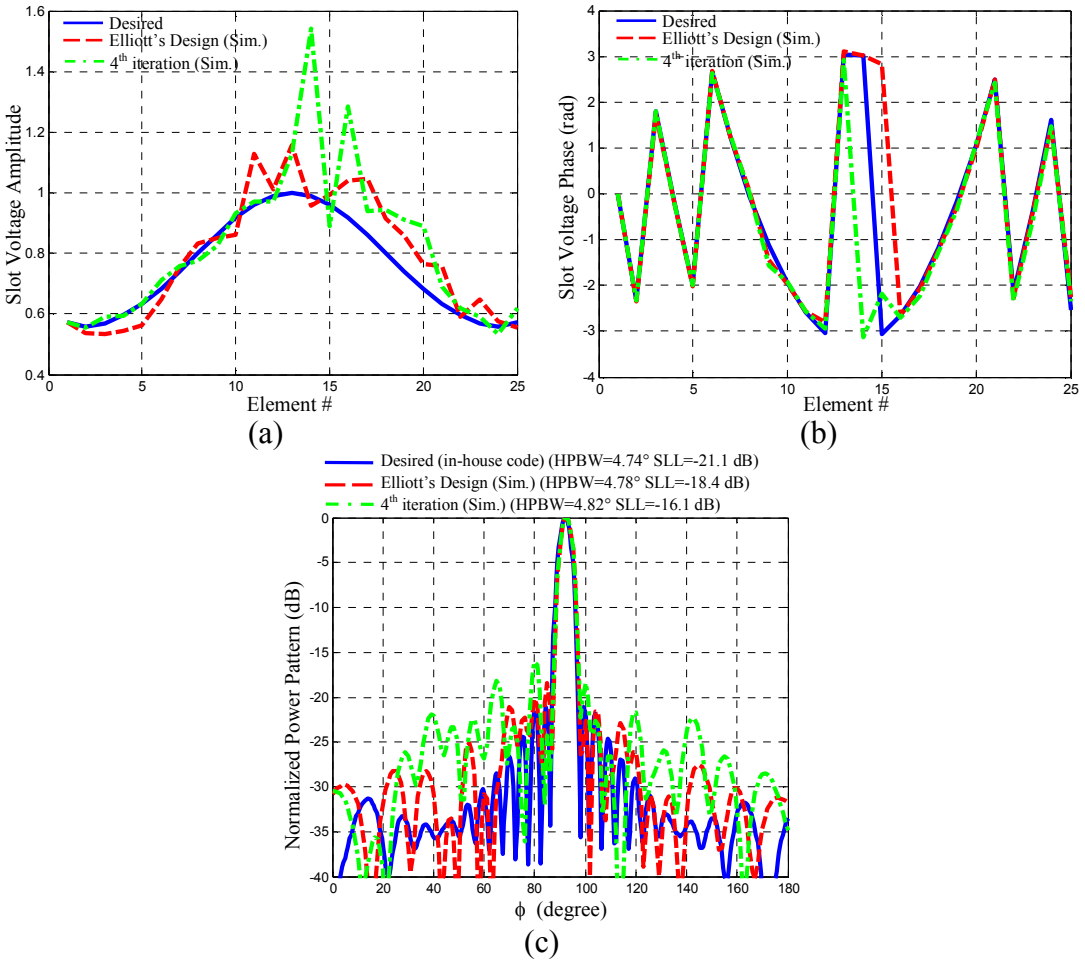

Figure 4.28. Slot voltage (a) amplitudes and (b) phases for *1 x 25* slot array on CSIW. (c) H-plane radiation patterns (1^{st} design).

calculated pattern is compared with the HFSS simulation in Figure 4.28 (c) where the simulations are carried out using slot offsets and lengths found from the Elliott's design listed in Table 4.6. Due to the fluctuations in the amplitude terms of the Elliot's design in Figure 4.28 (a), desired SLL could not be reached in the H-plane radiation pattern of the Elliott's design shown in Figure 4.28 (c). The difference between SLL values in the radiation pattern of the Elliott's design and the desired array pattern is about *2.7 dB*.

The fluctuations in the amplitude distribution of the Elliott's design Figure 4.28 (a) is tried to be reduced by using an iterative procedure. The iterative procedure is developed using similar approach presented in [55]. In [55], the electric fields found by Method of Moments (MoM) formulation are scaled to obtain desired pattern while the active admittance formulas are scaled and HFSS simulations are used in this thesis to obtain desired slot voltage distribution in the simulations. The initial values of the slot offsets and lengths can be determined using Elliott's design procedure, [55]. Once the Elliott's design is completed, the term $Y_p^a\left(z_p,l_p\right)\big/ f_p^{TE_{10}^z}\left(z_p,l_p\right)$ in (3.79) is known for all the slots for $p = 1, 2, 3,\ldots, 25$. This term is modified in each iteration as

$$\frac{Y_p^{a,i}\left(z_p^i,l_p^i\right)}{f_p^{TE_{10}^z,i}\left(z_p^i,l_p^i\right)} = \alpha_p^i \frac{Y_p^{a,i-1}\left(z_p^{i-1},l_p^{i-1}\right)}{f_p^{TE_{10}^z,i-1}\left(z_p^{i-1},l_p^{i-1}\right)} \tag{4.9}$$

where α_p^i is a scaling constant while $\left(z_p^i,l_p^i\right)$ is the slot offset and length pair for the p^{th} slot in the i^{th} iteration. In each iteration, the scaling constant α_p^i is determined by comparing the simulated slot voltages with the desired slot voltages and new slot offset and length values are found for the slots using the scaled active admittance terms in (4.9). Then the simulations are repeated with new slot offsets and lengths to find new slot voltages in the simulations for the next iteration. The iterations are repeated until the convergence is obtained in the simulated and desired slot voltages.

The term $Y_p^{a,0}\left(z_p^0, l_p^0\right) \Big/ f_p^{TE_{10}^z,0}\left(z_p^0, l_p^0\right)$ which appears at the RHS of (4.9) is determined from the Elliott's design procedure for $i = 1$ and $p = 1, 2, 3, \ldots, 25$. The values of $Y_p^{a,i}\left(z_p^i, l_p^i\right) \Big/ f_p^{TE_{10}^z,i}\left(z_p^i, l_p^i\right)$ are determined for each slot in each iteration by searching the values of $\left(z_p^i, l_p^i\right)$ as described in the 6^{th} step of the Elliott's design procedure presented in Section 3.2. In (4.9), it is assumed that scaling the active admittance value for the p^{th} slot does not affect the other active admittance values, similar to the idea of aperture decoupling as described in [55]. The mutual coupling terms can be recalculated using the slot offset and length values calculated from previous iteration and they can be used in the next iteration. Since the slot offsets and lengths are not expected to deviate much from their initial values, the mutual coupling terms which are calculated in the last step of the Elliott's design procedure can be used in all the iterations to save the time required for the iterations. If the mutual couplings are ignored in the iterations, convergence can still be obtained. Furthermore, the substrate and metal losses, which are not considered in the Elliott's design and encountered in the simulations, are also taken into account in this iteration technique. The scaling constant α_p^i in the iteration is given by

$$\alpha_p^i = \sqrt{\frac{V_p^{des}}{V_p^{Sim,i-1}}} \tag{4.10}$$

where V_p^{des} is the desired complex slot voltage distribution to be satisfied and they are already plotted in Figure 4.28 (a) and (b) for the *1st 1 x 25* slot array design. The complex slot voltages, $V_p^{Sim,i-1}$, are determined for all the slots by using the simulations carried out with the slot offset and length pairs $\left(z_p^{i-1}, l_p^{i-1}\right)$ found at the $(i-1)^{st}$ iteration. Note that for $i = 1$, the values of $V_p^{Sim,0}$ have already been plotted in Figure 4.28 (a) and (b) as dashed curves. The square root in (4.10) is used to avoid the oscillations of the slot voltages, $V_p^{Sim,i-1}$ found at each iteration, and hence, to obtain smooth convergence in the slot voltage distribution. Both the amplitudes and

phases of the slot voltages are corrected in each iteration step. The iterations are carried out by taking the first slot as a reference such that the first slot offset, length, and the first slot voltage values are not changed in the iterations. This is the reason for the desired and simulated slot voltages for the first slot element to be equal in Figure 4.28 (a) and (b) and they are equal in all the iteration steps. Hence, the value of $\left(z_p^i, l_p^i\right)$ are not changed for $p = 1$ in each iteration step. Moreover, the values of $V_p^{Sim,i-1}$ obtained in the simulations for each iteration step are scaled by the same complex constant such that $V_1^{Sim,i-1}$ is equated to V_1^{des} in each iteration step.

The iteration procedure can be used to achieve any slot distribution, however, the excitation weights to be realized are limited by the range of the phase values which can be achieved by the slots around the resonance. The iterations are carried out for the 1^{st} *1 x 25* slotted CSIW array. The excitation coefficients and the radiation pattern diverge from desired patterns after *4* iterations as shown in Figure 4.28 because the phase values near *90°* in Figure 4.27 (a) and (b) could not be achieved by the slot.

The 2^{nd} *1 x 25* slot array design on CSIW is carried out by determining the desired slot voltages using a genetic algorithm code. The phase values, Ψ_p and the slot amplitudes, a_p are the inputs of the algorithm for $p = 1, 2, 3, \ldots, 25$. Hence, total *50* inputs constitute the genomes of the algorithm. The slot phases, ψ_p are designed using the input phases, Ψ_p in the code. The input values of the algorithm changes between *0* and *1*. The amplitudes a_p are set free to vary continuously between *0* and *1*, however, restrictions are applied on the input phase values, Ψ_p. Since all the slot phases, ψ_p usually could not be designed by phase compensation technique so that phases of D_p^1 are positioned in the safe regions I and III as shown in Figure 4.27 (a), and also since this situation causes problems in obtaining desired radiation pattern, the restrictions on slot phases are applied in the genetic algorithm. This is

accomplished as follows. First of all, the input phases, Ψ_p varying between *0* and *0.5* are mapped to the angle values between *-35°* and *35°* and also Ψ_p values varying between *0.5* and *1* are mapped to the angle values between *145°* and *215°*. As a result of this mapping, the phase values, Ψ_p^1 are obtained. Then the slot voltage phases, ψ_p are obtained by adding φ_p^1 values to Ψ_p^1 values. Hence, the phase of D_p^1 in (4.7) becomes Ψ_p^1 which have maximum *±35°* deviation from *0°* and *180°*. After determining the slot phases, the H-plane radiation pattern of the slot array on CSIW is calculated using in-house code mentioned before. The SLL of the H-plane radiation pattern is calculated and it is minimized till the desired SLL value is reached in the code. No criterion is applied for HPBW because HPBW value becomes good enough when the SLL is suppressed low enough. The optimization is terminated when the SLL below desired value is reached. The population size in genetic algorithm is chosen as *500* in order to reach the global solution. The genetic algorithm optimizations are carried out and the desired radiation pattern is obtained as shown in Figure 4.29 (c). In Figure 4.29 (c), the main beam direction of the desired radiation pattern is $\phi_m^n = 80^o$ which is in the backward quadrant defined by $0^o < \phi_m^n < 90^o$ where *90°* is the broadside angle. This can be explained as follows. The slotted waveguide antennas resemble to the periodic leaky wave antennas when the waveguide is dielectric filled and the fundamental mode propagating in the waveguide is a slow wave. In this study, the fundamental mode in the CSIW is a slow wave at *25 GHz*. The main difference between uniform and periodic leaky wave antennas is that the former can radiate only into the forward quadrant, i.e., $90^o < \phi_m^n < 180^o$ while the latter can radiate into both forward and backward quadrants [48].

The slot amplitudes, a_p and phases, ψ_p found in the optimization are also shown as desired amplitudes and phases in Figure 4.29 (a) and (b), respectively. Note that the desired slot amplitudes, a_p and phases, ψ_p shown in Figure 4.29 differs from the

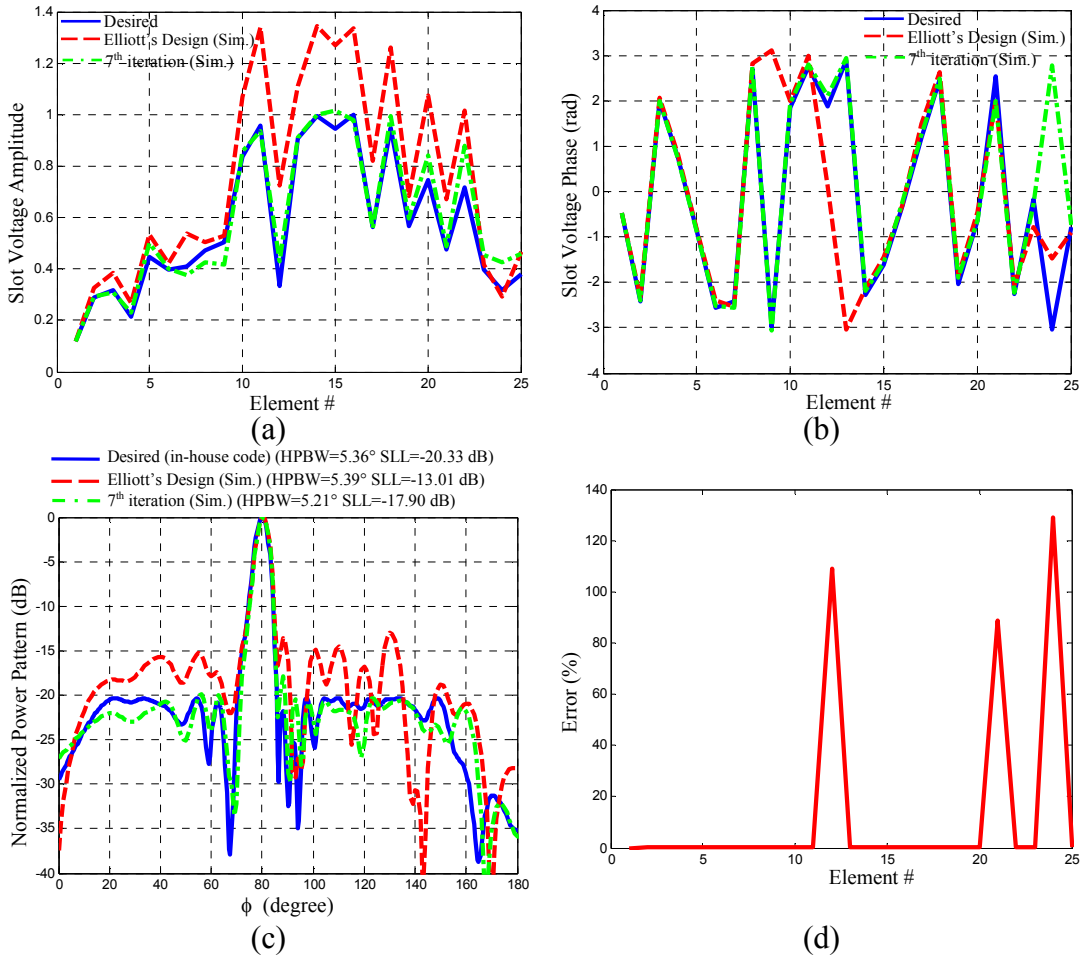

Figure 4.29. Slot voltage (a) amplitudes and (b) phases for *1 x 25* slot array on CSIW. (c) H-plane radiation patterns (2^{nd} design). (d) Error in the Elliot's design.

desired slot amplitudes and phases shown in Figure 4.28 because the slot voltage coefficients are determined by genetic algorithm in the 2^{nd} design shown in Figure 4.29 while the aperture projection method is used together with phase compensation in the 1^{st} design shown in Figure 4.28.

The Elliott's design procedure is applied using the slot amplitudes, a_p and phases, ψ_p determined in the genetic optimization for the 2^{nd} *1 x 25* slot array design on CSIW. Hence, the slot offsets and lengths of the 2^{nd} *1 x 25* slot array are determined.

Using the slot offsets and lengths determined in the Elliott's design, the simulation of the *2nd 1 x 25* slot array is carried out. As it is seen in Figure 4.29 (c), the radiation pattern obtained from the simulations of the Elliott's design does not satisfy desired *-20 dB* SLL because of the difference between the corresponding amplitude and phase curves obtained from simulations presented in Figure 4.29 (a) and (b), respectively. The maximum value of the error function in the Elliott's design is found above *90 %* only for the *12th*, *21st*, and *24th* slots as shown in Figure 4.29 (d). Although the phases of the elements are properly determined, this error is caused by the small slot offset values tried to be determined as mentioned before. As it is seen in Figure 4.29 (a), the desired amplitude taper reduces abruptly for the *12th* slot which makes the slot offset value of the *12th* slot so small that causes errors in the Elliott's design procedure. Moreover, the desired voltage amplitudes for the *21st* and *24th* slots are also small which requires small slot offset values vulnerable to errors for these slots.

The iterations are carried out to find the slot offsets and length which satisfy desired slot voltages, and hence, to find the desired pattern. The slot voltages found after *7* iterations are plotted in Figure 4.29 (a) and (b). Iterations are terminated at *7* because no significant improvement is observed compared to the slot voltages and SLL value in the *6th* iteration. As it is seen in Figure 4.29 (a) and (b), the slot voltages at the *7th* iteration are quite close the desired curve. However, there are still some difference between the *7th* iteration curves and desired slot voltages. Although the radiation pattern of the *7th* iteration shown in Figure 4.29 (c) almost converge to the desired radiation pattern, the desired *-20 dB* SLL criteria could not be satisfied due to these small differences. The difference between the desired SLL and the SLL obtained at *7th* iteration is *2.43 dB*.

In the iterations of the *2nd 1 x 25* slot array design, the smooth convergence could not be obtained because of high values of the error function found for the *12th* slot which is located at the center of the array. The errors arising from small slot offset values at

two ends of the waveguide might be acceptable because the required amplitude taper reduces toward ends. Since there is an abrupt change in the amplitude taper at the 12^{th} slot, the offset value of the 12^{th} slot is too small which causes an error above *100 %*. This error at the center slot affects the radiation pattern. Due to such large errors, the number of iterations to be carried out increases and as it is seen in Figure 4.29 (a), the convergence is still not obtained after *7* iterations. There is still some difference between the slot voltages for the 12^{th} slot having small slot offset which makes the iteration procedure difficult. Hence, large oscillations in the desired slot voltage amplitudes are not suitable because they increase the number of small slot offset values to be implemented which increases the errors in the code. Moreover, the iterations could not be implemented due to these small slot offsets. It is more proper to use the slot voltage amplitude distribution which monotonically increases till the center of the array and then decreases toward the end slot.

The 3^{rd} design of *1 x 25* slot array on CSIW is carried out by employing a smooth variation in the desired slot voltage amplitude. For this reason, the slot amplitudes, a_p are determined by the weights, W_p^{DE} calculated using (4.3). W_p^{DE} values are calculated similar to the ones shown in Figure 4.10 using the aperture projection method with *-25 dB* SLL Taylor ($\tilde{n} = 3$) line source distribution. The phase only synthesis is carried out using genetic algorithm to determine the slot phases, ψ_p. Using the procedure similar to the 2^{nd} *1 x 25* slot array design on the input phases, Ψ_p the genetic algorithm optimization is applied such that the maximum allowed phase deviation in D_p^1 from *0°* and *180°* is *±50°* which is chosen large enough to help the code to find the desired pattern. As a result of disturbing the compensated slot phases by restricting the maximum deviation of the slot elements from resonance to *±50°*, the SLL values are expected to increase. The genetic algorithm code is used with a safety margin of *2.5 dB* in the SLL goal such that the desired SLL value is set to *-22.5 dB*. This safety margin is applied in the code in order to compensate possible increase in the SLL due to the errors encountered in the Elliott's design procedure.

Similar to the *2nd 1 x 25* slot array design, the population size in genetic algorithm is chosen as *500* and the optimizations are carried out for the *3rd* design. The desired slot phases, ψ_p are determined after the optimizations. The desired slot amplitudes, $a_p = W_p^{DE}$, determined from *-25 dB* SLL Taylor ($\tilde{n}$ = *3*) distribution and the desired slot phases, ψ_p, determined by the genetic optimization are shown in Figure 4.30 (a) and (b), respectively. The radiation pattern obtained from the desired slot voltages and phases is the pattern synthesized in the genetic algorithm which is plotted as a desired pattern shown in Figure 4.30 (c). In Figure 4.30 (c), the main beam direction

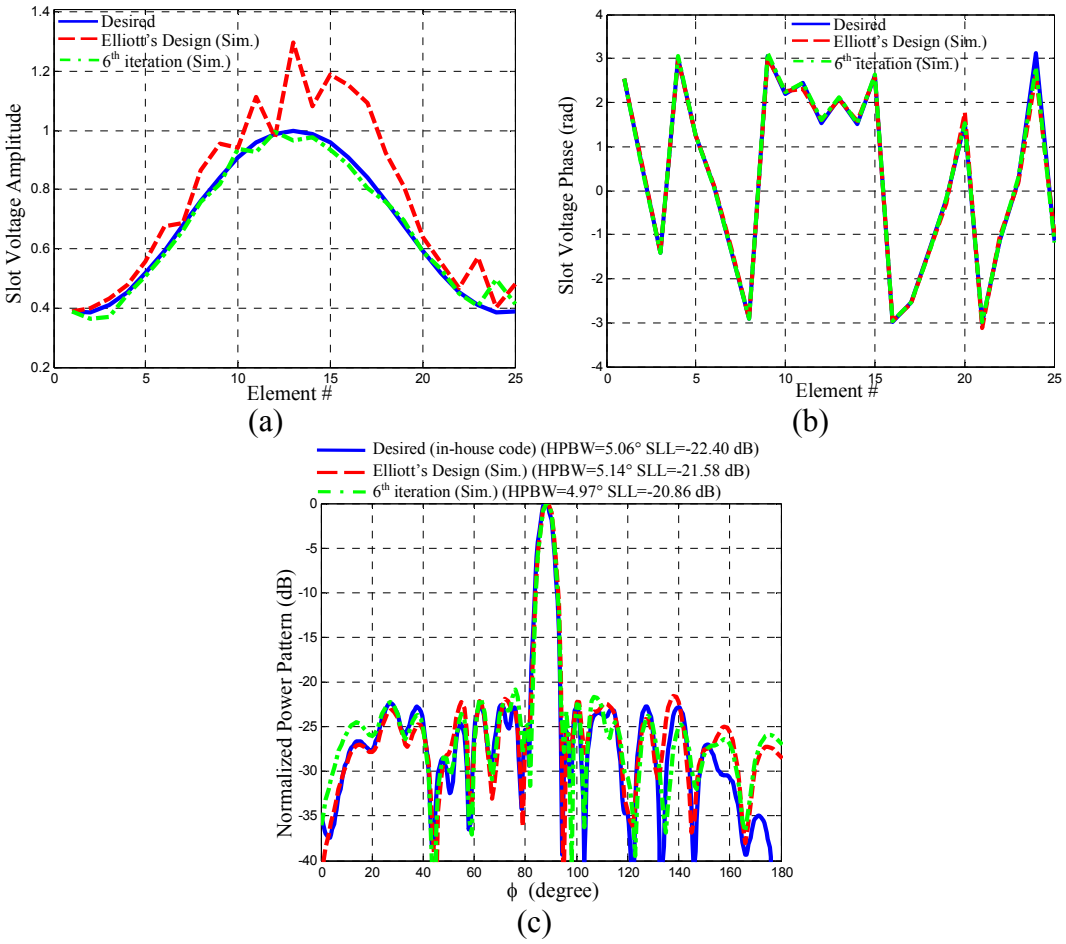

Figure 4.30. Slot voltage (a) amplitudes and (b) phases for *1 x 25* slot array on CSIW. (c) H-plane radiation patterns (*3rd* design).

of the desired radiation pattern is $\phi_m^n = 88^o$. In the optimization, the SLL of the desired radiation pattern is found as around *-22.4 dB*.

The deviation of the slot phases from resonance, D_p^1, found after the genetic algorithm code is shown in Figure 4.31 (a). As it is seen in Figure 4.31 (a), all the slots are in the safe regions which are regions I and III. The Elliott's design

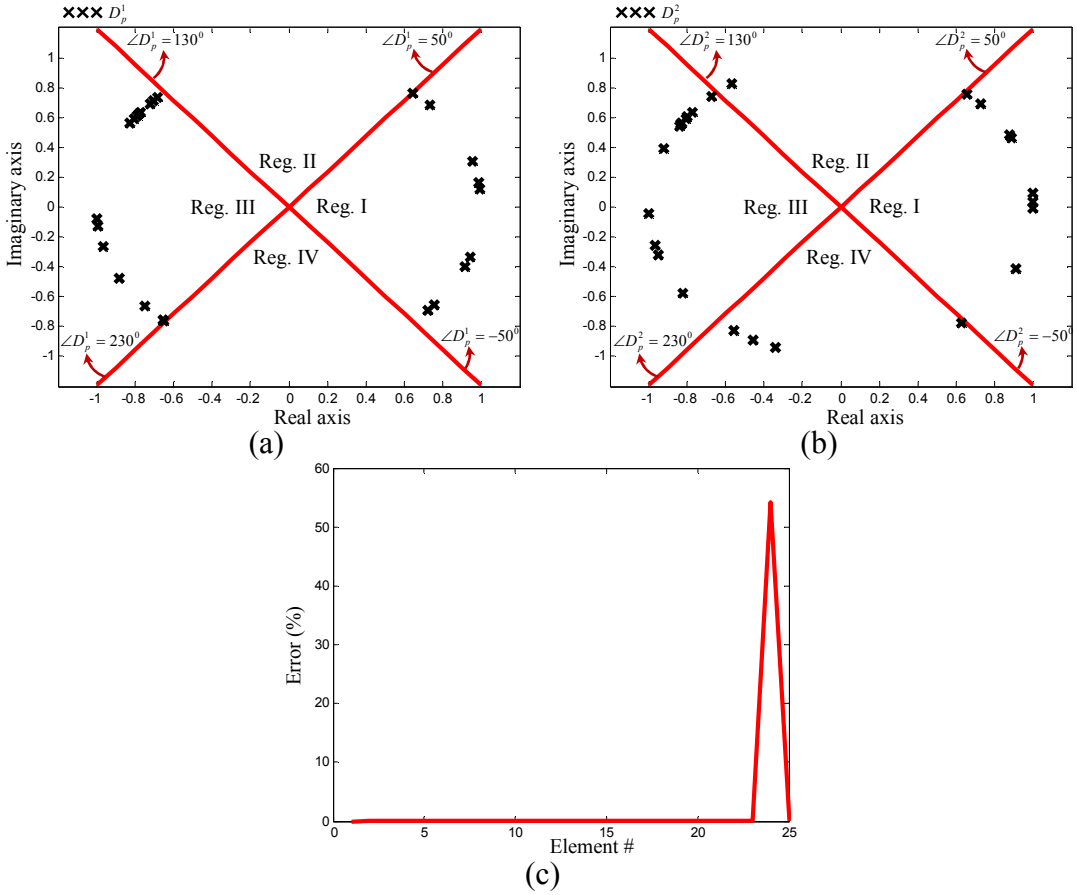

Figure 4.31. Phase and error graphs for *1 x 25* slot array on CSIW (3^{rd} design): (a) Deviation of slot phases from mode voltage phases ($\angle D_p^1$). (b) Deviation of slot phases from mode voltage phases in Elliott's design ($\angle D_p^2$). (c) Error in the Elliot's design.

procedure is carried out to find the slot offsets and lengths to satisfy desired slot voltage distribution. The slot offsets and lengths found after the Elliott's design procedure is listed in Table 4.7. The error obtained in the Elliott's design code is presented in Figure 4.31 (c). The high error above *50 %* is calculated for the 24^{th} slot. As it is seen in Table 4.7, the value of the offset is small for the 24^{th} slot and the large error is caused by this small slot offset value. The phase deviation values, D_p^2, calculated after the Elliott's design code are plotted in Figure 4.31 (b). As it is seen in Figure 4.31 (b), the slots do not deviate much from the safe region after the Elliott's design procedure.

The simulations are carried out using the slot offset and length values listed in Table 4.7 found by Elliott's design. The slot voltage distribution found from simulations of the Elliott's design is compared with the desired slot voltages in Figure 4.30 (a) and (b). The maximum difference between the slot amplitudes is found as about *0.3* around the peak position in Figure 4.30 (a). Furthermore, the maximum difference in the phases is *0.486 rad* at the 24^{th} slot. These differences between the Elliott's design

Table 4.7: Slot offsets and lengths for *1 x 25* slot array on CSIW (3^{rd} design).

Element #	Slot Offset (mm)	Slot Length (mm)	**Element #**	Slot Offset (mm)	Slot Length (mm)
1	-0.250	4.175	**14**	0.117	3.777
2	-0.131	4.066	**15**	-0.310	3.761
3	-0.183	4.106	**16**	0.201	3.914
4	-0.202	4.119	**17**	-0.092	3.927
5	-0.192	4.023	**18**	0.142	3.968
6	-0.228	3.947	**19**	-0.141	4.153
7	-0.231	3.905	**20**	0.055	3.938
8	-0.377	3.904	**21**	-0.076	3.951
9	0.452	4.422	**22**	0.061	3.782
10	0.144	3.790	**23**	-0.197	3.680
11	-0.458	4.343	**24**	-0.057	4.238
12	-0.079	3.789	**25**	0.042	3.897
13	0.275	3.969			

code and simulations are usually encountered. Due to these differences both in the slot amplitudes and phases, the simulated radiation pattern of the Elliott's design shown in Figure 4.30 (c) has small deviation from the desired radiation pattern.

The iterations as mentioned before are carried out to obtain desired slot excitation coefficients at the slots. The design found using Elliott's design procedure is iterated and the slot offsets and lengths listed Table 4.8 are found after *6* iterations. The simulations are carried out using the slot parameters listed in Table 4.8 for the 6^{th} iteration. The slot voltages and corresponding radiation pattern simulated for the 6^{th} iteration are presented in Figure 4.30. As it is seen in Figure 4.30 (a) and (b), the simulated slot voltages for the 6^{th} iteration are quite close to the desired slot voltages. Although, the SLL could not be improved further in the iterations in Figure 4.30 (c), some of the side lobes are seen to get closer to the desired pattern. The difference between the desired SLL and the SLL obtained at 6^{th} iteration is *1.54 dB*. Moreover, the simulated S_{11} is reduced from *-11.5 dB* to *-13.5 dB* after *6* iterations at *25 GHz*.

Table 4.8: Slot offsets and lengths for *1 x 25* slot array on CSIW after 6^{th} iteration (3^{rd} design).

Element #	Slot Offset (mm)	Slot Length (mm)	**Element #**	Slot Offset (mm)	Slot Length (mm)
1	-0.250	4.175	**14**	0.110	3.797
2	-0.128	4.068	**15**	-0.286	3.756
3	-0.175	4.096	**16**	0.174	3.893
4	-0.194	4.111	**17**	-0.086	3.925
5	-0.178	4.022	**18**	0.126	3.976
6	-0.211	3.947	**19**	-0.120	4.092
7	-0.223	3.915	**20**	0.060	3.961
8	-0.341	3.868	**21**	-0.073	3.945
9	0.381	4.265	**22**	0.069	3.810
10	0.136	3.811	**23**	-0.163	3.686
11	-0.409	4.249	**24**	-0.056	4.104
12	-0.089	3.820	**25**	0.047	3.942
13	0.255	3.957			

4.3.1. Fabrication and Measurements

The slot array which is found after 6^{th} iteration in the 3^{rd} design of *1 x 25* slot array on CSIW is selected for fabrication. The slot offsets and lengths of the array to be fabricated are listed in Table 4.8. The fabrication of the slot array is carried out by Ilfa company which is founded for the fabrication of various PCB products. The array is fabricated on *0.5 mm* thick Rogers *3003* substrate where the substrate has *35 μm* thick copper cladding on both sides. Electroless nickel immersion gold (ENIG) surface plating is applied on the copper metallization to protect the copper from oxidation.

4.3.1.1. 1 x 25 Slot Array on CSIW

The fabricated *1 x 25* slot array is shown in Figure 4.32 (a). The s-parameters of the *1 x 25* slot array are measured and compared with the simulations in Figure 4.32 (b) and (c). The simulations are carried out both by using zero metal thickness and *35 μm* copper thickness in HFSS. The finite conductivity boundary condition is assigned on the metal surfaces with zero metal thickness using copper conductivity in HFSS. As it is seen in Figure 4.32 (b) and (c), there is quite good agreement between the simulated and measured results. Both simulated and measured S_{11} values shown in Figure 4.32 (b) are below *-10 dB* between *20 GHz* and *30 GHz*. The measured S_{21} values successfully mimic the simulated S_{21} results in Figure 4.32 (c). The simulations carried out using *35 μm* copper thickness are in better agreement with the measured results compared to the simulations with zero metal thickness.

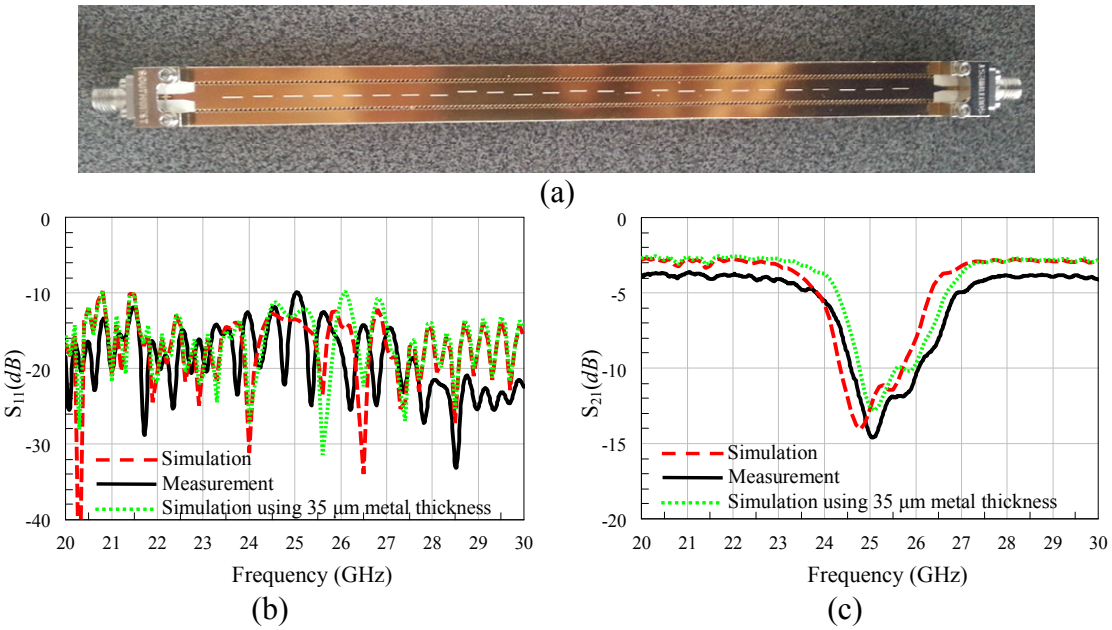

Figure 4.32: (a) Fabricated traveling wave *1 x 25* slot array on SIW. (b) S_{11} and (c) S_{21} results of the *1 x 25* slotted SIW array.

The radiation patterns of the *1 x 25* slotted CSIW array is measured in an anechoic chamber using the measurement setup shown in Figure 4.33. The patterns are

Figure 4.33: Measurement setup of *1 x 25* slot array on CSIW (*R = 10 cm*).

measured between *24 GHz* and *26 GHz* with *0.5 GHz* steps. The measurements are taken with *1°* angular resolution. The measured radiation patterns are compared with the simulations in Figure 4.34. The simulated radiation patterns in Figure 4.34 are obtained using *35 μm* copper thickness. Good agreement is observed between the measured and simulated radiation patterns in Figure 4.34. The SLL at *25 GHz* is below *-20 dB* in the simulations of the *25* element slotted CSIW array obtained after *6* iterations shown in Figure 4.30 (c) because this simulation does not take the conductor thickness into account. A waveguide with small length equal to the thickness of the copper is obtained in the slot regions, and hence, the slot voltages are affected which disturbs the SLL values in the initial design. In order to reduce the simulation time, the conductor thickness was ignored in the simulations and it was also not expected that the conductor thickness has such a large influence on the slot excitation coefficients. For this reason, the fine tuning of the design was not applied by considering the conductor thickness. It is concluded that if the design described in Figure 4.30 is carried out by considering the metal thickness in the simulations, desired SLL values can be reached.

The simulated and measured main beam positions are compared in Figure 4.34 (f). Good agreement is observed between the simulated and measured main beam positions. About *10°* beam steering is obtained when the frequency is changed between *24 GHz* and *26 GHz*. Since the measurements are taken with *1°* angular resolution, the maximum difference between the measured and simulated main beam positions is about *1°*.

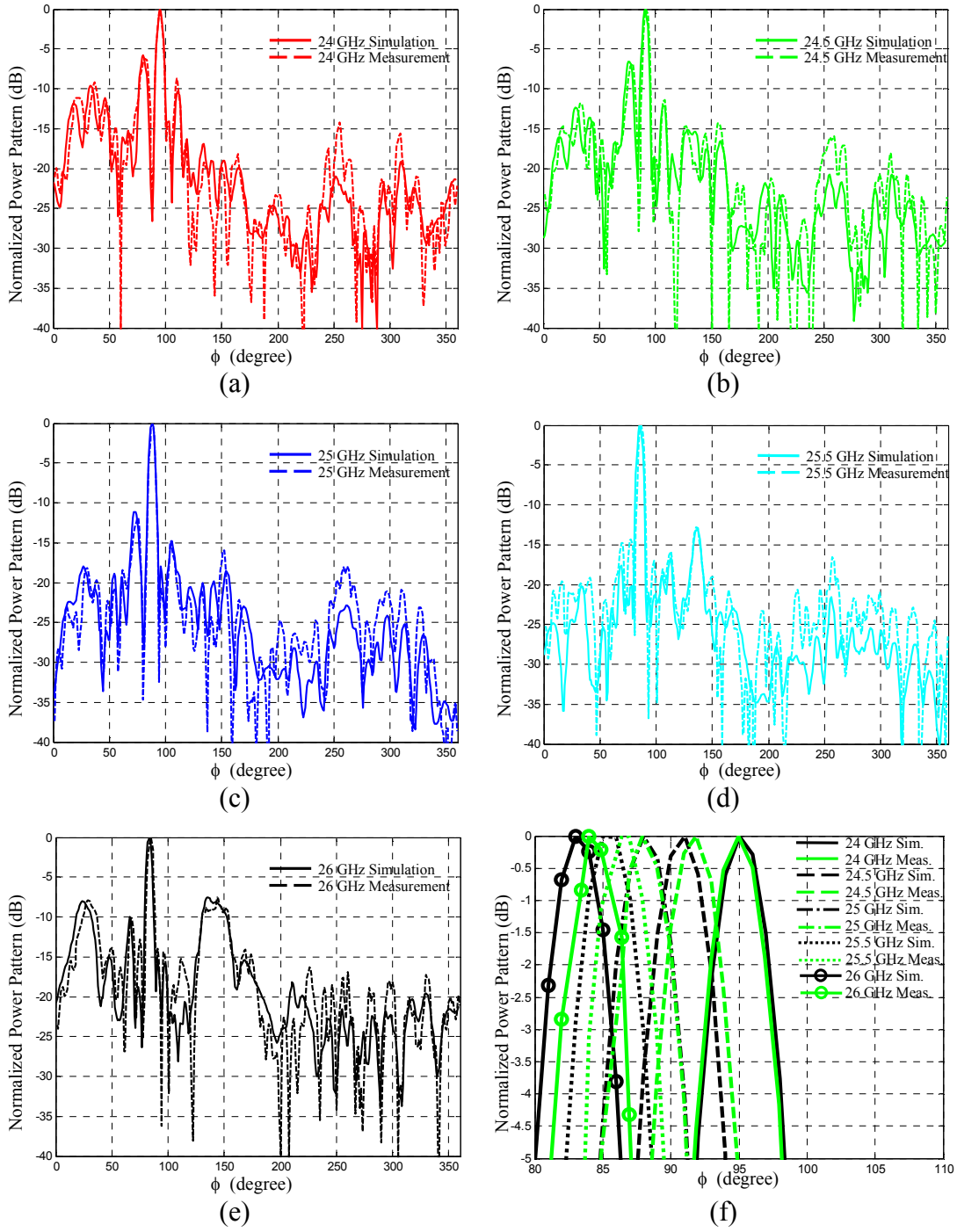

Figure 4.34: Radiation patterns of *1 x 25* slot array on CSIW.

The HPBW values of the patterns are calculated by interpolating the measured and simulated patterns. Moreover, the cross polarization levels of the patterns are measured. The HPBW values and cross polarization levels measured for different frequencies between *24 GHz* and *26 GHz* are compared with the simulations which take the effect of conductor thickness into account in Table 4.9. Good agreement is obtained between the measured and simulated results in Table 4.9.

Table 4.9: Simulated and measured HPBW and cross-polarization values of *1 x 25* slot array on CSIW.

	HPBW		**Cross-pol.**	
Frequency	**Meas.**	**Sim.**	**Meas.**	**Sim.**
24 GHz	4.90°	5.00°	-17.44 dB	-24.83 dB
24.5 GHz	4.83°	5.00°	-21.08 dB	-25.50 dB
25 GHz	4.58°	5.00°	-21.65 dB	-28.26 dB
25.5 GHz	4.88°	5.02°	-20.62 dB	-36.67 dB
26 GHz	4.81°	4.91°	-19.42 dB	-33.05 dB

The gain values of *1 x 25* slot arrays on CSIW are measured using the standard gain horn antenna for the frequencies between *24 GHz* and *26 GHz* with *0.5 GHz* steps. The measured gain values are compared with the simulations which take the effect of conductor thickness into account in Figure 4.35 (a). Since there is good agreement between the simulated and measured radiation patterns in Figure 4.34, the simulated directivity values are used to find the measured efficiency of the array in Figure 4.35 (b). The measured and simulated data is seen to be consistent with each other in Figure 4.35. The simulated gain at *25 GHz* is about *15.3 dB* while the measured gain is about *14.5 dB*. The maximum deviation between the measured and simulated gain is about *1.47 dB* at *25.5 GHz*. The small differences between the simulations and measurements in the gain and efficiency values are due to the small fabrication imperfections.

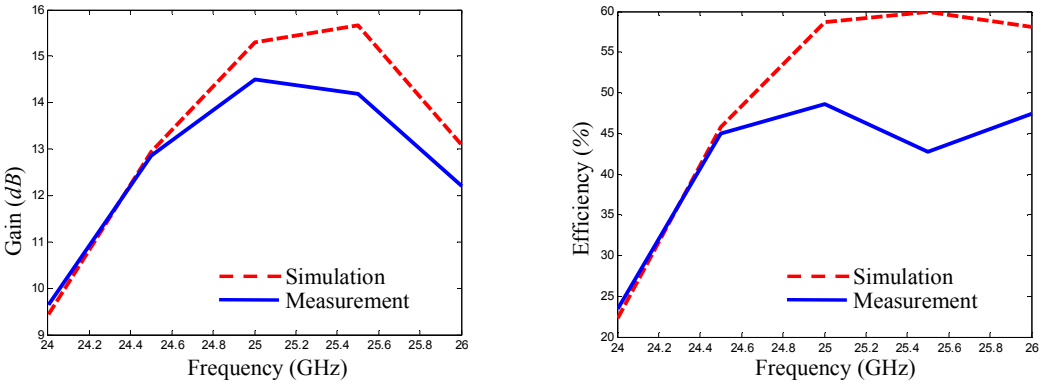

Figure 4.35: (a) Gain and (b) efficiency results of *1 x 25* SIW slot array.

The slotted CSIW arrays with uniform and non-uniform slot separations have both some advantages and disadvantages compared to each other. Using non-uniform slot separations is advantageous compared to uniform slot separations on CSIW because the former has slots near resonance while the latter allocates slots with large deviations from resonance, and hence, less number of active admittance calculations is required around the resonance for the design of slot array on CSIW with non-uniform slot separations. Furthermore, some of the complex slot voltage phases cannot be realized in the slotted CSIW array with uniform slot separation because the imaginary part of the slot admittance has limited range. In order to obtain desired radiation pattern using uniform slot separations, some of the optimization techniques can be used to find proper phase values both satisfying the desired pattern criteria and limiting the deviation of slots from resonance; however, the design complexity is increased. Furthermore, the pattern bandwidth of the slotted CSIW array with uniform slot separations might be adversely affected by the slots largely deviating from resonance because undesired slot modes might appear as a result of small frequency change. On the other hand, using uniform slot separations is advantageous compared to allocating non-uniform slot distribution in the slotted CSIW array design because a pattern with desired SLL can be synthesized by using uniform slot separations. In the slotted CSIW array with non-uniform slot separations, the element

separations are properly determined by the phase distribution requirements to obtain desired main beam and large element spacings might be encountered in the design which may cause undesired SLL values as discussed in Section 4.1.1. As a conclusion, based on the experience gained throughout this thesis study, uniform spacing can be preferred to meet high gain and low SLL design requirement of slotted CSIW arrays.

CHAPTER 5

CONCLUSIONS AND FUTURE WORK

The main goal of this thesis is to analyze, design, manufacture, and measure a traveling wave slot array at *25 GHz* on a novel CSIW structure where the CSIW lies in the circumferential direction of the cylinder. Different designs are carried out using non-uniform and uniform slot separations for beam steering and pattern synthesis applications. The slot separations are designed properly to obtain in phase contribution of each slot element to increase directivity in the non-uniform array. The aperture projection method is used to decrease the SLL, however, desired SLL could not be obtained in the non-uniform slot array because of large slot separation values. Hence, the slot lengths of the non-uniform array are optimized further to increase the bandwidth for beam steering applications. Although the SLL is increased to *-10 dB* after the optimizations, the fabricated non-uniform slot array has about *10°* beam steering when the frequency is swept between *24 GHz* and *26 GHz*. Three different designs are carried out using the uniform slot array to obtain pencil beam pattern and *-20 dB* SLL. The desired pattern is obtained at *25 GHz* using both the aperture projection method and phase only synthesis applied by genetic algorithm in the uniform slot array.

Based on the research carried out in the frame of this thesis, following conclusions can be drawn as follows:

- The mutual coupling and active admittance formulations are carried out for the slots on a novel CSIW structure using E-plane bend regular waveguides.

These novel formulations can be used to design slotted bend regular waveguide arrays which is not available in the literature.

- The derived formulations are validated by full wave simulations. The active admittance formulas are used in the Elliott's design procedure to design slotted CSIW arrays. The measurement results and the full wave simulations show that this novel array structure can successfully be designed using the proposed design formulas.
- The Elliott's design procedure is applied together with aperture projection method and genetic algorithm to satisfy both the desired radiation pattern and input match criteria. The iteration procedure is proposed for fine tuning of the slot voltages after the Elliott's design procedure.
- The slot array designs are successfully carried out for frequency steering and beam shaping applications. The antennas are fabricated and good agreement is obtained between the simulated and measured results.

The future works are summarized as follows:

- The active admittance formulations and Elliott's design procedure can be improved to take dielectric and conductor losses into account in the design.
- The iteration procedure can be carried out by taking the metal thickness into in the design of uniform slot array.
- The band of the slotted CSIW array can be improved by designing group of arrays operating at different frequencies in order to increase the scan coverage for the frequency steering applications.
- The dielectric losses which reduce the efficiency of the slotted CSIW array can be eliminated by improving the fabrication process to remove part of the substrate in CSIW.

REFERENCES

[1] L. Josefsson and P. Persson, *Conformal Array Antenna Theory and Design*. Hoboken, NJ: IEEE Press, 2003.

[2] J. Hirokawa and M. Ando, "Single-layer feed waveguide consisting of posts for plane TEM wave excitation in parallel plates," *IEEE Trans. Antennas Propag.*, vol. 46, no. 5, pp. 625-630, May 1998.

[3] D. Deslandes and K. Wu, "Integrated microstrip and rectangular waveguide in planar form," *IEEE Microw. Wireless Compon. Lett.*, vol. 11, no. 2, pp. 68-70, Feb. 2001.

[4] L. Yan, W. Hong, G. Hua, J. Chen, K. Wu, and T. J. Cui, "Simulation and experiment on SIW slot array antennas," *IEEE Microw. Wireless Compon. Lett.*, vol. 14, no. 9, pp. 446- 448, Sep. 2004.

[5] J. F. Xu, W. Hong, P. Chen, and K. Wu, "Design and implementation of low sidelobe substrate integrated waveguide longitudinal slot array antennas," *IET Microw., Antennas Propag.*, vol. 3, no. 5, pp. 790-797, Aug. 2009.

[6] S. E. Hosseininejad and N. Komjani, "Optimum design of traveling-wave SIW slot array antennas," *IEEE Trans. Antennas Propag.*, vol. 61, no. 4, pp. 1971-1975, April 2013.

[7] Q.-H. Lai, W. Hong, Z.-Q. Kuai, Y. S. Zhang, and K. Wu, "Half-mode substrate integrated waveguide transverse slot array antennas," *IEEE Trans. Antennas Propag.*, vol. 57, no. 4, pp. 1064-1072, April 2009.

[8] D.-Y. Kim, W.-S. Chung, C.-H. Park, S.-J. Lee, and S. Nam, "A series slot array antenna for 45°-inclined linear polarization with SIW technology," *IEEE Trans. Antennas Propag.*, vol. 60, no. 4, pp. 1785-1795, April 2012.

[9] Y. J. Cheng, W. Hong, K. Wu, Z.-Q. Kuai, C. Yu, J. X. Chen, J. –Y. Zhou, and H.-J. Tang, "Substrate integrated waveguide (SIW) rotman lens and its

Ka-band multibeam array antenna applications," *IEEE Trans. Antennas Propag.*, vol. 56, no. 8, pp. 2504-2513, Aug. 2008.

[10] P. Chen, W. Hong, Z. Kuai, J. Xu, H. Wang, J. Chen, H. Tang, J. Zhou, and K. Wu, "A multibeam antenna based on substrate integrated waveguide technology for MIMO wireless communications," *IEEE Trans. Antennas Propag.*, vol. 57, no. 6, pp. 1813-1821, Jun. 2009.

[11] T. Djerafi and K. Wu, "A low-cost wideband 77-GHz planar Butler matrix in SIW technology," *IEEE Trans. Antennas Propag.*, vol. 60, no. 10, pp. 4949-4954, Oct. 2012.

[12] B. Liu, W. Hong, Z. Kuai, X. Yin, G. Luo, J. Chen, H. Tang, and K. Wu, "Substrate integrated waveguide (SIW) monopulse slot antenna array," *IEEE Trans. Antennas Propag.*, vol. 57, no. 1, pp. 275-279, Jan. 2009.

[13] W. M. Abdel-Wahab, D. Busuioc, and S. Safavi-Naeini, "Millimeter-wave high radiation efficiency planar waveguide series-fed dielectric resonator antenna (DRA) array: analysis, design, and measurements," *IEEE Trans. Antennas Propag.*, vol. 59, no. 8, pp. 2834-2843, Aug. 2011.

[14] N. Ghassemi, K. Wu, S. Claude, X. Zhang, and J. Bornemann, "Low-cost and high-efficient W-band substrate integrated waveguide antenna array made of printed circuit board process," *IEEE Trans. Antennas Propag.*, vol. 60, no. 3, pp. 1648-1653, Mar. 2012.

[15] Y. J. Cheng, W. Hong, K. Wu, and Y. Fan, "Millimeter-wave substrate integrated waveguide long slot leaky-wave antennas and two-dimensional multibeam applications," *IEEE Trans. Antennas Propag.*, vol. 59, no. 1, pp. 40-47, Jan. 2011.

[16] D. Deslandes and K. Wu, "Substrate integrated waveguide leaky-wave antenna: concept and design considerations," in *Proc. Asia-Pacific Microw. Conf.*, Suzhou, China, 2005, pp. 346-349.

[17] F. Xu, K. Wu, and X. Zhang, "Periodic leaky-wave antenna for millimeter wave applications based on substrate integrated waveguide," *IEEE Trans. Antennas Propag.,* vol. 58, no. 2, pp. 340-347, Feb. 2010.

[18] J. Xu, W. Hong, H. Tang, Z. Kuai, and K. Wu, "Half-mode substrate integrated waveguide (HMSIW) leaky-wave antenna for millimeter-wave applications," *IEEE Antennas Wireless Propag. Lett.*, vol. 7, pp. 85-88, April 2008.

[19] Y. J. Cheng, W. Hong, and K. Wu, "Millimeter-wave half mode substrate integrated waveguide frequency scanning antenna with quadri-polarization," *IEEE Trans. Antennas Propag.*, vol. 58, no. 6, pp. 1848-1855, Jun. 2010.

[20] Y. Dong and T. Itoh, "Composite right/left-handed substrate integrated waveguide and half mode substrate integrated waveguide leaky-wave structures," *IEEE Trans. Antennas Propag.*, vol. 59, no. 3, pp. 767-775, Mar. 2011.

[21] Y. Dong and T. Itoh, "Substrate integrated composite right-/left-handed leaky-wave structure for polarization-flexible antenna application," *IEEE Trans. Antennas Propag.*, vol. 60, no. 2, pp. 760-771, Feb. 2012.

[22] N. Nasimuddin, Z. N. Chen, and X. Qing, "Multilayered composite right/left-handed leaky-wave antenna with consistent gain," *IEEE Trans. Antennas Propag.*, vol. 60, no. 11, pp. 5056-5062, Nov. 2012.

[23] N. Nasimuddin, Z. N. Chen, and X. Qing, "Substrate integrated metamaterial-based leaky-wave antenna with improved boresight radiation bandwidth," *IEEE Trans. Antennas Propag.*, vol. 61, no. 7, pp. 3451-3457, Jul. 2013.

[24] C. W. Westerman, V. L. Harrington, and P. K. Park, "Analytic design of conformal slot arrays," *IEEE Trans. Antennas Propag.*, vol. 31, no. 4, pp. 668-672, Jul. 1983.

[25] Y.-Y. Liu, M. Guo, and S.-S. Zhong, "Conformal slotted waveguide array antenna," in *Proc. IEEE Int. Workshop Antenna Technol. (iWAT)*, Tucson, AZ, USA, Mar. 5-7, 2012, pp. 56-59.

[26] G.-X. Fan and J.-M. Jin, "Scattering from a cylindrically conformal slotted waveguide array antenna," *IEEE Trans. Antennas Propag.*, vol. 45, no. 7, pp. 1150 –1159, Jul. 1997.

[27] A. Traille, J. Ratner, G. D. Hopkins, and V. Tripp, "Development of a novel faceted, conformal, slotted-waveguide subarray for sensor applications with full 360° azimuth tracking capabilities," in *Proc. IEEE Antennas Propag. Soc. Int. Symp.*, Honolulu, HI, USA, Jun. 9-15, 2007, pp. 3828-3831.

[28] S. Cheng, H. Yousef, and H. Kratz, "79 GHz slot antennas based on substrate integrated waveguides (SIW) in a flexible printed circuit board," *IEEE Trans. Antennas Propag.*, vol. 57, no. 1, pp. 64-71, Jan. 2009.

[29] Y. J. Cheng, H. Xu, D. Ma, J. Wu, L. Wang, and Y. Fan, "Millimeter-wave shaped-beam substrate integrated conformal array antenna," *IEEE Trans. Antennas Propag.*, vol. 61, no. 9, pp. 4558-4566, Sep. 2013.

[30] Y. Cassivi, L. Perregrini, P. Arcioni, M. Bressan, K. Wu, and G. Conciauro, "Dispersion characteristics of substrate integrated rectangular waveguide," *IEEE Microw. Wireless Compon. Lett.*, vol. 12, no. 9, pp. 333-335, Sept. 2002.

[31] R. E. Collin, *Foundations for Microwave Engineering*, 2nd ed. New York: McGraw-Hill, 1992, pp. 181-184.

[32] L. Lewin, D. C. Chang, and E. F. Kuester, *Electromagnetic Waves and Curved Structures*. Stevenage, U.K.: IEEE Press, 1977.

[33] R. S. Elliott, *Antenna Theory and Design*, Revised ed. Hoboken, N.J: John Wiley & Sons, 2003.

[34] R. S. Elliott, "An improved design procedure for small arrays of shunt slots," *IEEE Trans. Antennas Propag.*, vol. 31, no. 1, pp. 48- 53, Jan. 1983.

[35] O. Bayraktar and O. A. Civi, "Slots on cylindrical substrate integrated waveguide," in *IEEE Antennas Propag. Society Int. Symposium (AP-S URSI)*, Chicago, IL, USA, Jul. 8-14, 2012, pp. 1-2.

[36] R. S. Elliott and W. O'Loughlin, "The design of slot arrays including internal mutual coupling," *IEEE Trans. Antennas Propag.*, vol. 34, no. 9, pp. 1149-1154, Sep. 1986.

[37] G.-X. Fan and Q. H. Liu, “Dyadic Green’s functions for curved waveguides and cavities and their reformulation,” *Radio Science*, vol. 37, no. 5, p. 1078, Oct. 2002.

[38] R. F. Harrington, *Time Harmonic Electromagnetic Fields*. New York: IEEE Press, 2001.

[39] S. F. Mahmoud, *Electromagnetic Waveguides: Theory and applications*. London: The Institution of Engineering and Technology, 1991.

[40] R. S. Elliott, “On the design of traveling-wave-fed longitudinal shunt slot arrays,” *IEEE Trans. Antennas Propag.*, vol. 27, no. 5, pp. 717-720, Sep. 1979.

[41] P. A. Rizzi, *Microwave Engineering: Passive Circuits*. Prentice Hall International, 1988.

[42] C. Tokgoz, “Derivation of closed form Green’s functions for cylindrically stratified media”, M.S. thesis, Dept. of Elect. Electronics Eng., Middle East Technical University, Ankara, Turkey, Aug. 1997.

[43] C. Tokgoz and G. Dural, “Closed-form Green's functions for cylindrically stratified media,” *IEEE Trans. Microw. Theory Tech.*, vol. 48, no. 1, pp. 40-49, Jan. 2000.

[44] S. Karan, “Closed-form Green's functions in cylindrically stratified media for method of moments applications,” M.S. thesis, Dept. of Elect. Electronics Eng., Bilkent University, Ankara, Turkey, Aug. 2006.

[45] S. W. Lee, R. Mittra, J. Boersma, and E. Yung, “An investigation on characterizing mutual coupling between two antenna slots on a cone,” Defense Technical Information Center, University of Illinois, Electromagnetics Laboratory Technical Report No. 79-2, Jan. 1979.

[46] Z. W. Chang, L. B. Felsen, and A. Hessel, “Surface ray methods for mutual coupling in conformal arrays on cylindrical and conical surfaces,” Final Report, Contract N00123-76-C-0236, POLY-EE EP-76-016, Jul. 1976.

[47] S. W. Lee and S. Safavi-Naini, “Asyptotic solution of surface field due to a magnetic dipole on a cylinder,” University of Illinois, Electromagnetics

Laboratory Technical Report No. 76-11, Nov. 1976 (a shortened version appeared in IEEE Trans. Antennas Propag., vol AP-26, pp. 593-589, 1978).

[48] J. Volakis, *Antenna Engineering Handbook*, 4th ed. New York: McGraw-Hill, 2007, p. 11-5.

[49] C. A. Balanis, *Antenna Theory, Analysis and Design*, 3rd ed. Hoboken, N.J: John Wiley, 2005.

[50] R. MacPhie, "The element density of a spherical antenna array," *IEEE Trans. Antennas Propag.*, vol. 16, no. 1, pp. 125-127, Jan. 1968.

[51] I. Chiba, K. Hariu, S. Sato, and S. Mano, "A projection method providing low sidelobe pattern in conformal array antennas," in *Antennas Propag. Society Int. Symposium Dig.*, Jun. 1989, vol. 1, pp. 130-133.

[52] O. Bayraktar and O. A. Civi, "Slot array on curved substrate integrated waveguide," in *IEEE Antennas Propag. Society Int. Symposium (AP-S URSI)*, Orlando, FL, USA, Jul. 7-13, 2013, pp. 246-247.

[53] V. B. Ertürk and B. Güner, "Analysis of finite arrays of circumferentially oriented printed dipoles on electrically large cylinders," *Microwave Opt. Technol. Lett.*, vol. 42, no. 4, pp. 299-304, Aug. 2004.

[54] G. A. Casula, G. Mazzarella, and G. Montisci, "Design of shaped beam planar arrays of waveguide longitudinal slots," *Int. Journal of Antennas Propag.*, 2013, Article ID: 767342, vol. 2013.

[55] J. J. Gulick and R. S. Elliott, "A general design procedure for small slot arrays," in *Antennas Propag. Society Int. Symposium*, Jun. 1987, vol. 25, pp. 302-305.

[56] M. Abramowitz and I. A. Stegun, *Handbook of Mathematical Functions with Formulas, Graphs, and Mathematical Tables*. New York: Dover Publications, 1965.

APPENDIX A

SYSTEMATIC CONSTRUCTION OF FIELDS IN BEND REGULAR WAVEGUIDES

In a homogeneous source-free region, the equations satisfied by the electric and magnetic fields are given by [38]

$$-\overline{\nabla} \times \overline{E} = \hat{z}\overline{H} \tag{A.1}$$

$$\overline{\nabla} \times \overline{H} = \hat{y}\overline{E} \tag{A.2}$$

$$\overline{\nabla}.\overline{E} = 0 \tag{A.3}$$

$$\overline{\nabla}.\overline{H} = 0 \tag{A.4}$$

The field components due to magnetic vector potential can be found using

$$\overline{\nabla}.\overline{H}^{A} = 0 \Rightarrow \overline{H}^{A} = \overline{\nabla} \times \overline{A} \tag{A.5}$$

$$\overline{E}^{A} = \hat{y}^{-1}\left(\overline{\nabla}\left(\overline{\nabla}.\overline{A}\right) + k^{2}\overline{A}\right) \tag{A.6}$$

The field components due to electric vector potential can be found using

$$\overline{\nabla}.\overline{E}^{F} = 0 \Rightarrow \overline{E}^{F} = -\overline{\nabla} \times \overline{F} \tag{A.7}$$

$$\overline{H}^{F} = \hat{z}^{-1}\left(\overline{\nabla}\left(\overline{\nabla}.\overline{F}\right) + k^{2}\overline{F}\right) \tag{A.8}$$

where $\hat{y} = j\omega\varepsilon$ and $\hat{z} = j\omega\mu$. ε and μ are the permittivity and permeability of the medium, respectively, and ω is the angular frequency.

The field components inside the E-plane bend regular waveguide shown in Figure 3.1 can be found using (A.5)-(A.8). The magnetic vector potential and transverse magnetic to z (TM^{z}_{mn}) modes in the E-plane bend regular waveguide shown in Figure 3.1 are given by [37]

$$\overline{A} = \sum_{m=0}^{\infty}\sum_{n=1}^{\infty} A_{mn}\cos\left(\frac{m\pi z}{a}\right) C_{\in_{mn}}\left(k_{\rho}^{TM^{z}_{mn}}\rho\right) e^{\pm j\in_{mn}\phi}\hat{a}_{z} \tag{A.9}$$

$$E_{\rho}^{A} = -\frac{1}{\hat{y}}\sum_{m=0}^{\infty}\sum_{n=1}^{\infty} A_{mn}\frac{m\pi}{a}\sin\left(\frac{m\pi z}{a}\right) C'_{\in_{mn}}\left(k_{\rho}^{TM^{z}_{mn}}\rho\right) k_{\rho}^{TM^{z}_{mn}} e^{\pm j\in_{mn}\phi} \tag{A.10}$$

$$E_{\phi}^{A} = \mp\frac{j}{\hat{y}\rho}\sum_{m=0}^{\infty}\sum_{n=1}^{\infty} A_{mn}\frac{m\pi}{a}\sin\left(\frac{m\pi z}{a}\right) C_{\in_{mn}}\left(k_{\rho}^{TM^{z}_{mn}}\rho\right)\in_{mn} e^{\pm j\in_{mn}\phi} \tag{A.11}$$

$$E_{z}^{A} = \sum_{m=0}^{\infty}\sum_{n=1}^{\infty} A_{mn}\frac{\left(k_{\rho}^{TM^{z}_{mn}}\right)^{2}}{\hat{y}}\cos\left(\frac{m\pi z}{a}\right) C_{\in_{mn}}\left(k_{\rho}^{TM^{z}_{mn}}\rho\right) e^{\pm j\in_{mn}\phi} \tag{A.12}$$

$$H_{\rho}^{A} = \pm\frac{j}{\rho}\sum_{m=0}^{\infty}\sum_{n=1}^{\infty} A_{mn}\cos\left(\frac{m\pi z}{a}\right) C_{\in_{mn}}\left(k_{\rho}^{TM^{z}_{mn}}\rho\right)\in_{mn} e^{\pm j\in_{mn}\phi} \tag{A.13}$$

$$H_{\phi}^{A} = -\sum_{m=0}^{\infty}\sum_{n=1}^{\infty} A_{mn}\cos\left(\frac{m\pi z}{a}\right) C'_{\in_{mn}}\left(k_{\rho}^{TM^{z}_{mn}}\rho\right) k_{\rho}^{TM^{z}_{mn}} e^{\pm j\in_{mn}\phi} \tag{A.14}$$

$$H_{z}^{A} = 0 \tag{A.15}$$

$$\overline{E}^{A} = E_{\rho}^{A}\hat{a}_{\rho} + E_{\phi}^{A}\hat{a}_{\phi} + E_{z}^{A}\hat{a}_{z} \tag{A.16}$$

$$\overline{H}^{A} = H_{\rho}^{A}\hat{a}_{\rho} + H_{\phi}^{A}\hat{a}_{\phi} + H_{z}^{A}\hat{a}_{z} \tag{A.17}$$

$$k_\rho^{TM_{mn}^z} = \sqrt{k^2 - \left(\frac{m\pi}{a}\right)^2}\ ,\ \ \mathrm{Im}\left(k_\rho^{TM_{mn}^z}\right) \le 0 \tag{A.18}$$

$$C_{\in_{mn}}\left(k_\rho^{TM_{mn}^z}\rho\right) = J_{\in_{mn}}\left(k_\rho^{TM_{mn}^z}\rho_1\right)Y_{\in_{mn}}\left(k_\rho^{TM_{mn}^z}\rho\right) - Y_{\in_{mn}}\left(k_\rho^{TM_{mn}^z}\rho_1\right)J_{\in_{mn}}\left(k_\rho^{TM_{mn}^z}\rho\right) \tag{A.19}$$

$$C_{\in_{mn}}\left(k_\rho^{TM_{mn}^z}\rho_2\right) = J_{\in_{mn}}\left(k_\rho^{TM_{mn}^z}\rho_1\right)Y_{\in_{mn}}\left(k_\rho^{TM_{mn}^z}\rho_2\right) - Y_{\in_{mn}}\left(k_\rho^{TM_{mn}^z}\rho_1\right)J_{\in_{mn}}\left(k_\rho^{TM_{mn}^z}\rho_2\right) \tag{A.20}$$

where $J_{\in_{mn}}\left(k_\rho^{TM_{mn}^z}\rho\right)$ and $Y_{\in_{mn}}\left(k_\rho^{TM_{mn}^z}\rho\right)$ are Bessel functions of first and second kinds, respectively, with order $\in_{mn}$ and argument $k_\rho^{TE_{mn}^z}\rho$. $\in_{mn}$ are the roots of (A.20). The prime sign indicates the derivative with respect to the argument.

The electric vector potential and transverse electric to z (TE_{mn}^z) modes in the E-plane bend regular waveguide shown in Figure 3.1 are given by [37]

$$\overline{F} = \sum_{m=1}^{\infty}\sum_{n=0}^{\infty} F_{mn}\sin\left(\frac{m\pi z}{a}\right)B_{\mu_{mn}}\left(k_\rho^{TE_{mn}^z}\rho\right)e^{\pm j\mu_{mn}\phi}\hat{a}_z \tag{A.21}$$

$$E_\rho^F = \mp\frac{j}{\rho}\sum_{m=1}^{\infty}\sum_{n=0}^{\infty} F_{mn}\sin\left(\frac{m\pi z}{a}\right)B_{\mu_{mn}}\left(k_\rho^{TE_{mn}^z}\rho\right)\mu_{mn}e^{\pm j\mu_{mn}\phi} \tag{A.22}$$

$$E_\phi^F = \sum_{m=1}^{\infty}\sum_{n=0}^{\infty} F_{mn}\sin\left(\frac{m\pi z}{a}\right)B'_{\mu_{mn}}\left(k_\rho^{TE_{mn}^z}\rho\right)k_\rho^{TE_{mn}^z}e^{\pm j\mu_{mn}\phi} \tag{A.23}$$

$$E_z^F = 0 \tag{A.24}$$

$$H_\rho^F = \frac{1}{\hat{z}}\sum_{m=1}^{\infty}\sum_{n=0}^{\infty} F_{mn}\frac{m\pi}{a}\cos\left(\frac{m\pi z}{a}\right)B'_{\mu_{mn}}\left(k_\rho^{TE_{mn}^z}\rho\right)k_\rho^{TE_{mn}^z}e^{\pm j\mu_{mn}\phi} \tag{A.25}$$

$$H_\phi^F = \pm\frac{j}{\hat{z}\rho}\sum_{m=1}^{\infty}\sum_{n=0}^{\infty} F_{mn}\frac{m\pi}{a}\cos\left(\frac{m\pi z}{a}\right)B_{\mu_{mn}}\left(k_\rho^{TE_{mn}^z}\rho\right)\mu_{mn}e^{\pm j\mu_{mn}\phi} \tag{A.26}$$

$$H_z^F = \sum_{m=1}^{\infty}\sum_{n=0}^{\infty} F_{mn} \frac{\left(k_\rho^{TE_{mn}^z}\right)^2}{\hat{z}} \sin\left(\frac{m\pi z}{a}\right) B_{\mu_{mn}}\left(k_\rho^{TE_{mn}^z}\rho\right) e^{\pm j\mu_{mn}\phi} \tag{A.27}$$

$$\overline{E}^F = E_\rho^F \hat{a}_\rho + E_\phi^F \hat{a}_\phi + E_z^F \hat{a}_z \tag{A.28}$$

$$\overline{H}^F = H_\rho^F \hat{a}_\rho + H_\phi^F \hat{a}_\phi + H_z^F \hat{a}_z \tag{A.29}$$

$$k_\rho^{TE_{mn}^z} = \sqrt{k^2 - \left(\frac{m\pi}{a}\right)^2}\ ,\ \ \mathrm{Im}\left(k_\rho^{TE_{mn}^z}\right) \le 0 \tag{A.30}$$

$$B_{\mu_{mn}}\left(k_\rho^{TE_{mn}^z}\rho\right) = J'_{\mu_{mn}}\left(k_\rho^{TE_{mn}^z}\rho_1\right) Y_{\mu_{mn}}\left(k_\rho^{TE_{mn}^z}\rho\right) - Y'_{\mu_{mn}}\left(k_\rho^{TE_{mn}^z}\rho_1\right) J_{\mu_{mn}}\left(k_\rho^{TE_{mn}^z}\rho\right) \tag{A.31}$$

$$B'_{\mu_{mn}}\left(k_\rho^{TE_{mn}^z}\rho\right) = \frac{\partial B_{\mu_{mn}}\left(k_\rho^{TE_{mn}^z}\rho\right)}{\partial\left(k_\rho^{TE_{mn}^z}\rho\right)} \tag{A.32}$$

$$B'_{\mu_{mn}}\left(k_\rho^{TE_{mn}^z}\rho\right)\Big|_{\rho=\rho_2} = \left.\frac{\partial B_{\mu_{mn}}\left(k_\rho^{TE_{mn}^z}\rho\right)}{\partial\left(k_\rho^{TE_{mn}^z}\rho\right)}\right|_{\rho=\rho_2} \tag{A.33}$$

where $J_{\mu_{mn}}\left(k_\rho^{TE_{mn}^z}\rho\right)$ and $Y_{\mu_{mn}}\left(k_\rho^{TE_{mn}^z}\rho\right)$ are Bessel functions of first and second kinds, respectively, with order μ_{mn} and argument $k_\rho^{TE_{mn}^z}\rho$. μ_{mn} are the roots of (A.33).

APPENDIX B

FIELDS RADIATED BY APERTURES ON PEC CYLINDER

The cylindrical transform of the tangential electric fields on the PEC cylindrical surface with aperture shown in Figure B1 is given by, [38]

$$\widetilde{E}_z(n,k_z)=\frac{1}{2\pi}\int_0^{2\pi}d\phi\int_{-\infty}^{\infty}dzE_z(\rho_2,\phi,z)e^{-jn\phi}e^{-jk_zz} \tag{B.1}$$

$$\widetilde{E}_\phi(n,k_z)=\frac{1}{2\pi}\int_0^{2\pi}d\phi\int_{-\infty}^{\infty}dzE_\phi(\rho_2,\phi,z)e^{-jn\phi}e^{-jk_zz} \tag{B.2}$$

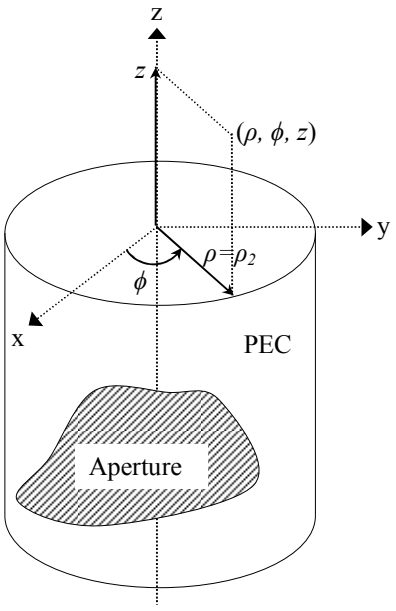

Figure B1: PEC cylindrical surface with aperture.

The inverse transformation is

$$E_z(\rho_2,\phi,z)=\frac{1}{2\pi}\sum_{n=-\infty}^{\infty}e^{jn\phi}\int_{-\infty}^{\infty}\widetilde{E}_z(n,k_z)e^{jk_z z}dk_z \tag{B.3}$$

$$E_\phi(\rho_2,\phi,z)=\frac{1}{2\pi}\sum_{n=-\infty}^{\infty}e^{jn\phi}\int_{-\infty}^{\infty}\widetilde{E}_\phi(n,k_z)e^{jk_z z}dk_z \tag{B.4}$$

Using the wave functions

$$A_z=\frac{1}{2\pi}\sum_{n=-\infty}^{\infty}e^{jn\phi}\int_{-\infty}^{\infty}f_n(k_z)H_n^{(2)}\left(\rho\sqrt{k_0^2-k_z^2}\right)e^{jk_z z}dk_z \tag{B.5}$$

$$F_z=\frac{1}{2\pi}\sum_{n=-\infty}^{\infty}e^{jn\phi}\int_{-\infty}^{\infty}g_n(k_z)H_n^{(2)}\left(\rho\sqrt{k_0^2-k_z^2}\right)e^{jk_z z}dk_z \tag{B.6}$$

and using (A.1)-(A.8), the fields radiated by the aperture field can be found as

$$E_z(\rho,\phi,z)=\frac{1}{j\omega\varepsilon_0}\frac{1}{2\pi}\sum_{n=-\infty}^{\infty}e^{jn\phi}\int_{-\infty}^{\infty}\left(k_0^2-k_z^2\right)f_n(k_z)H_n^{(2)}\left(\rho\sqrt{k_0^2-k_z^2}\right)e^{jk_z z}dk_z \tag{B.7}$$

$$E_\phi(\rho,\phi,z)=\frac{1}{2\pi}\sum_{n=-\infty}^{\infty}e^{jn\phi}\int_{-\infty}^{\infty}\left[\begin{array}{l}-\dfrac{nk_z}{j\omega\varepsilon_0\rho}f_n(k_z)H_n^{(2)}\left(\rho\sqrt{k_0^2-k_z^2}\right)+\\ g_n(k_z)\sqrt{k_0^2-k_z^2}\,H_n'^{(2)}\left(\rho\sqrt{k_0^2-k_z^2}\right)\end{array}\right]e^{jk_z z}dk_z \tag{B.8}$$

$$H_Z(\rho,\phi,z)=\frac{1}{j\omega\mu_0}\frac{1}{2\pi}\sum_{n=-\infty}^{\infty}e^{jn\phi}\int_{-\infty}^{\infty}\left(k_0^2-k_z^2\right)g_n(k_z)H_n^{(2)}\left(\rho\sqrt{k_0^2-k_z^2}\right)e^{jk_z z}dk_z \tag{B.9}$$

$$H_\phi(\rho,\phi,z)=\frac{1}{2\pi}\sum_{n=-\infty}^{\infty}e^{jn\phi}\int_{-\infty}^{\infty}\left[\begin{array}{l}-nk_z\dfrac{1}{j\omega\mu_0}\dfrac{1}{\rho}g_n(k_z)H_n^{(2)}\left(\rho\sqrt{k_0^2-k_z^2}\right)-\\ \sqrt{k_0^2-k_z^2}\,f_n(k_z)H_n'^{(2)}\left(\rho\sqrt{k_0^2-k_z^2}\right)\end{array}\right]e^{jk_z z}dk_z \tag{B.10}$$

where $H_n^{(2)}$ is the Hankel function of second kind and $H_n'^{(2)}(z)$ is the derivative of the Hankel function of second kind with respect to its argument.

By equating (B.3) to (B.7) and (B.4) to (B.8) at $\rho = \rho_2$

$$f_n(k_z) = \frac{j\omega\varepsilon_0 \widetilde{E}_z(n,k_z)}{(k_0^2 - k_z^2) H_n^{(2)}\left(\rho_2\sqrt{k_0^2 - k_z^2}\right)} \tag{B.11}$$

$$g_n(k_z) = \frac{1}{\sqrt{k_0^2 - k_z^2}\, H_n'^{(2)}\left(\rho_2\sqrt{k_0^2 - k_z^2}\right)}\left[\widetilde{E}_\phi(n,k_z) + \frac{nk_z}{\rho_2(k_0^2 - k_z^2)}\widetilde{E}_z(n,k_z)\right] \tag{B.12}$$

APPENDIX C

ASYMPTOTIC FORMS OF HANKEL FUNCTION RATIOS FOR LARGE ORDER AND ARGUMENT

The asymptotic forms for the ratios of the Hankel function of second kind and its derivative, $H_n'^{(2)}(z)/H_n^{(2)}(z)$ is derived using the formulations given in [56]. The Hankel function of the second kind can be written in terms of Bessel functions of first and second kinds as [56]

$$H_n^{(2)}(z) = J_n(z) - jY_n(z) \tag{C. 1}$$

The recurrence formulas are given by [56] as

$$H_n'^{(2)}(z) = H_{n-1}^{(2)}(z) - \frac{n}{z} H_n^{(2)}(z) \tag{C. 2}$$

$$H_n'^{(2)}(z) = -H_{n+1}^{(2)}(z) + \frac{n}{z} H_n^{(2)}(z) \tag{C. 3}$$

The asymptotic forms of the Bessel functions of first and second kinds are given as, [56]

$$J_n(z) \approx \frac{1}{\sqrt{2\pi n}} \left(\frac{ez}{2n} \right)^n, \; n \to \infty \tag{C. 4}$$

$$Y_n(z) \approx -\sqrt{\frac{2}{\pi n}}\left(\frac{ez}{2n}\right)^{-n},\ n \to \infty \tag{C. 5}$$

Using (C. 1), (C. 2), (C. 4), and (C. 5), the asymptotic form of $H_n'^{(2)}(z)/H_n^{(2)}(z)$ can be found as

$$\lim_{n\to\infty} \frac{H_n'^{(2)}(z)}{H_n^{(2)}(z)} = -\frac{n}{z} \tag{C. 6}$$

The asymptotic form for large negative orders can be found by the help of the formula given by [56] as

$$H_{-n}^{(2)}(z) = (-1)^n H_n^{(2)}(z) \tag{C. 7}$$

Using (C. 1), (C. 3), (C. 4), (C. 5), and (C. 7), the asymptotic form of $H_n'^{(2)}(z)/H_n^{(2)}(z)$ can be found for large negative orders as

$$\lim_{n\to-\infty} \frac{H_n'^{(2)}(z)}{H_n^{(2)}(z)} = \frac{n}{z} \tag{C. 8}$$

The asymptotic form expressions of the Hankel function of second kind for large argument can be written for fixed integer order n and as, [56]

$$H_n^{(2)}(z) \approx \sqrt{\frac{2}{z\pi}} e^{-j\left(z-\frac{n\pi}{2}-\frac{\pi}{4}\right)},\quad -2\pi < \arg(z) < \pi,\quad |z| \to \infty \tag{C. 9}$$

Inserting (C. 9) into (C. 2) or (C. 3)

$$\lim_{|z|\to\infty} \frac{H_n'^{(2)}(z)}{H_n^{(2)}(z)} = -j \tag{C. 10}$$

CURRICULUM VITAE

PERSONEL INFORMATION

Surname, Name: Bayraktar, Ömer

Nationality: Turkish (TC)

Date and Place of Birth: 22 Feb. 1983, Aydın

Marital Status: Married

Phone: +90 312 210 60 72

Fax: +90 312 210 23 04

email: bomer@metu.edu.tr

EDUCATION

Degree	Institution	Year of Graduation
Ph.D.	METU Electrical and Electronics Eng.	2014
M.Sc.	METU Electrical and Electronics Eng.	2007
B.Sc.	METU Electrical and Electronics Eng.	2005
High School	A.O.S. Science High School, Bursa	2000

WORK EXPERIENCE

Year	Place	Enrollment
2013-Present	METU Electrical and Electronics Eng.	Project Personnel
2012-2013	METU-Mems Center	Scientific Project Expert
2007-2012	METU Electrical and Electronics Eng.	Research Assistant
2005-2007	METU Electrical and Electronics Eng.	Project Assistant
July 2004	ASELSAN	Summer Practice
July 2003	TOFAŞ A.Ş.	Summer Practice

FOREIGN LANGUAGES

Advanced English

AWARDS

Graduated with high honors from undergraduate studies.

METU Lecture performance award in Ph.D.

Successful Student Paper award in National URSI Symposium Turkey, 2010.

Ranked 3 in student paper competition in National URSI Symposium Turkey, 2014.

URSI GASS Young Scientist award, 2014.

INTERNATIONAL JOURNAL PUBLICATIONS

1. O. Bayraktar and O. A. Civi, "Circumferential traveling wave slot array on cylindrical substrate integrated waveguide (CSIW)," *IEEE Trans. Antennas Propag.,* vol. 62, no. 7, pp. 3557-3566, Jul. 2014.
2. O. Bayraktar, O. A. Civi, and T. Akin, "Beam switching reflectarray monolithically integrated with RF MEMS switches," *IEEE Trans. Antennas Propag.*, vol. 60, no. 2, pp. 854-862, Feb. 2012.

INTERNATIONAL CONFERENCE PUBLICATIONS

1. O. Bayraktar and O. A. Civi, "Cylindrical substrate integrated waveguide (CSIW) slot arrays with uniform and nonuniform spacings," in *Proc. 31st General Assembly and Scientific Symposium (URSI GASS)*, Beijing, China, Aug. 16-23, 2014.
2. O. Bayraktar and O. A. Civi, "Slot array on curved substrate integrated waveguide," in *IEEE Antennas Propag. Society Int. Symposium (AP-S URSI)*, Orlando, Florida, USA, Jul. 7-13, 2013, pp. 246-247.
3. O. Bayraktar and O. A. Civi, "Slots on cylindrical substrate integrated waveguide," in *IEEE Antennas Propag. Society Int. Symposium (AP-S URSI)*, Chicago, IL, USA, Jul. 8-14, 2012, pp. 1-2.

4. O. Bayraktar, O. A. Civi, and T. Akin, "Beam switching reflectarray with MEMS controls," in *Proc. 4th European Conference on Antennas and Propagation (EuCAP),* Barcelona, Spain, April 12-16, 2010.

5. K. Topalli, O. Bayraktar, M. Unlu, O. Aydin Civi, S. Demir, and T. Akin, "Reconfigurable antennas by RF MEMS technology," in *Proc. 30th ESA Antenna Workshop on Antennas for Earth Observation, Science, Telecommunications and Navigation Space Missions*, Noordwijk, Netherlands, May 27-30, 2008, pp. 497-500.

6. K. Topalli, M. Unlu, I. Istanbulluoglu, H. I. Atasoy, O. Bayraktar, O. Aydin Civi, Ş. Demir, S. Koc, and T. Akin, "Reconfigurable RF MEMS devices and antennas," in *Proc. 5th International Conference on Electrical and Electronics Engineering (ELECO)*, Bursa, Turkey, Dec. 5-9, 2007, pp. 204-209.

7. O. Bayraktar, K. Topalli, M. Unlu, O. A. Civi, S. Demir, and T. Akin, "Beam switching reflectarray using RF MEMS technology," in *Proc. 2nd European Conference on Antennas and Propagation (EuCAP 2007)*, Edinburgh, UK, 11-16 Nov. 11-16, 2007.

8. O. Bayraktar, K. Topalli, M. Unlu, I. Istanbulluoglu, E. U. Temocin, H. I. Atasoy, O. A. Civi, S. Demir, S. Koc, and T. Akin, "Reconfigurable reflectarray using RF MEMS technology," in *Proc. 1st European Conference on Antennas and Propagation (EuCAP)*, Nice, France, Nov. 6-10, 2006.

9. E. Erdil, K. Topalli, M. Unlu, I. Istanbulluoglu, E. U. Temocin, H. I. Atasoy, O. Bayraktar, O. A. Civi, S. Demir, S. Koc, and T. Akin, "Reconfigurable slot antenna with fixed-fixed beam type RF MEMS capacitors," in *Proc. 1st European Conference on Antennas and Propagation (EuCAP)*, Nice, France, Nov. 6-10, 2006.

10. H. I. Atasoy, M. Unlu, K. Topalli, I. Istanbulluoglu, O. Bayraktar, E. U. Temocin, S. Demir, O. A. Civi, S. Koc, and T. Akin, "Investigation of on-wafer TRL calibration accuracy dependence on transitions and probe positioning," in

Proc. 36th European Microwave Conference, Manchester, UK, Sep. 10-15, 2006, pp. 1582-1585.

11. M. Unlu, K. Topalli, H. I. Atasoy, E. U. Temocin, I. Istanbulluoglu, O. Bayraktar, S. Demir, O. A. Civi, S. Koc, and T. Akin, "A Reconfigurable RF MEMS triple stub impedance matching network," in *Proc. 36th European Microwave Conference*, Manchester, UK, Sep. 10-15, 2006, pp. 1370-1373.

12. H. I. Atasoy, K. Topalli, M. Unlu, I. Istanbulluoglu, E. U. Temocin, O. Bayraktar, S. Demir, O. A. Civi, S. Koc, and T. Akin, "Metal-to-metal and capacitive contact RF MEMS shunt switch structures," *7th Workshop on MEMS for MilimeterWave Communications (MEMSWAVE)*, Orvieto, Italy, Jun. 27-30, 2006, pp. 154-156.

13. M. Unlu, K. Topalli, H. I. Atasoy, E. U. Temocin, I. Istanbulluoglu, O. Bayraktar, S. Demir, O. A. Civi, S. Koc, and T. Akin, "A reconfigurable RF MEMS impedance tuner for impedance matching of a two-stage low noise amplifier," *7th Workshop on MEMS for MilimeterWave Communications (MEMSWAVE)*, Orvieto, Italy, Jun. 27-30, 2006, pp. 115-118.